A Study of Photoactive Materials for Solution-Processed Thin-Film Solar Cells

by

Andrew Namespetra

Submitted in partial fulfilment of the requirements
for the degree of Master of Science

at

Dalhousie University
Halifax, Nova Scotia
August 2015

DEDICATIONS

I dedicate this thesis to my family, for their love and support, and to all of my friends who have accompanied me on the journey through grad school.

TABLE OF CONTENTS

LIST OF TABLES

LIST OF FIGURES

ABSTRACT

The overall goal of the research projects herein is to fabricate low-cost and efficient thin-film perovskite and organic solar cells. The fabrication of a planar-heterojunction perovskite solar cell was first optimized by investigating factors that influence perovskite thin film formation. The optimized sequential spin-coating method produces uniform perovskite thin films and yields devices achieving power conversion efficiencies beyond 13 %. Secondly, cheap, organic hole-transporting materials based on a triphenylamine core were investigated as alternatives to spiro-OMeTAD in perovskite solar cells, but poor solubility led to deficiencies in photovoltaic performance. Finally, it was shown that both solution processing techniques and molecular design can influence the morphology, electronic properties and crystallinity of thin films consisting of a fullerene-free donor-acceptor pair for applications in organic solar cells. It was determined that solution processing and the molecular composition of photoactive materials influences thin film properties and device performance in perovskite and organic solar cells.

LIST OF ABBREVIATIONS USED

AFM	Atomic force microscopy
BDT	Benzodithiophene
BHJ	Bulk-Heterojunction
CB	Chlorobenzene
CBM	Conduction band minimum
CV	Cyclic voltammetry/voltammogram
D-A	Donor-Acceptor
DFT	Density functional theory
DI	Deionized
DIO	1,8-diiodooctane
DMF	Dimethylformamide
DPP	Diketopyrrolopyrrole
EDOT	3,4-ethylenedioxythiophene
ETL	Electron-transporting layer
ETM	Electron-transporting material
Fc	Ferrocene
FTO	Fluorine-doped tin oxide
FWHM	Full-width half-height maximum
HOMO	Highest occupied molecular orbital
HTL	Hole-transporting layer
HTM	Hole-transporting material
ITO	Indium-doped tin oxide
I-V	Current-voltage
J-V	Current density-voltage
Li-TFSI	Lithium trifluoromethanesulfonate
LUMO	Lowest unoccupied molecular orbital
MAI	Methylammonium iodide
$MAPbI_3$	Methylammonium lead iodide
1-NA	1-naphthaldehyde
NHE	Normal hydrogen electrode
NMR	Nuclear magnetic spectroscopy
OFET	Organic field-effect transistor
OM	Optical microscope/microscopy
OPV	Organic photovoltaic
OSC	Organic solar cell
PDMS	Polydimethylsiloxane
P3HT	Poly-3-hexylthiophene
PEDOT:PSS	Ethylenedioxythiophene : poly(styrene sulphonate)
PHJ	Planar heterojunction
PCBM	Phenyl-C_{61}-butyric acid methyl ester
PCE	Power conversion efficiency
PDI	Perylene diimide
PL	Photoluminescence
PSC	Perovskite solar cell
PTFE	Polytetrafluoroethylene

PVDF	Polyvinylidene fluoride
R2R	Roll-to-roll
RMS	Root mean square
RT	Room temperature
SDC	Sequential dip-coating
SEM	Scanning electron microscopy
SPM	Scanning probe microscopy
SSC	Sequential spin-coating
SVA	Solvent vapour annealing
tBP	tert-butylpyridine
4-TFBA	4-trifluoromethyl benzoic acid
TGA	Thermogravimetric analysis
TFT	Thin-film transistor
THF	Tetrahydrofuran
TPA	Triphenylamine
UPS	Ultraviolet photoelectron spectroscopy
UV-Vis	Ultraviolet-Visible
VBM	Valence band maximum
XPS	X-ray photoelectron spectroscopy
XRD	X-ray diffraction

ACKNOWLEDGEMENTS

First and foremost, I would like to thank my supervisors Prof. Gregory Welch and Prof. Ian Hill for their continued guidance and mentorship throughout my program. I also thank Prof. Jean Burnell for his assistance on my thesis and Prof. Mary Anne White and Prof. Jeffery Dahn for their roles as committee members.

This work was made possible due to collaborations with other members of the Welch and Hill research groups. I would like to thank each contributing member individually:

i) Arthur Hendsbee for: i) synthesis of organic materials including D1 and A1-A5, HTM01 and HTM02, ii) acquisition of CV data for D1, A1, A3, A4 and A5, iii) XRD patterns of the thermally-annealed blend films of D1:A1;

ii) Elizabeth Kitching for: i) spin-coating of the D1:A1 1:1 blends, ii) thermal-annealing of the corresponding films, and iii) acquisition of UV-Vis spectra of the films;

iii) Jetsuda Areephong for: i) synthesis of HTM03 and DPP1 and ii) acquisition of the corresponding solution UV-Vis and CV data for each of these materials;

iv) Seth McAfee for running the CV experiments for HTM04;

v) Jess Topple for her guidance and advice on use of the AFM; and

vi) Charlotte Clegg for help and support with optimizations of perovskite thin-films.

I wish to thank Dalhousie faculty members: Prof. Mark Obrovac for the use of his X-ray diffractometer and Prof. Jeff Dahn for the use of his SEM.

I would also like to thank Dr. Nicholas Vukotic for helping me with the analysis of the XRD powder patterns in Figure 3.15 using Jade software.

CHAPTER 1 - INTRODUCTION

1.1 Background: Solar Photovoltaic Technology

As the global demand for energy is projected to rise over the next few decades,[1] clean, renewable sources of energy are becoming increasingly important. Energy-capture systems such as wind, solar and hydroelectric are important to offset the dependence on fossil fuels for energy conversion.

Solar energy is particularly promising given the vast resource provided by the Sun. For example, 4.3×10^{20} J of energy from the Sun strikes the Earth every hour, which greatly exceeds the amount of energy consumed in the United States in an entire year.[2,3] Other strategies exist to capture energy from the Sun (e.g., solar thermal, solar fuels, etc.), but solar photovoltaic (PV) technology is the conversion of solar energy directly into electricity.

There are three general types of photovoltaic technology: first-, second- and third-generation. First-generation PV utilizes crystalline silicon as the active material; it is the most widespread PV technology and currently dominates the market. Second-generation thin-film PV technologies, including CIGS (copper indium gallium selenide), GaAs, CdTe, can be made with lower quantities of materials, but typically consist of scarce and/or toxic elements. Third-generation photovoltaic technologies utilize soluble photoactive materials. Therefore, the active layers can be formed via common printing and coating techniques,[4] offering the potential for rapid roll-to-roll (R2R) printing on an industrial scale.[5] These techniques can be performed at low temperatures, which opens the door for lightweight and flexible substrates such as foils and plastics. In general, from first- to second- to third-generation photovoltaics, the overall production cost can be reduced, but power conversion efficiencies (*PCE*s) also decrease. It is therefore a challenge to increase the *PCE* of third-generation PV to realize low-cost and efficient solar cells.

Two promising third-generation PV technologies are perovskite solar cells (PSCs) and organic solar cells (OSCs). PSCs have rapidly gained attention in the scientific community since their discovery in 2009.[6] To date, the most efficient lab-scale perovskite solar cells deliver a *PCE* greater than 19 %.[7] Although these were small area (10 mm^2) devices, they have the potential to compete with multi-crystalline Si solar cells, which demonstrate *PCE*s of ca. 21 % in larger-area modules.[8]

Organic solar cells employ organic π-conjugated polymers or small molecules as light-harvesters. While less efficient than PSCs and other inorganic photovoltaic technologies, OSCs have also seen great improvements in efficiency over the past three decades. Since one of the first reports of a functional organic solar cell in 1986 by Tang,[9] the efficiency of devices has improved from under 1% to the record of 11% in 2015.[8]

Despite similarities in operating principles, perovskite and organic solar cells have significant differences. Therefore, a discussion of both systems in terms of materials and device operation is warranted.

1.2. Perovskite Solar Cells (PSCs)

1.2.1. Perovskite Materials

The term "perovskite" refers to the class of crystal structures named after the Russian mineralogist Perovski. In general, perovskites have an "ABX_3" chemical formula, where the A and B cations are 12- and 6-coordinate with respect to the X anion (X is a halogen or oxygen). For years, inorganic-organic perovskites have remained interesting materials in electronic applications for their abundance, conductivity and excitonic properties.[10,11] In these materials, the size of the "A" cation governs the dimensionality of the structure. Small monovalent cations such as methylammonium (MA) and formamidium form 3D structures,[12] whereas large aryl groups can form the 2D layered structure.[13–15] The 3D structure is more relevant in photovoltaics for its lower bandgap and lower exciton binding energy.[16]

In 2009, Kojima *et al*., demonstrated the successful fabrication of a solar cell using methyl ammonium lead iodide ($CH_3NH_3PbI_3$ or "$MAPbI_3$") as the light-harvesting sensitizer (the crystal structure is shown in **Figure 1.1**).[6] $MAPbI_3$ continues to be used as the standard active layer for PSCs, but improvements in device and material design (e.g., the replacement of electrolyte with solid-state organic hole-transporting layers (HTLs))[17] have led to vast increases in performance and stability.

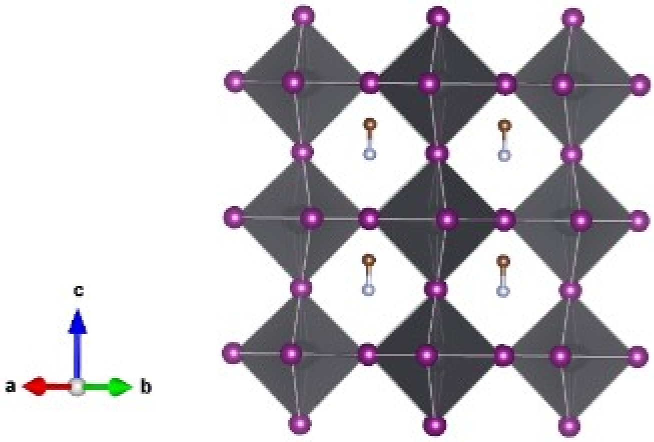

Figure 1.1. An image of the 110 projection of $MAPbI_3$ simulated using Vesta software from crystal structure information acquired by Stoumpos *et al.*[18] The PbI_6 octahedra are darkened for visual contrast. The Pb, I, C and N atoms are represented by black, purple, brown and silver icons, respectively.

1.2.2. Photovoltaic Mechanism in Perovskite Solar Cells

Photovoltaic performance in devices, whether in PSCs or OSCs, requires the absorption of photons, which is dependent on both the i) bandgap and ii) extinction coefficient of the active material. Materials for photovoltaic applications are generally designed and/or selected to match the bandgap with the region of the solar spectrum that displays the greatest flux, that is, the visible region which corresponds to wavelengths from 400 to 700 nm.

In general, a photovoltaic device operates by absorbing photons and generating charge carriers. Photoexcitation and charge generation occurs in the active layer which contains the photoactive material. The operation of a PSC is illustrated in **Figure 1.2 a)**. Since $MAPbI_3$ has a high dielectric constant ($\varepsilon \sim 18$),[19] photoexcitation in the perovskite generates free charge carriers; the electrons and holes separate immediately.[20] Electrons are the mobile charges and "holes" refer to the vacancies left by the electrons. The free electrons and holes move through conduction band minimum (CBM) and the valence band maximum (VBM), respectively, within the perovskite thin film active layer. The electrons diffuse to the interface of the electron-transporting (ETM), are transferred to the CBM of the ETM and are then collected at the cathode. In the PSCs used in the studies herein, TiO_2 is used as the ETM. Although TiO_2 has a very wide bandgap (~ 3 eV)[21] and may be viewed as an insulator, the CBM of TiO_2 aligns with the CBM of $CH_3NH_3PbI_3$ and is therefore accessible for electron transfer.[22] On the opposite side of the active layer, holes diffuse to the interface of the hole-transporting material (HTM) and are transferred to the highest occupied molecular orbital (HOMO) of the HTM. In **Figure 1.2 a)**, holes are depicted as moving charges, however, a more accurate picture is movement of electrons from the anode to fill the vacancies in the valence band maximum (VBM) of the perovskite left after photoexcitation. Using ultraviolet photoelectron spectroscopy (UPS), the VBM for $MAPbI_3$ has been measured to be −5.43 eV versus energy of an electron in vacuum.[17] It was also possible to determine the CBM (−3.93 eV) by applying the optical bandgap.

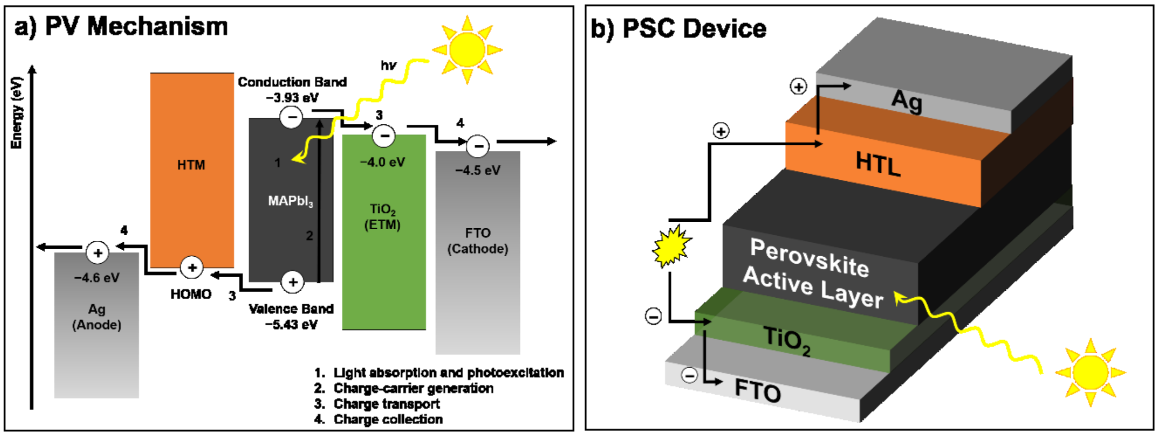

Figure 1.2. a) An energy level diagram illustrating the mechanism of charge generation in a PSC and b) a diagram depicting the device architecture of a PSC.

1.2.3. Device Construction

Thin-film perovskite solar cells s (and organic solar cells) are constructed in layered, “sandwich”-style devices, with each layer contributing to the generation of current. Complementary charge-transporting materials make contact with the active layer to extract the charges and generate a current. Charge transport is facilitated by movement of electrons from the higher-energy levels of the active material to the lower-energy levels of adjacent materials along a gradient. For this reason, selection of materials with appropriate energy levels is critical. **Figure 1.2 b)** depicts the typical device design or “architecture” for a PSC. Alternative architectures referred to as “inverted” devices exist for PSCs[23–26] however, these are not discussed herein. The devices are fabricated layer-by-layer on a glass substrate coated with a transparent conductive oxide, such as fluorine-doped tin oxide (FTO), that allows light to enter the device. The active layer is positioned in the middle of the device, with charge-transport layers making physical contact above and below.

In “normal” PSC devices, FTO serves as the cathode, where electrons are collected. The second layer is a dense thin film of TiO_2 which is both a hole-blocking and electron-transporting layer (ETL). The third layer is the perovskite active layer, which is the site of photoexcitation. Covering the perovskite is the hole-transporting layer (HTL) which consists of a wide bandgap organic semiconductor (e.g., 2,2',7,7'-tetrakis(*N*,*N*-di-*p*-methoxyphenylamine)-9,9'-spirobifluorene (spiro-OMeTAD), vide infra) that both harvests free holes from the perovskite and blocks the flow of electrons in the wrong direction (thus reducing the instances of recombination). Lastly, the top metal contact (usually Ag or Au) acts as the anode, which "collects holes" or supplies electrons to system.

1.3. Organic Solar Cells

1.3.1. Organic Semiconductor Materials

Organic semiconductors have conjugated structures with alternating double-single bonds and a continuous overlap of p-orbitals. This results in extensive π-electron delocalization and a narrowing of the bandgap energy, which is the difference in energy of the HOMO and the lowest-unoccupied molecular orbital (LUMO). These electronic properties allow for the absorption of photons.

Organic semiconductors exist in two categories: donors and acceptors. In general, acceptors have lower molecular orbital energy levels (relative to the ionization energy of hydrogen in vacuum) and correspondingly higher electron-affinity. Donors have elevated LUMO levels and therefore a lower electron affinity. The photoactive layer of an organic solar cell consists of an electron donor and an electron acceptor in physical contact. **Figure 1.3** depicts the structures of some common organic materials that function in organic solar cellss. Some of the best-performing acceptors are fullerene derivatives, such as phenyl-C_{61}-butyric acid or "PCBM," which will be discussed in greater detail in subsequent chapters. Also shown are examples of a polymer (poly 3-hexylthiophene or "P3HT") and small-molecule (5,5'-*bis*[(4-(7-hexylthiophen-2-yl)thiophen-2-yl)-[1,2,5]thiadiazolo[3,4-

c]pyridine]-3,3’-di-2-ethylhexylsilylene-2’2’-bithiophene or “DTS(PTTh$_2$)$_2$”)[27] donor material.

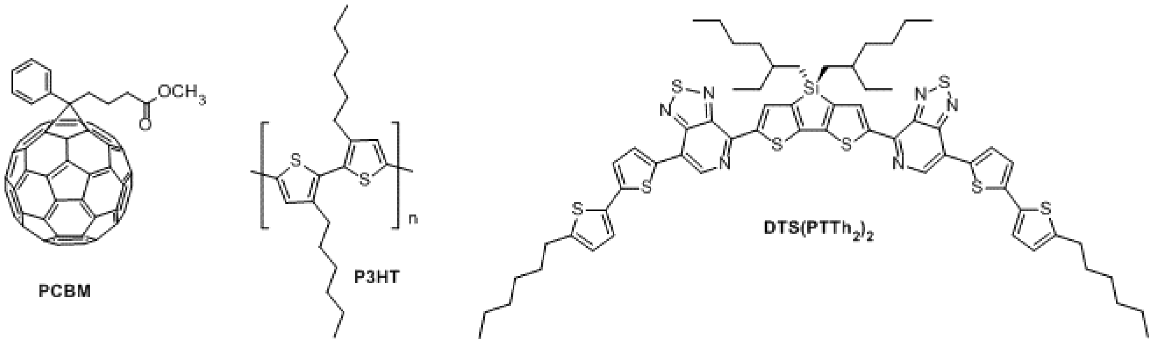

Figure 1.3. Examples of π-conjugated organic materials for OSCs.

1.3.2. Photovoltaic Mechanism in Organic Solar Cells

The photovoltaic mechanism in OSCs is illustrated in **Figure 1.4 a)**. In contrast to perovskite materials, organic semiconductors have lower dielectric constants ($\varepsilon \sim 3$).[28] Consequently, light-absorption of the donor in an organic solar cell generates a bound electron-hole pair known as an exciton. The exciton migrates to the D-A interface, where it can then dissociate into free charge carriers.[29] However, dissociation of the exciton is met by a Coulombic barrier known as the binding energy. As shown by Hill *et al.*,[30] the binding energy of organic semiconductors can be quite large (i.e., 0.4 to 1.4 eV) which necessitates a sufficient energy offset between the LUMO of the donor and the LUMO of the acceptor to induce charge separation. After separation, the free electrons and holes are transported through the acceptor and donor, respectively, and collected at the electrodes.

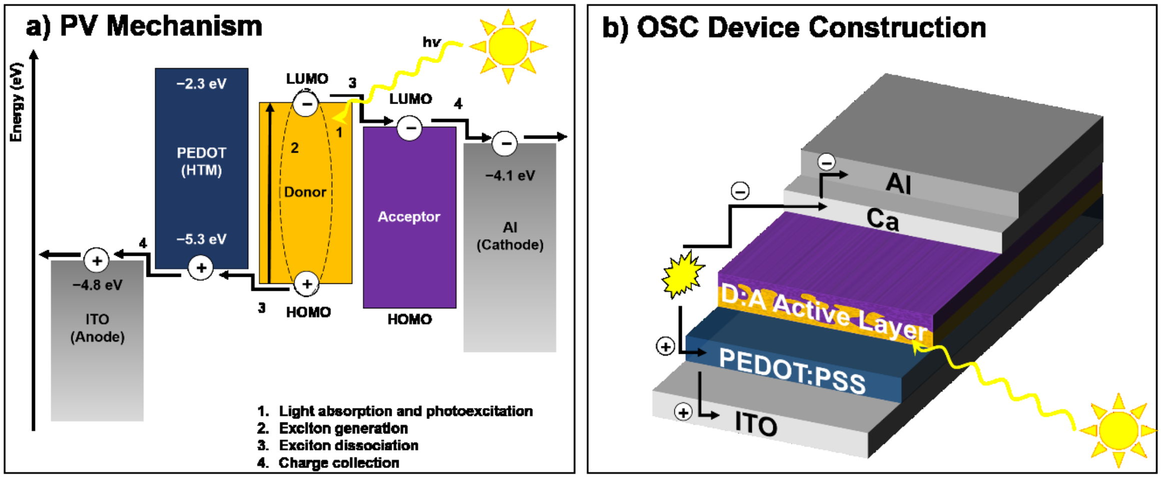

Figure 1.4. a) An energy level diagram illustrating the mechanism of charge generation in an OSC and b) a diagram depicting the device architecture of an OSC.

1.3.3. Organic Solar Cell Device Architecture

In conventional organic solar cell devices (**Figure 1.4 b)**), indium-doped tin oxide (ITO) serves as the anode (the site of hole-collection). The second layer is the hole-transporting layer, which is a mixture of conductive polymers poly(3,4-ethylenedioxythiophene) and polystyrene sulfonate in what is known as PEDOT:PSS. The third layer is the active layer composed of an interface of the donor and acceptor. The two materials come into contact at a D-A heterojunction, which is facilitated by the design of the active-layer. It is important to note that OSCs can also be built with an inverted architecture,[31] however these designs were not implemented in the projects herein and are therefore not discussed.

Two main types of active-layers in OSCs exist: a planar heterojunction (PHJ) and a bulk heterojunction (BHJ) (depicted in **Figure 1.5**). Since the exciton diffusion length in organic semiconductors is very short (10-20 nm), PHJ cells must have very thin donor and acceptor films to allow the excitons to reach the D-A interface before they decay. In contrast, the BHJ consists of an intimate mixture of the two materials, creating percolating networks within the "bulk" of the active layer.[32] A BHJ film is formed simply by dissolving the two materials in a common solvent, casting the solution, and allowing the donor and acceptor to self-assemble into distinct domains. Advantageously, BHJ active layers can be made thicker (~100 nm) than a PHJ, allowing for a greater quantity of light-absorbing material, and consequently higher current output. Lastly, the top contact is a low work-function metal, such as Al as the cathode. Metals are typically deposited by thermal evaporation under vacuum.

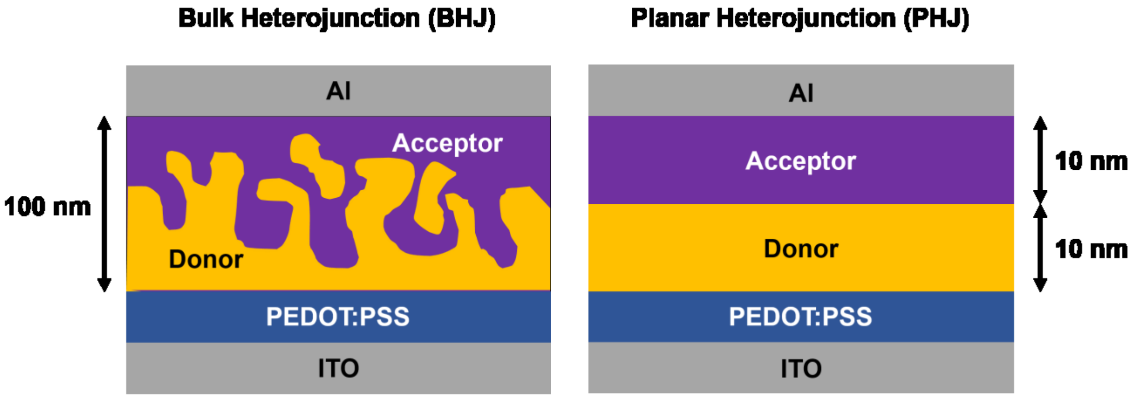

Figure 1.5. Cross-sectional illustrations of OSC devices, comparing planar and bulk heterojunction active layers in a conventional-style architecture.

1.4. Solar Cell Device Testing and Performance Metrics

Testing the photovoltaic performance is critical for the assessment of a solar cell and the quality of the functional materials (e.g., hole-transporting materials in a perovskite solar cell or a D-A pair in an organic solar cell). Measurement of the current (I) produced by the cell as a function of applied bias or voltage (V) generates an I-V curve (illustrated in **Figure 1.6**).

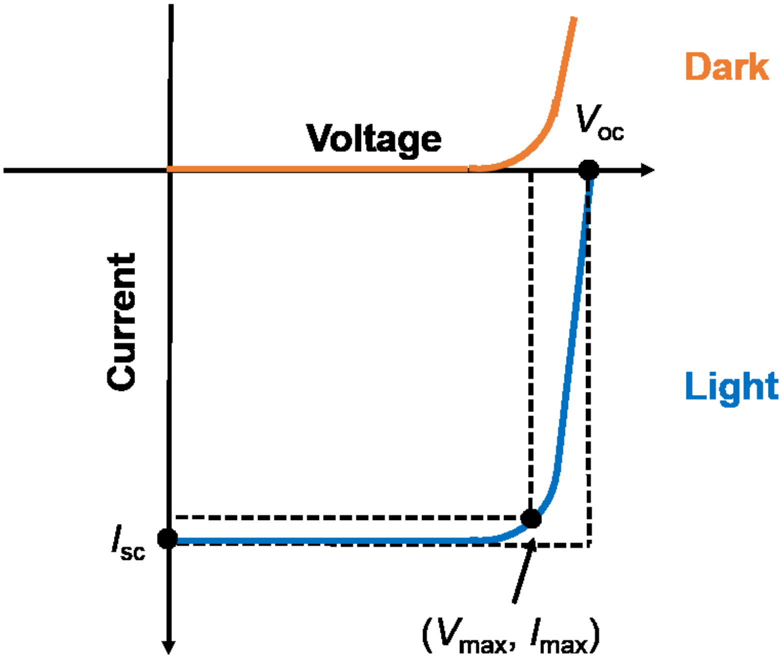

Figure 1.6. An illustration of *I-V* curves for a SC tested in the dark and in the light (i.e., under illumination).

In many cases, current is reported per unit area of the cell as a *current density* (*J*). By convention, the photogenerated current is *negative* on the *I-V* curve and the product of *I* and *V* is the power generated by the device (*P*):

$$P = IV. \tag{1}$$

From the *I-V* (or *J-V*) curve, many important parameters can be determined. First, the open-circuit voltage or V_{oc}, occurs when no current flows external to the cell. The maximum V_{oc} of a perovskite solar cell is the difference in potential energy between the CBM of the ETL (e.g., TiO_2) and the VBM of the HTL; in other words, the V_{oc} is the difference in potential energy of the excited electron and the collected hole.[33] Comparably, the V_{oc} of an organic solar cell is limited by potential difference between the LUMO of the acceptor and the HOMO of the donor. The second parameter is the short-circuit current (I_{sc} or J_{sc}) which occurs when the voltage equals zero and represents the maximum current output of the SC. Multiplying I by V gives P as a function of V which gives the maximum power (P_{max}) generated by the cell. The current and voltage at the maximum power point on the I-V curve are I_{max} and V_{max}, respectively. The power conversion efficiency (PCE or η) is the ratio of P_{max} to the power of the incident light (P_{in}) and is given by the equation:

$$PCE = \frac{P_{\mathrm{max}}}{P_{\mathrm{in}}} \; . \tag{2}$$

Another indicator of the overall quality of the cell is the fill-factor (FF), which is represented graphically by the ratio of the areas depicted on the I-V curve. The fill factor can be calculated by using Equation (3), which is given by:

$$FF = \frac{I_{\mathrm{max}} \cdot V_{\mathrm{max}}}{I_{sc} \cdot V_{\mathrm{oc}}} \; . \tag{3}$$

In the absence of light, a solar cell can be modelled as a diode, with current passing in one direction only (see circuit diagram in **Figure 1.7**). When illuminated, the cell produces a photo-generated current (I_{l}). The total output current (I) for an ideal cell is given by Equation (4) and is the difference of I_{l} and the diode current (I_{D}). Equation (4) is given by:

$$I = I_{\mathrm{D}} - I_{\mathrm{l}} = I_0\,(\mathrm{e}^{(qV/nkT)} - 1) - I_{\mathrm{l}}. \tag{4}$$

.

In Equation (4), q is the elementary charge of an electron (1.6×10^{-19} C), k is the Boltzmann constant (1.38×10^{-23} J/K) and T is the operating temperature in Kelvin.

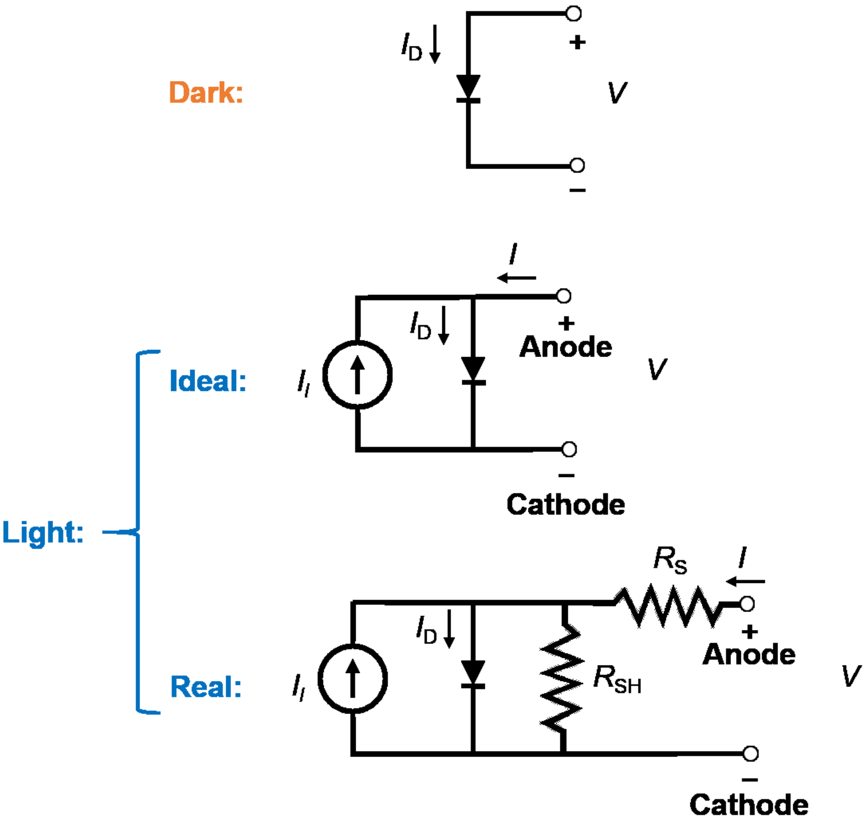

Figure 1.7. Circuit diagrams for an ideal solar cell operating under dark and light conditions and for a real cell, showing sources of parasitic resistances. By convention, the anode and cathode are defined as the sites of hole and electron collection, respectively. The "+" and "–" signs indicates the polarity of the applied bias during solar cell operation.

However, in a real solar cell, there are voltage losses due to parasitic series resistance (R_S) and parallel or shunt resistance (R_{SH}). R_S is related to the thickness of the active layer, conductivity of the materials, electrode interfaces and carrier mobilities. R_{SH} is reflective of the amount of structural and morphological defects in the active layer; defects decrease R_{SH}, thereby decreasing photovoltaic performance.[34] Taking these factors into account expands the diode current equation to:

$$I = I_D - I_l = I_0 \left(e^{(q(V+I \cdot R_S)/nkT)} - 1\right) - I_l + \frac{V + I \cdot R_S}{R_{SH}} \, . \tag{5}$$

The effect of R_S and R_{SH} on the *I-V* curve is represented in **Figure 1.8**. R_S and R_{SH} can be calculated as the inverse slope of the curve and open-circuit and short-circuit, respectively.

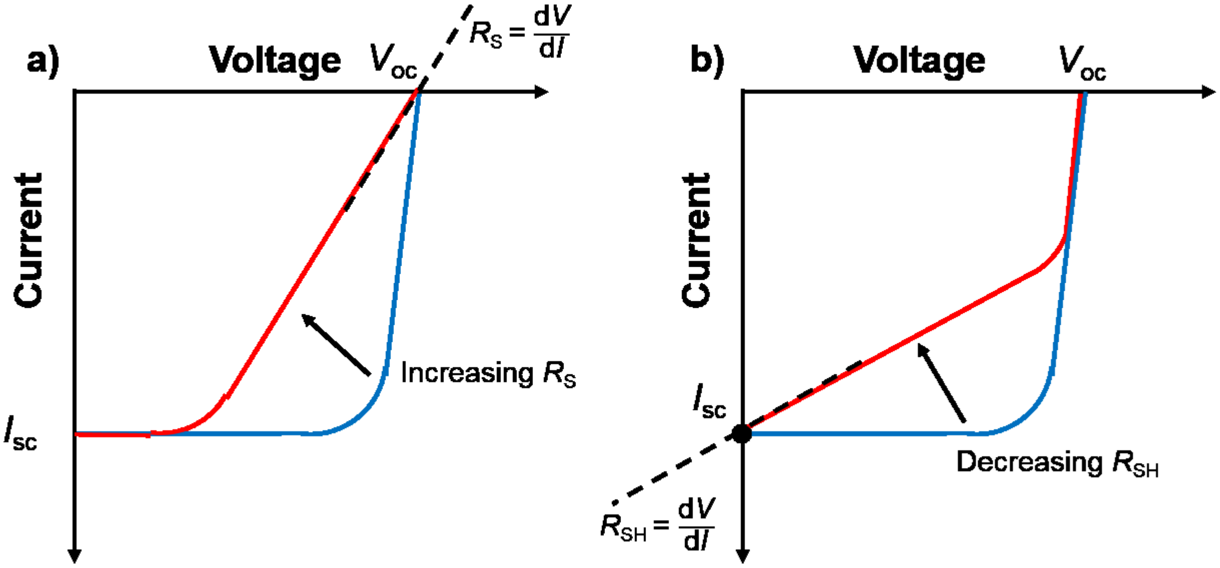

Figure 1.8. An illustration of *I-V* curves showing the detrimental effects on *FF* with a) increasing R_S and b) decreasing R_{SH}.

1.5. Thin Film Formation for Solar Cell Applications

In the context perovskite and organic solar cells, a solid thin-film is formed after nucleation of the material on a substrate and subsequent growth of "domains." The electronic, chemical and structural properties of the material in the thin-film are heavily dependent on the method of deposition. As mentioned before, the most attractive techniques use solutions of the dissolved material to produce the active layers (i.e., solution-processing). Among the myriad of solution deposition techniques that exist (and have been reviewed in-depth),[35] spin-coating is used almost exclusively for both laboratory work and research and development on small-area substrates. While spin-coating is generally not used in commercial applications, it is an ideal technique for high-throughput screening of materials (as is the case for the projects undertaken in this thesis). Other coating and printing methods such as slot die coating, spray-coating, screen printing and ink-jet printing are compatible with roll-to-roll (R2R) printing, which can be employed on large rolls of flexible substrates.

In the studies conducted herein, spin-coating is used exclusively as the method of film-formation (see illustration in **Figure 1.9**). Spin-coating is accomplished by first dispensing the solution onto the substrate. The substrate is then rapidly rotated up to a desired rotational velocity or "spin-speed" (ν_{rot}), measured in revolutions per minute (rpm). Most of the overlying solution is immediately ejected from the surface, leaving a thin "wet" film of solution. As the solvent evaporates during the spin cycle, the material precipitates or crystallizes on the substrate surface, forming a solid dry thin-film.

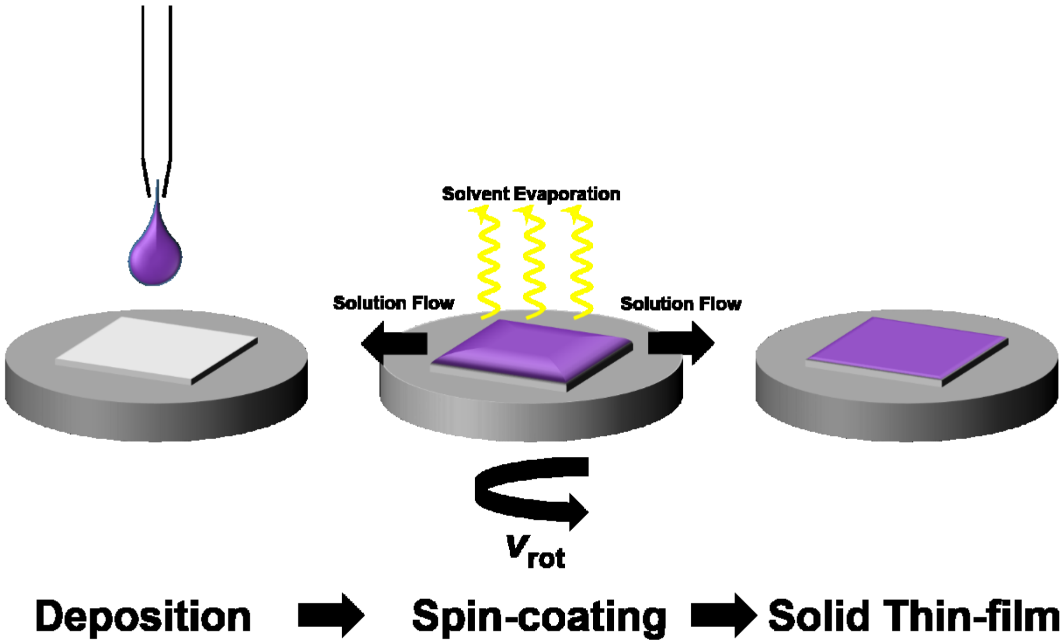

Figure 1.9. An illustration of the stages involved in the spin-casting procedure.

Two characteristics of the resulting spin-cast film that are critical to device performance are: i) film thickness (h) and ii) morphology, or the physical arrangement of the nano-scale domains. Both characteristics are largely dependent on the spin-coating parameters, such as ν_{rot}, initial solution concentration (c_0), viscosity (μ_0), and density (ρ). Since film thickness has been shown to depend on inverse square root of spin speed and is directly proportional to c_0, [36] h can be controlled relatively easily based on the relationship given by Equation (6):

$$h \propto \left(\frac{\mu_0}{\rho \cdot \nu_{\mathrm{rot}}}\right)^{1/2} c_0 . \tag{6}$$

However, the morphology is often more difficult to predict than h. Therefore, controlled experimentation and use of characterization tools to observe the thin-film morphology is necessary to optimize the spin-coating conditions.

1.6. Project Goals

The overall goal of the research projects herein is to investigate the thin film properties of the active layers for the production of low-cost and efficient perovskite (e.g., $CH_3NH_3PbI_3$) and organic solar cells. The goal of the first project (**Chapter 3**) is to fabricate an efficient perovskite solar cell. The methods involved in the deposition of perovskite thin films from solution (i.e., the solution-processing conditions) are probed and correlated to the morphology of perovskite thin films and the performance of the devices. The second goal of the project (**Chapter 4**) is reduce the overall cost of the perovskite solar cell by using cheaper organic hole-transporting materials. The third goal is to assemble a low-cost non-fullerene donor-acceptor pair for the active layer of an organic solar cell (**Chapter 5**). The effect of solution-processing techniques and molecular design on the thin-film morphology, electronic properties and crystallinity are investigated for complementary donor-acceptor pairs.

CHAPTER 2 – CHARACTERIZATION TECHNIQUES

In order to understand how materials form thin films in perovskite and organic solar cells, techniques that elucidate the physical and chemical properties of materials in both bulk form and in thin films are critical.[37] This section describes the characterization techniques and procedures that are applied to perovskite and organic materials and used throughout this thesis.

2.1. Optical Microscopy (OM)

One of the simplest forms of microscopy is optical microscopy (OM). Since images acquired by this technique are of low-resolution, it is limited to detecting micrometre-sized topological film features for rapid screening. However, more powerful techniques are required to view nano-sized film features. OM images were acquired under transmitted light using a Zeiss Axio Imager and processed using the Zeiss Zen software package.

2.2. Scanning Electron Microscopy (SEM)

Scanning electron microscopy (SEM) allows the acquisition of higher-resolution images than OM. A focused beam of electrons is raster scanned across the sample surface. Secondary electrons are ejected from the sample and detected to generate a 2D image of the film surface. In this thesis, SEM was used exclusively to image the surfaces of perovskite films as a tool to detect pinholes and assess film coverage. All surface SEM images were acquired using a Phenom G2 Pro bench-top SEM with backscatter detection, in the laboratory of Prof. Jeffery Dahn.

2.3. Atomic Force Microscopy (AFM)

Atomic force microscopy (AFM) is advantageous over the aforementioned forms of microscopy for the ability to elucidate the three-dimensional (3D) topography of the film surface for quantification of domain sizes and height deviations. For this reason, AFM is especially useful for imaging the surfaces of the active layers in organic solar cells for which the domain sizes and the degree of D-A phase separation are critical to PV performance. AFM is a form of scanning probe microscopy (SPM) in which a physical probe traces across the sample's surface, generating a 3D image (see **Figure 2.1**). As the probe or "tip" is brought near the sample surface, interaction forces (e.g., chemical bonding, Van der Waals, electrostatic forces, magnetic forces, etc.) between the sample and tip cause the cantilever to deflect. On the Bruker Innova AFM used herein, the degree of deflection is monitored by a laser.

A sample can be imaged in one of two ways: under constant height mode or constant force mode. In both cases, a raster scan involves the tip tracing over the surface of the sample in the *xy* plane. During a scan in constant height mode, the *z* position of the cantilever is fixed. Changes in the deflection signal are monitored using a piezoelectric crystal and are recorded as a function of position. In constant force mode, signal from a feedback controller is applied to a piezoelectric crystal which moves the position of the tip (*z*) to maintain constant cantilever deflection. All experiments herein were performed using constant force mode.

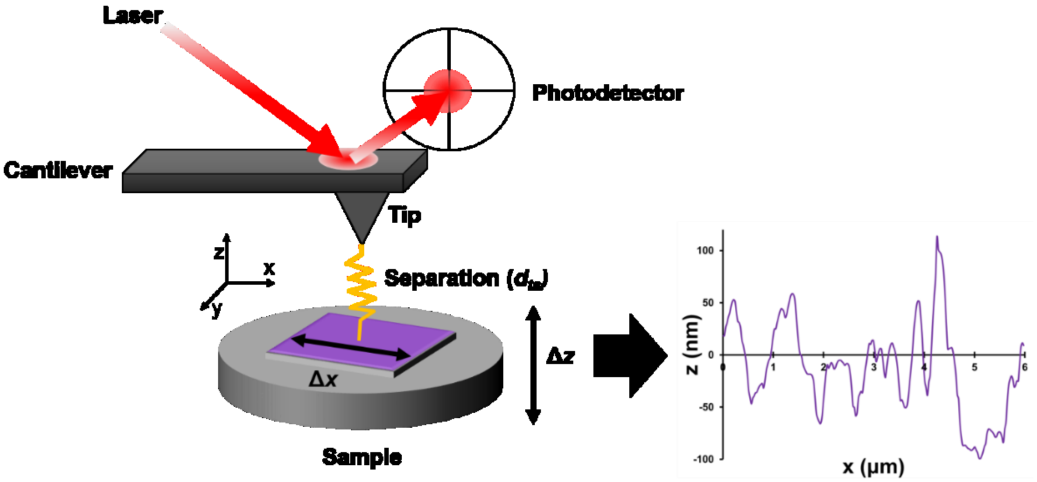

Figure 2.1. An illustration of the operation of an AFM.

There are two common modes of AFM topography: contact and tapping mode. Contact mode is simpler; the cantilever deflection is static as the tip traces over the sample. In contrast, during tapping mode, the cantilever oscillates at a resonant frequency and the amplitude of the oscillation is maintained by the feedback controller. Since the tip alternately contacts and lifts from the sample surface during tapping mode, frictional forces are reduced; the result is a less-destructive technique.

AFM experiments were conducted in tapping mode using a Bruker Innova microscope and NanoDrive (v 8.02) software. The AFM instrument was located in the laboratory of Prof. Ian Hill. Square images of 5 × 5 μm in dimension were acquired by scanning at a rate of 0.3 Hz and sampling 256 points per line. Each image was processed using the Nanoscope Analysis software package.

Three parameters can be used to quantify the surface morphology of a thin film using the Surface Roughness Tool in the NanoDrive program: i) the 3-dimensional image surface area, ii) R_{RMS}, the root mean square (RMS) average of height deviations relative to the mean image data plane, iii) R_{a}, the average of the absolute values of the surface height deviations relative to the mean plane, and iv) $R_{\max}$, the vertical distance between the highest and lowest data points in the image. Z_i is the deviations of the height from the mean data plane in the ith pixel of the image. N is the number of pixels in the image. R_{RMS} and R_{a} are calculated from the following expressions:

$$R_{\mathrm{RMS}} = \left(\frac{\Sigma Z_{\mathrm{i}}^2}{N}\right)^{1/2}, \text{ and} \tag{7}$$

$$R_a = \frac{1}{N} \sum_{i=1}^{N} |Z_i| \ . \tag{8}$$

2.4. X-ray Diffraction (XRD)

XRD experiments are used to: i) identify the materials present and ii) assess the crystallinity of materials within the thin films. Insight into the arrangement of molecules within the crystallites in the films can be gained using Bragg's Law:

$$n\lambda = 2d\sin\theta \tag{9}$$

where n is an integer, λ is the wavelength of incident radiation from the instrument, θ is the angle of incidence of X-rays with respect to the atomic planes of the crystal and d is the separation distance of the atomic planes (i.e., spacing). The Rigaku diffractometer used for the XRD experiments has a Cu-Kα radiation source, so the X-rays produced have a wavelength of 1.54 Å.[38]

XRD patterns were acquired using a Rigaku Ultima IV X-ray diffractometer equipped with a CuKα radiation source, scintillation detector, fixed monochromator and 285 nm focusing slit. The film-coated substrates were mounted into the instrument on a metal platform. Experiments were run using the RINT2200 Right software package with divergence and receiving slit widths of 10 mm and 0.3 mm, respectively, and an offset angle of 0°. Powder patterns were acquired by continuous scans, collecting data as counts per second (cps) and scanning at a rate of 2° per minute. The patterns in each data set were normalized such that the level of the noise is equivalent, that is, the intensity of the pattern at a Bragg angle of 3.05°.

2.5. UV-Visible (UV-Vis) Spectroscopy

UV-Visible spectroscopy (UV-Vis) can be performed on conjugated organic molecules in solid-state thin films or dissolved in solution. The absorption profile provides information about the energy of the light absorbed by the material, which is related to the bandgap energy (E_g), or the difference between the HOMO and LUMO energy levels. E_g is determined from the wavelength of the onset of absorption (λ_{onset}), or the longest wavelength of visible light that is absorbed by the material, and applying Equation (10):

$$E_g = \frac{h \cdot c}{\lambda_{onset}} . \tag{10}$$

In Equation (10), h is the Planck constant (4.136×10^{-15} eV·s) and c is the speed of light in vacuum (2.998×10^{8} m/s). All UV-Vis spectra were acquired using an Agilent Cary 60 spectrophotometer with the Cary Scan software program. For thin-film experiments, the film-coated glass substrates were mounted vertically into the instrument with the glass side facing the radiation source. The instrument was first zeroed using a clean glass slide as a blank. Spectra were acquired by scanning from 900 nm to 200 nm at a rate of 600 nm/min. The spectra were normalized to the peak absorbance value. All solution samples were prepared by stirring a weighed quantity of each material in a vial with $CHCl_3$ or chlorobenzene (CB) as the solvent until dissolved. After transferring the solutions into quartz cuvettes, UV-Vis spectra were acquired by scanning from 900 nm to 200 nm at a rate of 600 nm/min.

2.6. Photoluminescence (PL) Spectroscopy

The term photoluminescence (PL) refers to the emission of photons following photoexcitation. Photoexcitation occurs when electrons are promoted to higher-energy states upon absorption of light. As the electrons relax to the ground-state via various mechanisms, photons can be re-radiated and detected by the PL instrument. During PL experiments, the sample is irradiated by visible light of a particular wavelength (excitation wavelength, λ_{ex}) and an emission spectrum is recorded.

The film-coated substrates were mounted vertically into the instrument with the film-side facing the radiation source at a 45° angle. For emission experiments, λ_{ex} was selected as the wavelength at which maximum absorption for the particular material occurs in a thin film (determined from the results of thin-film UV-Vis experiments). Excitation and emission slit widths were set to 20 nm. Spectra were acquired by scanning at a rate of 600 nm/min.

2.7. Cyclic Voltammetry (CV)

CV was used to measure the onset of oxidation and reduction of the materials, which corresponds to the ionization potential (HOMO) and electron affinity (LUMO), respectively. This information is critical in D-A organic solar cells, where the efficient charge separation at the D-A interface depends on appropriate alignment of the HOMO and LUMO energy levels.

CV experiments for organic materials were conducted using solution samples. A BASi CV instrument was equipped with an N_2 bubbler as well as an Ag/AgCl electrode, Pt wire and glassy-carbon electrode as the pseudo-reference, counter electrode and working electrode, respectively. Measurements were conducted using the BASi Epsilon EC software program. Samples were prepared with a concentration of ~1 mg/mL by dissolving each material in anhydrous CH_2Cl_2 with ~0.1 M tetrabutylammoniumhexafluorophosphate ($TBAPF_6$) as the supporting electrolyte. All solutions were purged with $N_2(g)$ and then scanned at 50, 100 and 150 mV/s as-is and at 100 mV/s after the addition of a ferrocene

(Fc) standard. The resulting voltammograms were referenced to the oxidation potential of Fc/Fc$^+$, which corresponds to the HOMO energy level at a value of 4.80 eV below the vacuum level.[39] The values of the HOMO and LUMO energy levels of the organic compounds were obtained by comparing the onset of oxidation and reduction, respectively, to the HOMO energy of ferrocene.

CHAPTER 3 – THIN FILM FORMATION IN PEROVSKITE SOLAR CELLS

3.1. Background

3.1.1. Solution-Processed Perovskite Solar Cells

The combination of interesting material properties and the reported high performance of perovskite solar cellss make perovskites an attractive field of study. For this reason, it was a collective decision to develop a research program in the Welch and Hill laboratories focused on the development and characterization of materials for PSCs.

Before the study of novel materials could be conducted, it was necessary to develop an in-house fabrication procedure for reproducible and high-efficiency standard devices to serve as controls. While many reports in the literature exist, fabricating a PSC is not a straight-forward process and ultimately depends on film formation of the active layer. This chapter serves as an account of the challenges encountered during the development of a functional perovskite solar cell.

3.1.2. Active Layer Components and Device Architecture

There are two general types of active layers for PSCs: Meso-structured and planar heterojunction (PHJ) (see **Figure 3.1)**. In mesostructured PSCs the perovskite material is housed within a mesoporous scaffolding of semiconducting (e.g., TiO_2)[17] or insulating (Al_2O_3)[40,41] nanoparticles. In contrast, a planar heterojunction perovskite solar cell does not contain the mesoporous oxide layer; the active layer is simply an unsupported thin film of perovskite material.[42,43] While preliminary mesoporous devices were fabricated (results are not reported in this thesis), the PHJ architecture was selected for further optimization due to its simplicity in construction.

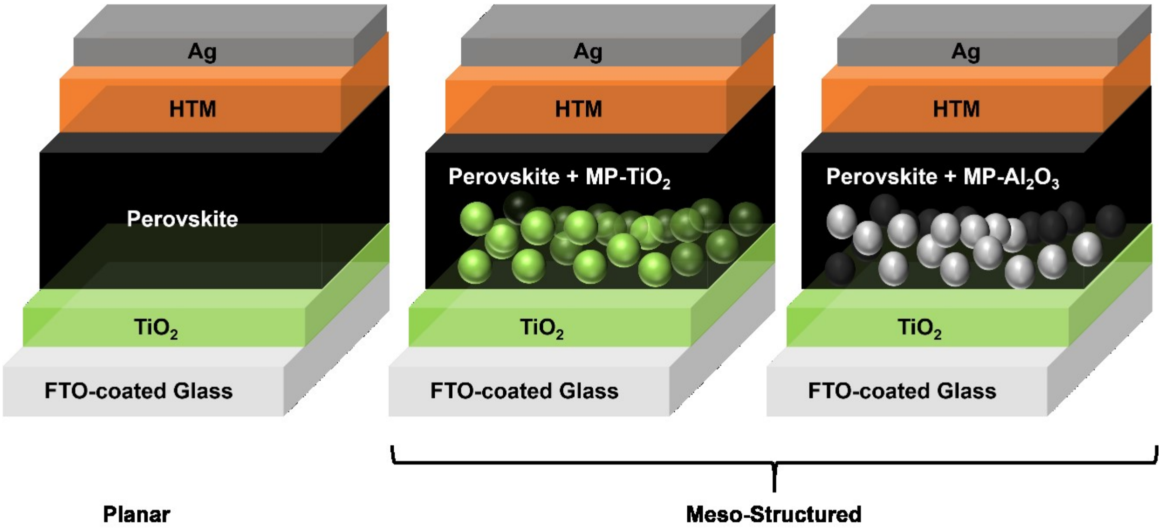

Figure 3.1. Device architectures for planar and meso-structured perovskite solar cells.

For planar perovskite solar cells, a mixed halide perovskite ($CH_3NH_3PbI_{3-x}Cl_x$) is a preferred material for planar architectures because of the longer electron-hole diffusion length[44] than its pure-halide[45] counterpart ($CH_3NH_3PbI_3$). Nevertheless, pure-halide (i.e., $MAPbI_3$) perovskites have been used in planar cells with high efficiencies.[24,46] For this reason, $MAPbI_3$ is the perovskite material used in the studies throughout this thesis.

Regardless of the material selection, film uniformity of the perovskite active layer is critical for high performance devices and is difficult to achieve. It has been demonstrated that controlled vapour deposition is an effective method that can achieve uniform films and highly efficient planar cells with both mixed- and pure-halide perovskite active layers.[24,47] However, this method is expensive and challenging on an industrial scale. On the other hand, solution-processing is a cost-effective method for active layer deposition and is necessary to realize large-scale R2R production of perovskite solar cells.[48]

3.1.3. Methods of Solution-Processed Perovskite Thin Films

One of the most important factors that influences the performance of a planar heterojunction perovskite solar cell is the active layer film morphology (e.g., crystal grain size, crystal distribution, overall uniformity and coverage, absence of pinholes, etc.). Furthermore, the film morphology is largely dependent on the processing methods and conditions applied during film formation.

Three well-documented methods exist for perovskite film formation from solution:

i) Co-Deposition. The perovskite is formed in-situ by spin-coating a single solution containing the two constituents (i.e., methyl ammonium iodide (CH_3NH_3I or "MAI") and lead (II) iodide (PbI_2)).[17,49]

ii) Sequential Dip-Coating (SDC). A film of the metal halide is first deposited on the substrate via spin-coating and then dipped into a solution containing the ammonium salt. In this method, (which was first documented by Liang *et al*),[50] PbI_2 and MAI react to form the final perovskite film. This method has proven to be an effective active-layer processing technique in perovskite solar cells, helping to fabricate devices that achieve over 15% efficiency.[46,51] In addition, modifications to the two-step method to control PbI_2 crystal growth via solvent engineering have been discovered that yield devices with over 16%.[52]

iii) Sequential Spin-Coating (SSC). Similar to the SDC method, a thin film of PbI_2 is first deposited onto the substrate.[53] Subsequently, a film of MAI is spin-coated on top of the PbI_2 layer. Heating the layers stimulates the interdiffusion of MAI ions into the underlying PbI_2 film, forming the perovskite, $MAPbI_3$.

The first goal in this project was to screen previously-reported methods for perovskite film formation. However, processing conditions vary from lab to lab – the optimal conditions for film formation reported in the literature are not universal. Furthermore, it was found that many subtle techniques and "tricks-of-the-trade" are often excluded from experimental sections of "high-impact" papers. For these reasons, it was important to identify variables and perform controlled sets of optimization experiments to develop a custom in-house method for perovskite film formation. Methods for both SDC and SSC were developed and discussed herein.

3.2. Sequential Dip-Coating Experimental Methods

3.2.1. PbI_2 and $MAPbI_3$ Thin Films

Thin films of PbI_2 and $MAPbI_3$ were prepared via spin-coating on TiO_2-coated glass substrates to determine the optimal processing conditions. The procedure for making these films was as follows.

25 mm × 25 mm glass slides were first cleaned in the following order: i) scrubbing with mixture of deionized (DI) H_2O and Sparkleen® detergent, ii) rinsing with DI H_2O, iii) rinsing with acetone, iv) rinsing with isopropanol, v) drying under a stream of air and iv) UV/ozone treatment for 15 min.

The clean substrate was first mounted onto the chuck of a Laurell spin-coater. To form the dense TiO_2 layer, the precursor solution (see **Appendix A** for preparation procedure) was dispensed onto the center of the 625-mm^2 substrate through a 0.45 µm PVDF filter using a 1 mL syringe in one aliquot of 0.3 mL. The film was then spun at 2000 rpm (ramp = 2050 rpm/s) for 45 seconds. The coated substrates were placed in clean Pyrex® petri dishes and then placed in a sintering oven. The temperature was ramped up to 500 °C at a rate of 30 °C/min and held at 500 °C for 30 min. The films were then removed from the oven and cooled to room temperature (RT).

To form the PbI_2 films, PbI_2 solutions with *N,N*-dimethylformamide (DMF) as the solvent were prepared (see **Appendix A** for preparation procedure). At a concentration of 1.0 M, the solution was supersaturated at RT and had to be cast at an elevated temperature. The dilute solutions (i.e., 0.5 M and 0.75 M) were cast at RT.

The TiO_2-coated glass substrates were used either heated (on a hotplate) or unheated (at RT). After placing the substrate onto the chuck of the spin-coater, approximately 0.3 mL of solution was retracted from the vial using a 1.0 mL syringe and dispensed onto the center of the substrate through a 0.45 μm PTFE filter in a single aliquot. The spin-coater was then run at speeds of either 1000, 3000 and 5000 rpm for 30 s. For heated substrates, the average elapsed time from removal of the substrate from the heat source and solution deposition was 30 s.

The dipping solutions were prepared by weighing the dried MAI (dried in a vacuum oven overnight prior to solution preparation) into a 30 mL beaker, adding the appropriate amount of isopropanol to form a 10 mg/mL solution and then stirring the solution at RT (using a stir bar and a hotplate) for approximately 15 min. The synthesis of MAI is described in **Appendix B**. To initiate the conversion into a $MAPbI_3$ perovskite film, the PbI_2 films were briefly rinsed a beaker containing isopropanol, removed, and then immersed in the beaker containing the MAI solution. The beaker was gently swirled by hand for 60 s to promote uniform diffusion of the MAI across the entire PbI_2 film surface. After 60 s, the substrate was removed from the dipping solution using tweezers, rinsed in a beaker of isopropanol and finally dried under a stream of filtered air or N_2. The perovskite films were characterized as-is without further processing and stored in an Ar-filled glovebox. The SDC procedure is illustrated in **Figure 3.2**.

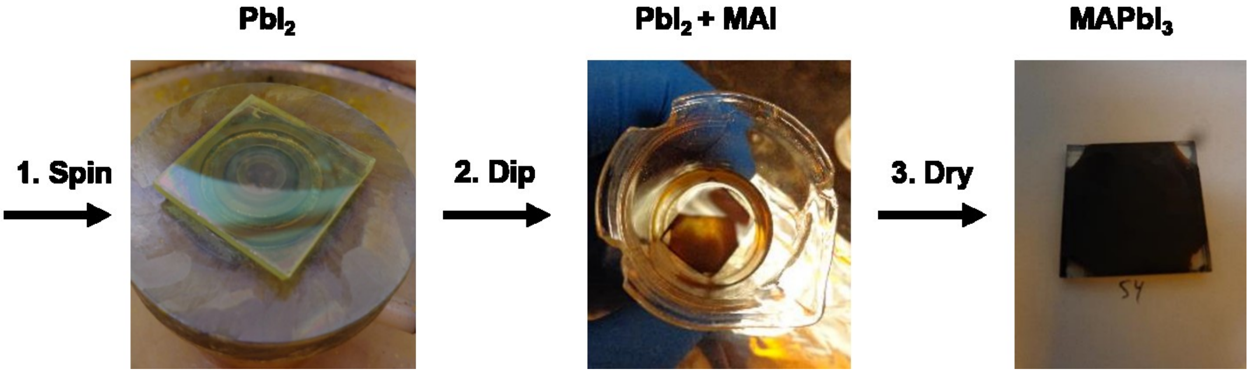

Figure 3.2. Photographs depicting the stages of the SDC procedure.

3.2.2. Perovskite Solar Cell Fabrication Using Sequential Dip Coating

The 25 mm × 25 mm FTO-glass substrates were first cleaned by the following procedure: i) scrubbing the surface with lab detergent (Sparkleen®) and DI H_2O, ii) sonicating in a solution of DI H_2O and Sparkleen® for 15 min, iii) sonicating in acetone for 15 min, iv) sonicating in ethanol for 15 min, iv) rinsing in DI H_2O and v) UV/ozone treatment for 20 min.

The TiO_2 film was deposited immediately following UV/ozone treatment using the method described in **Section 3.2.1**. Before entering the oven, the four corners of the substrate were carefully wiped with a CleanSwab® dampened with 37% HCl to expose the underlying FTO. The substrates were then placed in a Pyrex® petri dish and then baked in the sintering oven at 500 °C for 30 min. After cooling to room-temperature, the substrates were either heated on a hotplate to establish the desired $T_{\text{substrate}}$ or used unheated.

Only 1.0 M PbI_2 solutions were used to make PbI_2 films for PSCs. For deposition on heated substrates, the substrates were removed from the hotplate and quickly placed onto the chuck of the spin-coater. Approximately 0.3 mL of the hot PbI_2 solution was retracted into a 1.0 mL syringe and then quickly dispensed onto the center of the heated substrate through a 0.45 μm PTFE filter in one aliquot. The spin-coater was then run at speeds of either 1000 or 3000 rpm for 30 s. The four corners were then wiped with CleanSwab® dampened with DMF to expose the underlying FTO. The PbI_2 films were converted into $MAPbI_3$ in all devices following the procedure outlined in **Section 3.2.1**.

To form the hole-transporting layer, the solution containing p-doped spiro-OMeTAD (see **Appendix A** for preparation procedure) was dispensed onto the perovskite layer through a 0.45 μm PTFE filter and then spun at a rate of 4000 rpm for 30 s under ambient conditions. The four corners were then wiped with a CleanSwab® dampened with chlorobenzene to expose the underlying FTO.

The top metal contact was deposited via thermal evaporation. The substrates were loaded top-down into a metal mask and then mounted in a custom-built bell-jar thermal evaporator. A silver slug was used as the metal source in a tungsten-wire basket. The bell-jar was evacuated using a diffusion pump to a pressure less than 4×10^{-6} Torr. A 75-nm thick layer of silver was deposited onto the substrates by thermal evaporation. After removal from the bell-jar, the devices were immediately transferred into an Ar-filled glovebox where they were tested and subsequently stored.

3.3. Perovskite Solar Cell Device Characterization

For photovoltaic measurements, solar cell devices were illuminated using a calibrated light source. A National Institute of Standards and Technology (NIST)-traceable calibrated photodiode (Newport 818-UV-L) in conjunction with a near infrared absorptive filter (Thorlabs NENIR60A) was used to measure the output power density of the Xe arc lamp (Sciencetech SS0.5K) below 800 nm, where the spectrum of the source closely matches the solar spectrum and covers the absorption range of all photoactive materials used in this thesis. This provided a power density of 100 (±1) mW/cm^2 of AM 1.5G spectrum over relevant wavelengths, or the equivalent of 1.00 Suns. Each device had an area of 0.032 cm^2 and was tested in separate measurements. One exposed FTO corner was contacted with the negative (black) electrode and the Ag top contact of a device was contacted by gently approaching a thin gold-wire that was connected to the positive (red) electrode (illustrated in **Figure 3.3**). Current-voltage (I-V) curves were then measured using a Keithley source-measure unit, scanning from +2.0 V to short-circuit (0.0 V) unless otherwise stated.

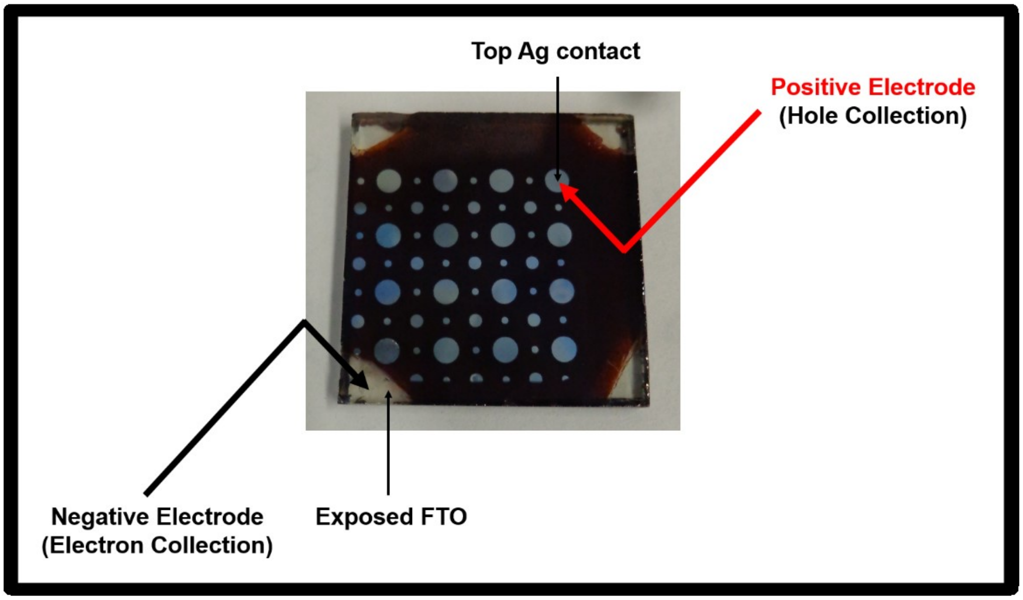

Figure 3.3. A photograph of a substrate with 16 completed PSC devices. The points of contact to the positive and negative electrode are indicated by red and black arrows, respectively.

3.4. Results and Discussion – Sequential Dip-Coating

While investigating the sequential dip-coating (SDC) method for perovskite thin film formation, it was found that the morphology of the final perovskite film is largely dependent on the morphology of the initial PbI_2 film. A major issue was the formation of large, needle-like crystals of PbI_2, which formed cloudy, non-continuous films with poor substrate-coverage, unsuitable for the active layer of PSCs. Perovskite active layers with maximum surface coverage are desired in devices to prevent shunt pathways and shortcircuits. Therefore, methods that generate dense perovskite layers with a uniform distribution of crystallites are favoured.

Rapid cooling of the hot solution during spin-coating of the PbI_2 was identified as a cause for the large-crystal growth. Various spin-coating parameters were systematically controlled to investigate the effect on film morphology. The solution concentration (C_{solution}), spin speed (ν_{rot}), and substrate temperature ($T_{\mathrm{substrate}}$) were found to have the most significant effect on film morphology. Conditions including the solution temperature (T_{solution}, **Figure C1**) and atmosphere (**Figure C2**) were also investigated and are discussed in **Appendix C**.

3.4.1. Solution Concentration (C_{solution}) and Spin Speed

The most common solution used in the literature for the deposition of the PbI_2 film during the two-step perovskite deposition method is a 1.0 M (461 mg/mL) solution in DMF. While this solution has proven to yield thick, uniform films in devices with high efficiencies, its use is problematic: it is a supersaturated solution at room temperature and must be deposited at elevated temperatures (i.e., “hot-cast”). Following this procedure, there is a tendency for the PbI_2 to rapidly crystallize on the substrate before the film is spun. By reducing the concentration, it is possible to deposit a homogeneous solution of PbI_2 without the need for hot-casting. **Figure 3.4** depicts OM images of PbI_2 films deposited from solutions of different concentrations and different spin speeds onto substrates held at room temperature. It was observed that film uniformity and coverage increases with increasing spin velocity – a phenomenon that was also observed by Cohen *et al.*[54] The crystalline domain sizes decrease with increasing spin velocity. This is attributed to the higher rate of solvent evaporation as the spin speed is increased. From the optical microscope images, it is clear that perovskite films cast from 1.0 M solutions provide better substrate coverage and are more desirable as active layers in PSC devices than those cast from more dilute solutions (**Figure 3.5**). For this reason, all further modifications to processing conditions in this study were performed using 1.0 M solutions.

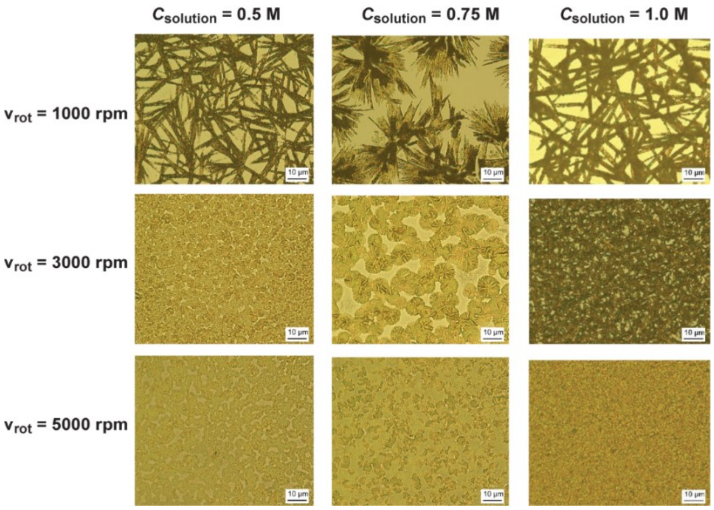

Figure 3.4. Optical microscope images of PbI_2 films spin-cast on TiO_2 compact films showing the effect of precursor-solution concentration. The 0.5 and 0.75 M solutions were deposited at room temperature and spun for 90 s. The 1.0 M solution was deposited at 70 °C and spun for 30 s. All films were cast onto room-temperature substrates.

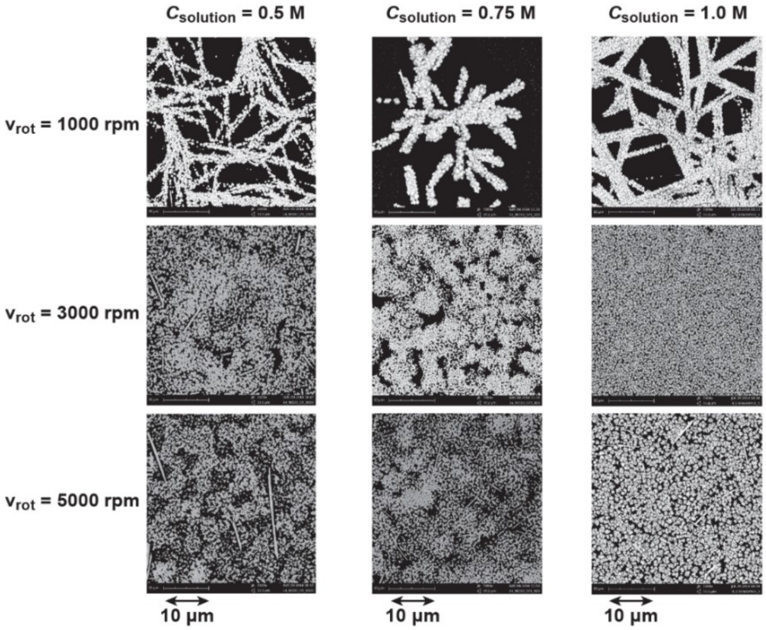

Figure 3.5. SEM images of the $CH_3NH_3PbI_3$ films after conversion of the PbI_2 films via SDC, showing the effect of precursor-solution concentration.

3.4.2. Substrate Temperature ($T_{\text{substrate}}$)

To reduce the rate of cooling of the solution after dispensing it onto the cold substrate, films were cast onto heated substrates (from 50 °C up to 150 °C) and compared to those cast onto unheated substrates (**Figure 3.6**). It is important to note that the substrate cools considerably between the time of heating and the time when the solution is dispensed. To determine the substrate temperatures ($T_{\text{substrate}}$), a thermocouple probe was attached to the surface of the substrate using Kapton® tape. The initial substrate temperature ($T_{\text{substrate,initial}}$) was recorded while the substrate was resting on the hotplate with a surface temperature of T_{hotplate}. These measurements were recorded after at least 10 minutes of heating. The final substrate temperature ($T_{\text{substrate,final}}$) was recorded 30 s after the substrate was removed from the heat source and placed on the chuck of the spin-coater. The measurements for substrate temperatures are listed in **Table 3.1**.

It was observed that glass microscope slides, which are considerably thinner than the FTO-coated glass substrates used for device fabrication, have a higher rate of cooling. For instance, if a glass microscope slide and an FTO-coated glass substrate are heated to 100 °C and 75 °C, respectively, both will cool to a temperature of 60 °C after being placed on the chuck of the spin-coater for 30 s (i.e., $T_{\text{substrate,final}}$ is ~ 60 °C).

Table 3.1. Initial and final (i.e., after 30 s) temperatures of glass and FTO substrates heated on a hotplate set to a surface temperature of T_{hotplate}.

$T_{\text{substrate,initial}}$ (°C)	T_{hotplate} (°C)	$T_{\text{substrate,final}}$ (°C) (Glass)	$T_{\text{substrate,final}}$ (°C) (FTO)
50	66	40	46
75	92	49	59
100	117	60	69
125	135	65	85
150	160	73	105

Figure 3.6 depicts the films cast on substrates heated to 100 °C just prior to deposition are more uniform and consist of smaller domains than those cast on room-temperature substrates. The additional heating step in the processing procedure is beneficial for two reasons: First, water is removed from the surface on the substrate, allowing better contact with PbI_2 ions and nucleation sites. Second, the heated substrate helps to maintain the elevated temperature of the supersaturated solution, thus preventing rapid cooling of the solution and corresponding crystallization of the solute. For example, it is observed that the films spun on unheated substrates at 1000 rpm consist of large needle-shaped crystals, whereas the films cast on heated substrates consist of significantly smaller grains. By spin-coating at a slow speed and heating the substrate (e.g., 1000 rpm), thicker films can be produced that provide comparable coverage to films spun at higher speeds.

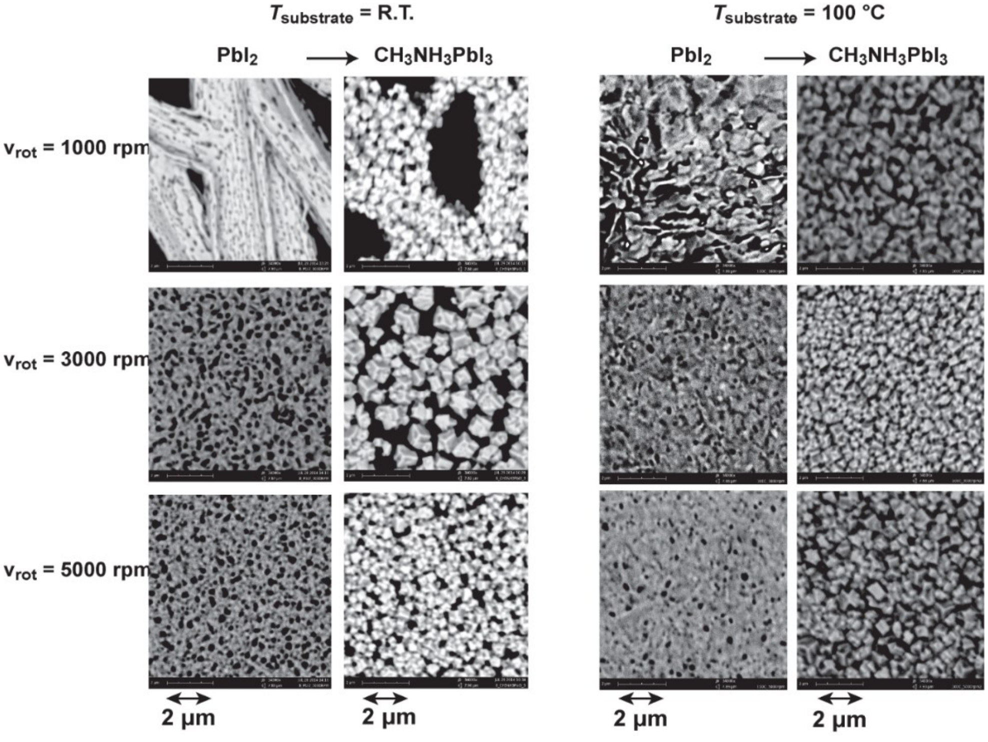

Figure 3.6. The effect of spin velocity and substrate temperature. SEM images of PbI_2 films spin-cast on TiO_2 compact films at different temperatures and the corresponding $CH_3NH_3PbI_3$ films after conversion via dipping. All films were spin-cast from a 1.0 M PbI_2 solution in DMF held at 70 °C and spun for 30 s.

Although the film cast on a R.T.-substrate consists of needle-like crystals and large voids, substrate temperatures of 50 °C and above resulted in more uniform surface coverage and no needle growth (see **Figure 3.7**). Intermediate temperatures (50 and 75 °C) resulted in a honeycomb PbI_2 morphology whereas the films cast on the substrates at the highest temperatures (100, 125, 150 °C) consisted of larger grains. After conversion to the perovskite via dipping into the MAI solution, the films cast on all substrates heated to temperatures above 50 °C display similar morphologies that consist of micron sized cuboidal crystallites.

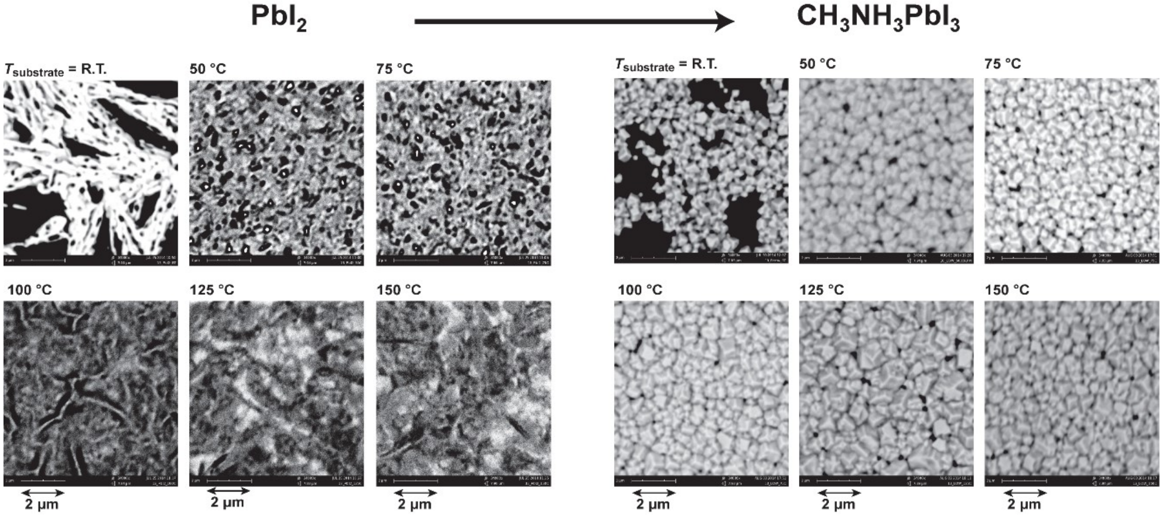

Figure 3.7. The effect of substrate temperature. SEM images of PbI_2 films spin-cast on TiO_2 compact films at different temperatures and the corresponding $CH_3NH_3PbI_3$ films after conversion via dipping. All films were spin-cast from a 1.0 M PbI_2 solution in DMF held at 70 °C at a spin speed of 3000 rpm for 30 s.

3.4.3. Device Performance Using Sequential Dip Coating

Based on the optical microscope and SEM images acquired for the PbI_2 films, it is clear that substrate temperature has a significant effect on morphology. To correlate the morphological changes to PV performance, PHJ perovskite solar cell were fabricated on substrates heated to a range of temperatures.

When keeping the spin speed constant at 3000 rpm, increasing the temperature of the substrate decreases cell performance in terms of efficiency and current density (**Figure 3.8** and **Table 3.2**). However, the devices with PbI_2 films cast at 1000 rpm benefit from substrate heating (**Figure 3.9** and **Table 3.3**). By heating the substrate to 100 °C prior to deposition, the resulting devices display a higher shunt resistance. This is in agreement with the optical microscope images of the PbI_2 and perovskite films; films cast on the heated substrates show visibly greater coverage and correspondingly higher R_{SH}.

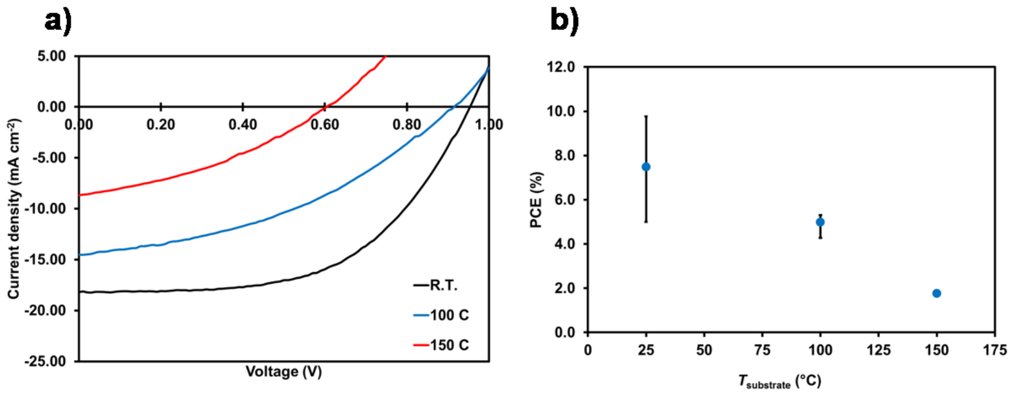

Figure 3.8. a) *J-V* curves for the best-performing PSCs with PbI_2 films deposited at 3000 rpm on substrates heated and unheated substrates. b) A plot of the average *PCE* of PSC devices with PbI_2 films deposited at 3000 rpm as a function of substrate temperature. For each substrate temperature, error bar range extends from the lowest- to the highest-observed *PCE* among five representative devices.

Table 3.2. *J-V* performance metrics for the best-performing PSCs fabricated with PbI_2 films deposited at 3000 rpm on substrates heated and unheated substrates. The average metrics for five sample devices (at each substrate temperature) are also provided with standard deviations in the brackets.

v_{rot} (rpm)	$T_{substrate}$ (°C)		V_{oc} (V)	J_{sc} (mA cm^{-2})	*PCE* (%)	FF
3000	R.T.	Best Cell	0.97	−18.20	9.76	0.56
		Average	0.93(0.02)	−18.12(0.26)	7.48(2.01)	0.44(0.11)
3000	100	Best Cell	0.93	−14.52	5.31	0.39
		Average	0.92(0.01)	−14.43(0.56)	4.99(0.42)	0.38(0.02)
3000	150	Best Cell	0.62	−8.67	1.91	0.36
		Average	0.56(0.07)	−8.79(1.01)	1.76(0.14)	0.36(0.00)

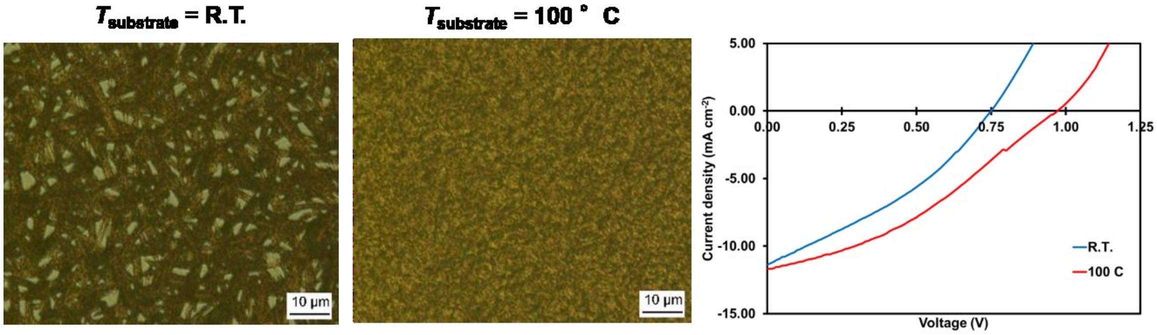

Figure 3.9. *J-V* curves of the best-performing PSCs with PbI_2 films deposited at 1000 rpm on substrates heated to different temperatures. OM images of the active layers are also shown.

Table 3.3. *J-V* performance metrics of the best-performing PSCs with PbI_2 films deposited at 1000 rpm on substrates heated to different temperatures. The average metrics for five sample devices (at each substrate temperature) are also provided with standard deviations in the brackets. The shunt resistances listed are for the best-performing devices only.

v_{rot} (rpm)	$T_{substrate}$ (°C)		V_{oc} (V)	J_{sc} (mA cm^{-2})	*PCE* (%)	FF	Shunt resistance (Ω cm^{-2})
1000	RT	Best Cell	0.75	−11.39	2.86	0.34	9.0×10^{-4}
		Average	0.72(0.08)	−9.32(2.85)	1.99(0.88)	0.28(0.03)	-
1000	100	Best Cell	0.99	−11.67	3.94	0.34	2.1×10^{-5}
		Average	0.89(0.03)	−10.54(2.92)	2.67(1.09)	0.27(0.04)	-

3.5. Experimental Methods – Sequential Spin Coating

Inconsistencies in device performance using the SDC method led to an investigation of an alternative method of perovskite film formation: sequential spin-coating (SSC), which is illustrated in **Figure 3.10**.

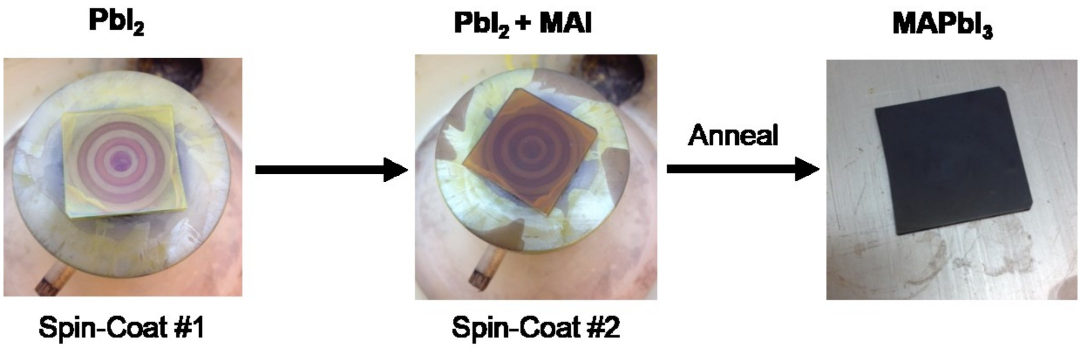

Figure 3.10. Photographs of films depicting stages of the SSC procedure.

TiO_2 films were first prepared on cleaned glass substrates as per the procedure outlined in **Section 3.2.1.** After the substrates were cooled to RT, PbI_2 films were spin-coated onto the TiO_2-coated substrates by dispensing the hot (70 °C) PbI_2 solution (1.0 M in DMF) onto the substrate through a 0.45 μm PTFE filter using a syringe and then spinning at 6000 rpm for 60 s. The substrates were immediately removed from the spin-coater and placed on a hotplate with a surface temperature of 70 °C for 5 min to remove excess DMF. The substrates were cooled to RT before depositing the MAI layer.

MAI solutions of varying concentrations were prepared dissolving dry MAI crystals in isopropanol in 4 mL glass Teflon-capped vials and stirring at room temperature. MAI films were spin-coated onto the dry PbI_2 films by dispensing the MAI solution onto the substrate through a 0.45 μm PVDF filter using a syringe and then spinning at 6000 rpm for 60 s. The PbI_2/MAI layered films were then annealed on a hotplate at 100 °C for 1 h. Films for all PSC devices were annealed in an Ar-filled glovebox, for reasons that are explained in **Section 3.6.1**.

3.6. Results and Discussion – Sequential Spin Coating

3.6.1. Annealing Conditions

After both the PbI_2 and MAI layers have been deposited, heat is required to drive the interdiffusion of MAI into the lattice of the underlying PbI_2. Lead iodide can be described as a "quasi two-dimensional" material since the 2D atomic planes of lead iodide are arranged in layered stacks.[55] The spaces between the atomic planes have been shown to facilitate the intercalation of small molecules, such as methylammonium iodide.[52] To confirm the presence of $CH_3NH_3PbI_3$ in the thin films, the experimental XRD patterns were compared against a simulated pattern of $CH_3NH_3PbI_3$ obtained from the crystal structure data reported by Stoumpos *et al*. (see **Figure 3.11**). Annealing under inert atmosphere at

100 °C for 1 hour results in full conversion to the perovskite, as indicated by absence of the 110 PbI_2 peak ($2\theta = 12.6°$) in the thin-film XRD patterns **Figure 3.11**. On the other hand, the films that were annealed in ambient conditions for 1 hour contained unconverted PbI_2. It is possible that the moisture in air contributes to degradation of the perovskite into lead iodide, which has been demonstrated in a previous study by Kelly *et al.*[56] No significant differences were observed in terms of morphology for the films annealed in ambient versus those annealed in inert atmosphere (see **Figure 3.12**). Based on these results, all subsequent perovskite films were annealed in an Ar-filled glovebox.

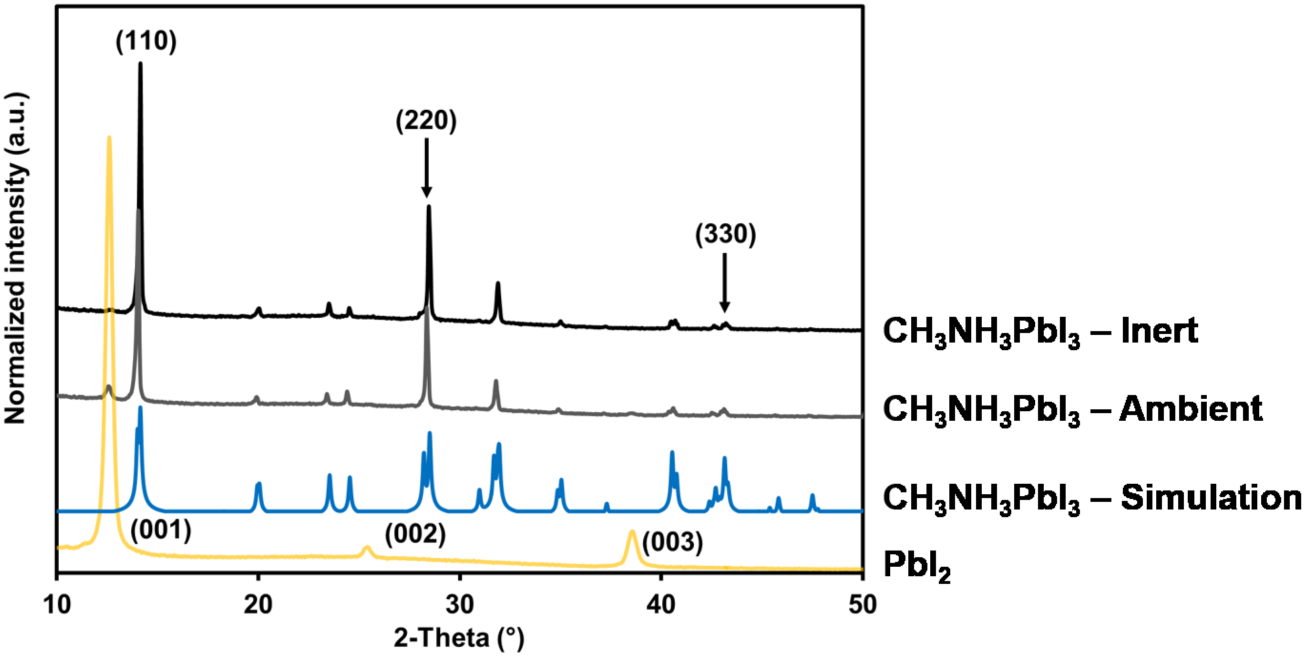

Figure 3.11. XRD pattern of a PbI_2 thin film on TiO_2 compared to $CH_3NH_3PbI_3$ films after annealing at 100 °C for 1 h in inert (black trace) or ambient (grey trace) atmosphere. The simulated powder pattern (blue trace) was obtained from the $CH_3NH_3PbI_3$ crystal structure data (in the form of a cif file) reported by Stoumpos *et al.*[18] The corresponding lattice planes for each of the diffraction peaks in the PbI_2 pattern ((001), (002) and (003)) were identified according to Burschka *et al.*[51] The peaks corresponding to the major lattice planes in the $CH_3NH_3PbI_3$ patterns ((110), (220) and (330)) were identified based on the analysis performed by Dualeh *et al.*[57]

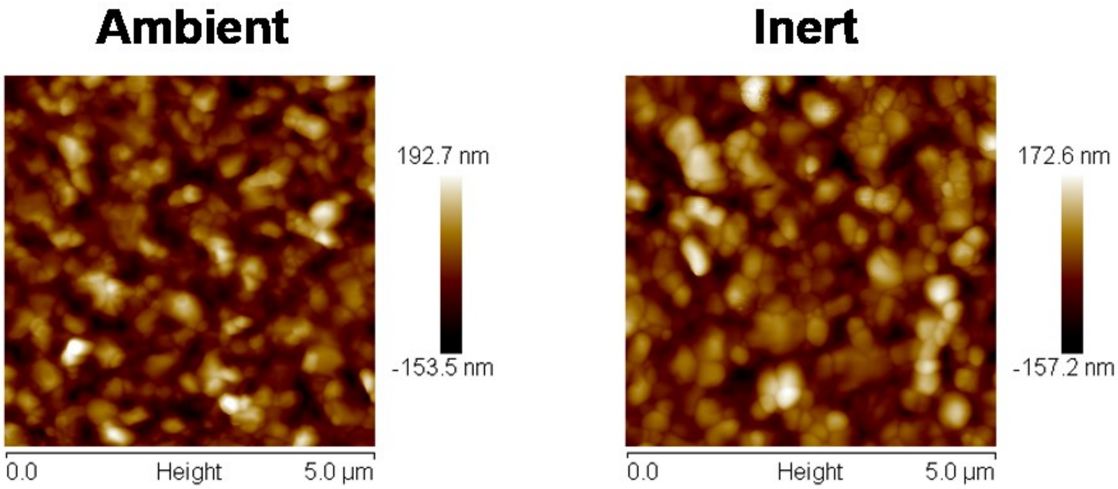

Figure 3.12. 2D AFM topographical maps of the surface of two perovskite films formed by the sequential spin-coating method – one was annealed in ambient and one annealed in an inert atmosphere.

3.6.2. MAI Concentrations

In order to establish the correct stoichiometry between the PbI_2 and MAI layers for complete perovskite conversion, a series $CH_3NH_3PbI_3$ films were formed by sequential spin coating using different concentrations of MAI solution. For all films, the PbI_2 spin speed (6000 rpm), PbI_2 solution concentration (1.0 M), MAI spin speed (6000 rpm), PbI_2-MAI annealing time (60 min) and annealing temperature (100 °C) were kept constant.

XRD was used to detect the phases of the materials present in the final films (**Figure 3.13**). The intensity of the (110) PbI_2 peak ($2\theta = 12.6°$) decreased linearly with increasing MAI concentrations, indicating that less PbI_2 remains unreacted in the film (**Figure 3.14**). Visually, the films with a higher MAI loading appear darker and more optically dense due to the higher quantities of $MAPbI_3$ (see photographs of films in **Figure 3.13**). As shown in the XRD patterns in **Figure 3.13**, perovskite thin films spin-coated with MAI solutions less than 50 mg/mL all contained (001), (002) and (003) PbI_2 diffraction peaks of significant intensity. A plot of the relative intensity of the (001) PbI_2 peak in the perovskite powder patterns as a function of MAI concentration is provided in **Figure 3.14** and shows a linear decrease in peak intensity with increasing MAI concentration. This provides evidence for presence of unreacted starting material and incomplete perovskite conversion when using dilute MAI concentrations.

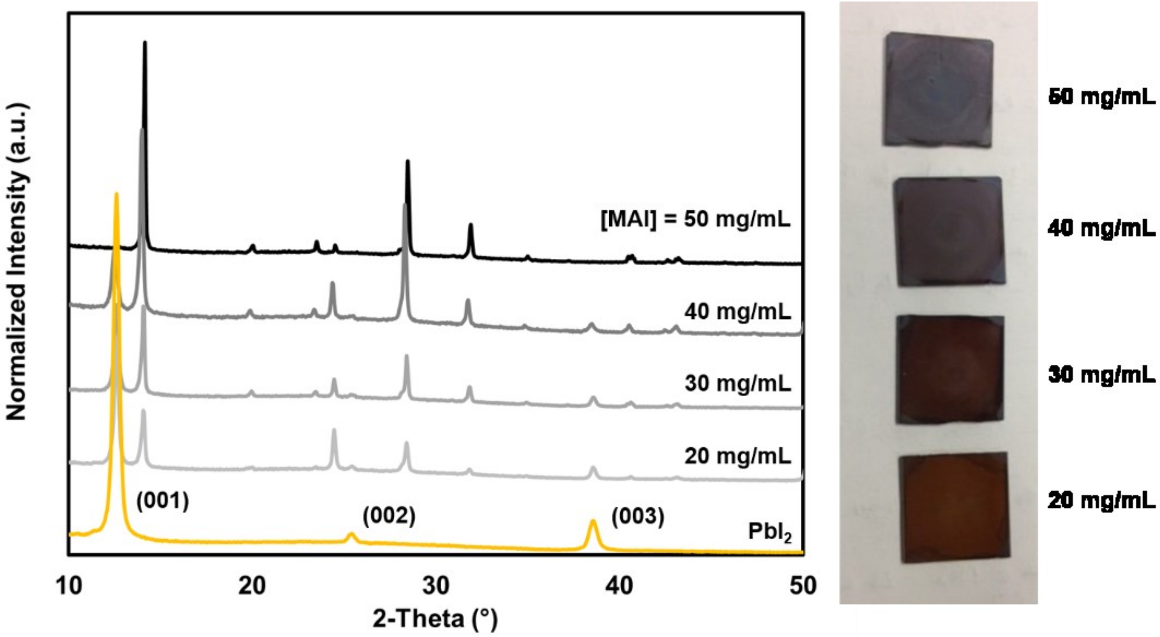

Figure 3.13. XRD patterns of $MAPbI_3$ thin film formed via the sequential spin-coating method with different concentrations of MAI precursor solution. All films were annealed at 100 °C under inert atmosphere after spin-coating the MAI and PbI_2 layers. A powder patterns of a PbI_2 neat film is included at the bottom of the plot for comparison. Also shown are photographs of the $MAPbI_3$ films, showing progressive darkening of the film with increasing MAI concentration.

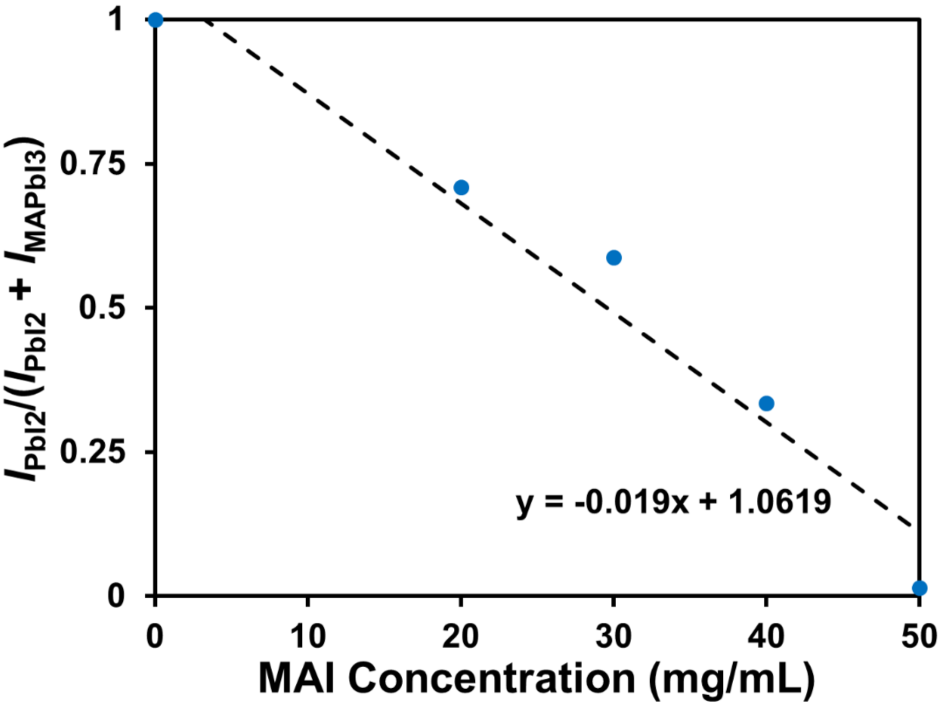

Figure 3.14. Relative XRD peak intensities for the highest-intensity peak of a) PbI_2 and b) MAI plotted as a function of MAI precursor concentration. The relative peak intensity was determined by dividing the integrated intensity of the (001) PbI_2 peak (I_{PbI2}) by the sum of I_{PbI2} and the intensities of the $MAPbI_3$ (110) peak ($2\theta = 14.1°$). Areal peak intensities were calculated by applying a Pearson VII function using Jade software. Although error bars are included in the plot, they are not visible. Measures of uncertainty associated with the calculated peak intensities are listed in **Table D1** in **Appendix D**.

3.6.3. Device Performance Using Sequential Spin-Coating

Perovskite solar cell devices were fabricated to determine the optimal MAI precursor solution concentration for the sequential spin-coating method. All other components in the devices were fabricated following the same procedures used for the devices made via the dip method. Devices made with the higher loading of MAI (50 mg/mL) were more efficient as indicated by the *J-V* curves in **Figure 3.15**. These results are comparable to devices made using similar procedures, in which the reported *PCE*s of sample devices are 13.4 %[58,59] and 15.4 %.[53] Comparing the J-V results to the XRD patterns in **Figure 3.13**, the higher device performance in the devices fabricated with a more concentrated MAI solution is attributed to the more complete perovskite conversion.

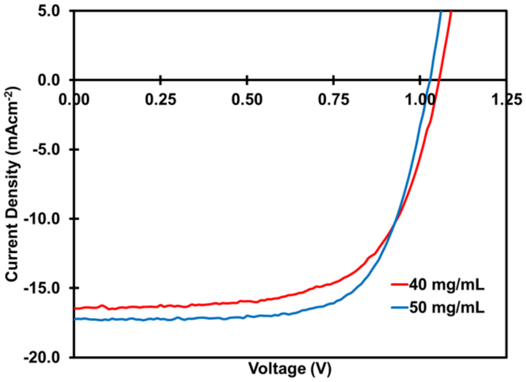

[MAI]		V_{oc} (V)	J_{sc} (mA cm^{-2})	*PCE* (%)	*FF*
40	Best Cell	1.07	16.45	11.22	0.64
	Average	1.04(0.04)	14.97(1.77)	9.33(1.90)	0.59(0.04)
50	Best Cell	1.03	17.24	12.28	0.69
	Average	1.04(0.02)	17.21(0.24)	12.40(0.28)	0.69(0.03)

Figure 3.15. *J-V* curves for the best-performing PSC devices fabricated via the SSC method using an MAI concentration of 40 mg/mL (red curve) and 50 mg/mL (blue curve). Performance metrics for the best-performing device and the average of five sample devices are given in the table to the right of the curves. The values in brackets are the standard deviations.

3.7. Conclusions

It has been demonstrated that simple adjustments in processing parameters can have large effects on the morphology of perovskite thin films during both dip-coating and spin-coating procedures. In particular, solution concentration and substrate temperature are key variables to monitor during the dip method. The dipping step in the SDC method was difficult to reproduce for two reasons. First, the conversion rate from PbI_2 to perovskite varied from batch-to-batch. Second, drying of the film with the air gun led non-uniformity across the substrates. These factors led to batch-to-batch inconsistencies and even variations in performance among the devices on the same substrate.

In contrast, the sequential spin-coating method allowed more control over conversion of the perovskite and morphology of the film, producing more consistent films and high-performing devices. Therefore, the spin-coating method was selected for use in subsequent device fabrications as the project moved forward to the next chapter: investigating new hole-transporting materials in PSCs.

It is important to consider the thermal properties of $CH_3NH_3PbI_3$ when investigating the two aforementioned methods of perovskite film formation. $CH_3NH_3PbI_3$ has two known phase transitions at temperatures of 162.7 K (~110 °C) and 326.6 K (~54 °C).[60,61] Since the perovskite made using the dip method is not heated during or after the conversion process, it remains in a single phase. In contrast, the perovskite is heated above its upper transition temperature (54 °C) following the sequential spin-coating procedure, resulting in a phase transition that marked by a significant crystal lattice volume expansion.[62] The work by Bi *et al.*[59] suggests that prolonged heating of a $CH_3NH_3PbI_3$ thin film above the upper transition temperature (e.g., at 100 °C) promotes the growth of larger crystallites. The result is a compact and continuous perovskite active layer with devices showing improved device *FF* and *PCE* compared to those that were heated for shorter durations. This work provides evidence for beneficial changes in morphology upon heating above the $CH_3NH_3PbI_3$ and may explain the superior performance of devices made via the sequential spin method over the dip method.

CHAPTER 4 – ORGANIC HOLE-TRANSPORTING MATERIALS FOR PEROVSKITE SOLAR CELLS

4.1. Background

Achieving a robust and reproducible method for the fabrication of efficient planar heterojunction solar cells was an important outcome of **Chapter 3**. Although high efficiency is among one of the top priorities in the development of PSCs, another important consideration is the cost. The goal for **Chapter 4** is to investigate cheaper alternatives for organic hole-transporting materials in perovskite solar cells.

Spiro-OMeTAD was the first solid-state organic hole-transporting material used in perovskite solar cells[17] and continues to be the industry-standard. However, spiro-OMeTAD is expensive due to the multifaceted synthesis of its starting materials.[63] It is therefore important to develop economical HTMs synthesized from low-cost starting materials to reduce the overall cost of PSCs.

Design of a new organic HTM requires the piecewise attachment of π-conjugated functional groups. Ideally, a cheap building block, such as triphenylamine (TPA), is at the centre or "core". The TPA core adopts a pseudotetrahedral three-dimensional (3D) geometry (see **Figure 4.1 a)**).[64] This structural motif has been proven to yield effective hole conductors for a variety of organic electronic applications.[65–69] Each of the three phenyl groups can be functionalized at *para* positions forming the three "side-arm" units. The result is a 3D propeller-shaped molecule. This design motif has proven to be successful for other TPA-based HTMs in PSCs, yielding high efficiencies (see **Figure 4.1**).[70,71]

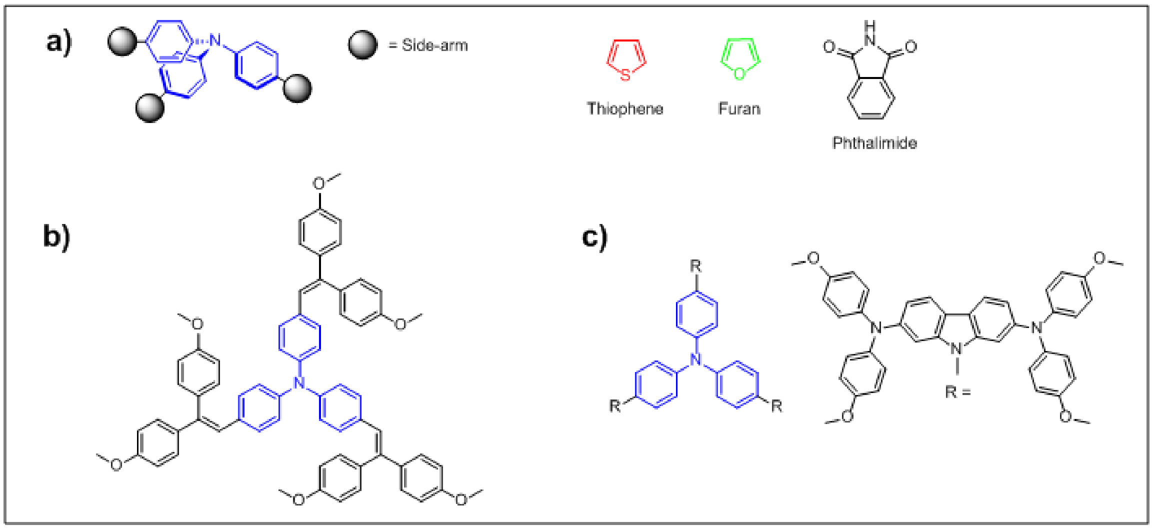

Figure 4.1. a) A structural representation of the design motif for HTMs with a TPA core. Two examples of propeller-shaped small-molecule HTMs used in PSCs ((b)[70] and (c)[71]) are also shown.

Using the motif depicted in **Figure 4.1 a)**, side-arms can be designed with different functionalities to build TPA-based derivatives with different electronic properties.[72] Three functional groups commonly used for organic π-conjugated materials are thiophene, furan and phthalimide (shown in **Figure 4.1**); these groups can be adopted in the side-arms. A discussion of the prevalence of thiophene as an electron-donating component in small-molecule (**Figure E1**) and polymer hole-transporting materials (**Figure E2**) in PSCs is provided in **Appendix E**.

Herein, a low-cost TPA core is used to build a series of hole-transporting materials, each with a different side-arm composition. The effect of both molecular composition and film-forming properties on the performance TPA-based HTMs in perovskite solar cells is investigated. By engineering side-arms with different functionalities (i.e., a different combination of electron-donating (donor) and electron-withdrawing (acceptor) units), it is possible to tune the electronic properties. Therefore, the HOMO can be adjusted to a suitable level conducive to hole-extraction from the perovskite active layer.

4.2. Materials and Methods

4.2.1. Materials

The molecular structures of all organic materials used in this study are given in **Figure 4.2**. The molecular formula and molecular weight for each of the materials are provided in **Table 4.1**. The first hole-transporting material is 5,5',5''-(5,5',5''-(nitrilotris(benzene-4,1-diyl))tris(2-hexylthiophene), designated as "HTM01". HTM01 is the simplest and smallest molecule in the series with a TPA core flanked by a thiophene unit for the purpose of extending π-conjugation. The hexyl chains increase solubility in organic solvents. This compound has been previously synthesized by others via lithiation and transmetallation.[73] In Welch lab, Arthur Hendsbee successfully synthesized HTM01 via direct arylation as an alternative and facile procedure.

The second compound in this study is 5,5',5''-(5,5',5''-(nitrilotris(benzene-4,1-diyl))tris(furan-5,2-diyl))tris(2-octylisoindoline-1,3-dione), or "HTM02". HTM02 (also synthesized by Arthur Hendsbee) has two structural differences compared to HTM01: i) replacement of the thiophene unit with a furan group and ii) addition of an electron-deficient phthalimide acceptor group. The furyl units were selected for two reasons. First, it is considered to be a sustainable and "green" alternative to thiophene as a building block in functional materials since it is derived from biological feedstocks.[74–76] Second, substitution of furan for thiophene as donor units in organic semiconductors can result in an increase in hole mobility, as demonstrated by recent work in the Welch and Hill labs[77] and by others.[78,79] The phthalimide groups are electron-deficient and stabilize the frontier energy levels of the molecule HTM02 relative to HTM01, resulting in a decrease in the LUMO energy and a corresponding decrease in the bandgap energy.

The third compound is named HTM03. HTM03 is largest, most complex molecule. Similar to HTM02, HTM03 has furan-phthalimide D-A units. A diketopyrrollopyrrole (DPP) unit in the center of the side-arm was inserted to stabilize the frontier energy levels, particularly the LUMO, to reduce the bandgap energy relative to HTM02. Large branched alkyl chains (i.e., 2-ethylhexyl) help to disrupt strong π-π intermolecular interactions between DPP units,[80] which improves solubility. 1-ethylpropyl or "swallowtail" end caps were used in place of the hexyl chains present in HTM01 and HTM02.

The fourth hole-transporting material is 7,7'-(4,4-bis(2-ethylhexyl)-4H-silolo[3,2-b:4,5-b']dithiophene-2,6-diyl)bis(6-fluoro-4-(5'-hexyl-[2,2'-bithiophen]-5-yl)benzo[*c*]-[1,2,5]thiadiazole), which is also known as *p*-DTS(FBTTh$_2$)$_2$, but is labelled as "HTM04" throughout this chapter. This material demonstrates high hole-mobility[81] and has similar HOMO energy levels as HTM01, HTM02 and HTM03. For this reason, it is appropriate for use as a hole-transporting material in this study. HTM04 is also well-known as a high-performance two-dimensional (2D) donor material in small-molecule organic solar cells.[82]

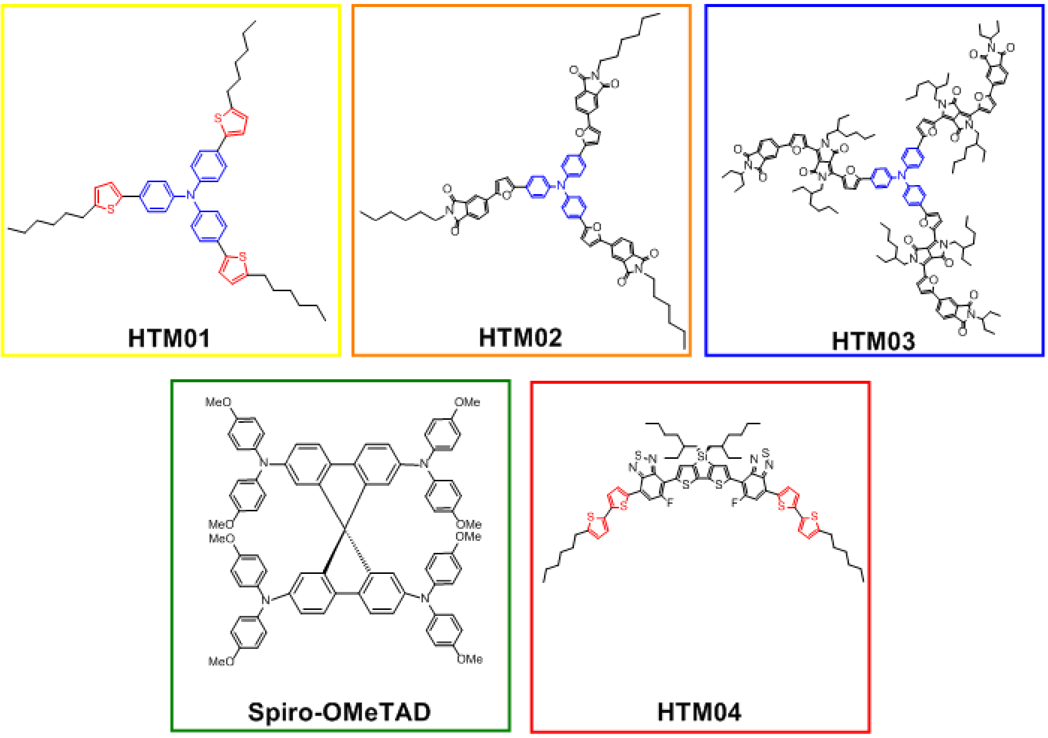

Figure 4.2. Molecular structures of the five HTMs investigated in this study. The TPA cores are coloured blue and thiophene units are coloured red.

Table 4.1. The chemical formula and molecular weight of each HTM used in the study.

HTM	Chemical Formula	Molecular Weight (g/mol)
HTM01	$C_{48}H_{57}NS_3$	744.17
HTM02	$C_{72}H_{66}N_4O_9$	1131.34
HTM03	$C_{147}H_{168}N_{10}O_{18}$	2263.01
HTM04	$C_{64}H_{72}F_2N_4S_8Si$	1219.87
Spiro-OMeTAD	$C_{81}H_{68}N_4O_8$	1225.45

4.2.2. Thin-film Formation via Spin Coating

To characterize each hole-transporting material individually, thin-films were spin-cast on glass substrates. Precursor solutions were prepared by combining the weighed solid compound and the measured volume of solvent (chlorobenzene) in a 4.0 mL Teflon-capped vial with a stir bar. The materials were weighed using an analytical balance and the solvent was measured using a 1000-µL micropipette. Solutions of spiro-OMeTAD, HTM01 and

HTM02 were stirred overnight at RT and solutions of HTM03 and HTM04 were stirred on a hotplate set to 90 °C.

The 25 mm × 25 mm glass substrates were cut from microscope slides. The substrates were cleaned prior to use by scrubbing the surface with a mixture of lab detergent (Sparkleen®) and DI H_2O and then rinsing thoroughly with DI H_2O. The substrates were then sequentially rinsed with acetone and ethanol prior to UV/ozone cleaning for 20 min.

Substrates were loaded onto the chuck of a Laurell spin-coater immediately after UV/ozone treatment. The solutions of spiro-OMeTAD, HTM01 and HTM02 were cast at RT whereas the solutions of HTM03 and HTM04 were hot-cast due to their lower solubility. Each solution was retracted from the vial using a 1 mL syringe. Approximately 200 µL of solution was then dispensed onto the center of the substrate through a 0.45 µm PTFE filter in one aliquot. The spin-coat program was then run using the parameters specified in **Table 4.2**. The high solubility of spiro-OMeTAD in organic chlorinated solvents permits casting from a solution that is higher in concentration than the TPA HTMs and HTM04.

Table 4.2. HTM deposition parameters.

HTM	Concentration in CB (mg/mL)	Solution Deposition Temperature (°C)	Spin Speed (rpm)	Spin Duration (s)
Spiro-OMeTAD	80	25	4000	30
HTM01	25	25	1000	90
HTM02	25	25	1000	90
HTM03	25	70	1000	90
HTM04	25	70	1000	90

4.2.3. PSC Fabrication Procedure

All devices were made with the same architecture: FTO/TiO_2 compact/$CH_3NH_3PbI_3$/HTM/MoO_3/Ag. The FTO glass substrates and TiO_2 layers were prepared as described in **Chapter 3**. The perovskite active layers were formed via the optimal sequential spin-coating method also described in **Chapter 3**.

After the active layers were converted to perovskite, the devices were removed from the glovebox. All HTMs were deposited onto the perovskite layer in air via spin-coating from chlorobenzene solutions and filtered through 0.45 μm PTFE filters. No dopants were used in the devices comparing the different hole-transporting materials. However, a detailed discussion of the effect of dopants on HTM performance can be found in **Appendix F** with a comparison of *JV* curves for devices made with doped and undoped spiro-OMeTAD in **Figure F1**. Deposition parameters for each HTM are given in **Table 4.2**. The top metal contact was deposited by thermal evaporation at $< 4.0\times10^{-6}$ torr in a custom-built bell-jar evaporation system. A 10-nm layer of molybdenum (VI) oxide (MoO_3) was first deposited followed by 75 nm of Ag. The purpose of using a MoO_3-Ag top contact was to replace the commonly-used Au contact and reduce the overall cost of the system.[83] The final active area of each device was 0.032 cm^2.

After fabrication, the devices were promptly transferred into an Ar-filled glovebox, which was the location for *J-V* testing and the site of post-testing storage. To account for hysteresis in the *J-V* curves, each cell was scanned first from a forward bias (+ 2.0 V) to short-circuit (0.0 V) and then in the opposite direction. Each scan was repeated with three different scan delays (5 ms, 10 ms and 100 ms) at a sampling rate of 0.01 V/step.

4.3. Results and Discussion

4.3.1. Material Characterization

Figure 4.3 shows an energy level diagram of the components of the PSC devices. HOMO and LUMO energy levels of the organic hole-transporting materials were determined by cyclic voltammetry (CV plots shown in **Figure 4.4**). The onset of oxidation for each of the HTMs was measured as the intersection of the baseline of the CV plot and the line tangent to the first oxidation peak. These potential values were referenced to the oxidation potential of ferrocene, which has been measured previously to be 4.80 eV, and are listed in **Table 4.3**.[39] Detailed methods for the CV experiments and calculations of the energy levels can be found in **Section 2.7**. It was confirmed that the HOMO levels of all five HTMs were similar (~5 eV) and at an appropriate level for hole-extraction at the perovskite interface.

Energy levels of the other components are included in the diagram for comparison and are based on literature reports. The valence band maximum and the conduction band minimum of the perovskite ($CH_3NH_3PbI_3$) were previously determined by others.[17] The conduction band minimum of −5.5 eV for an air-exposed film of MoO_3 is representative of n-type MoO_3 charge-transport layers used in organic electronic devices.[84] In perovskite solar cells, MoO_3 is used as an n-type material to assist charge transfer from the HTMs to Ag, a high work-function electrode. Dense TiO_2 acts as the electron-transport/hole-blocking layer with a work function of −4.0 eV.[85] The work function of fluorine-doped tin-oxide (FTO), the electron-collecting electrode, is −4.5 eV based on measurements conducted using X-ray photoelectron spectroscopy (XPS).[86]

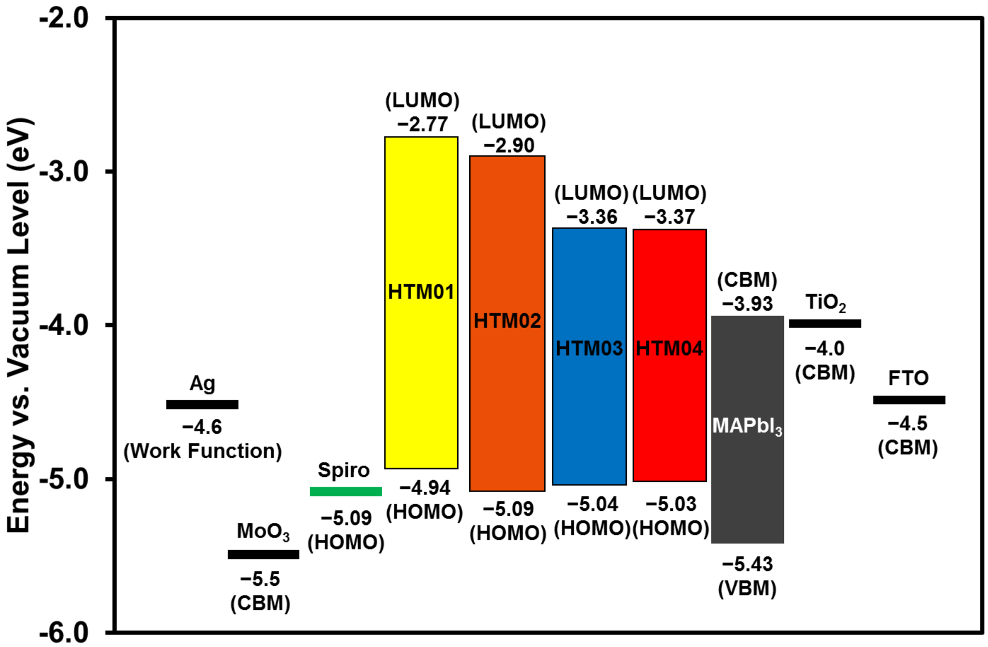

Figure 4.3. Energy level diagram for all components in the PSCs. The HOMO and LUMO levels for HTM01-04 were determined by CV, with coloured bars representing the bandgap. Only the HOMO level was measured for spiro-OMeTAD. The CBM and VBM for $CH_3NH_3PbI_3$ were determined by others.[7]

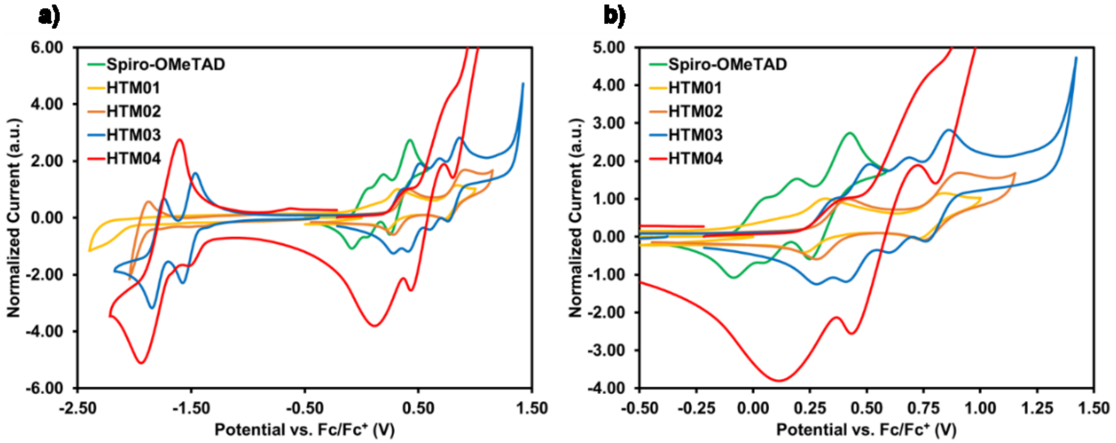

Figure 4.4. a) Full cyclic voltammograms (CVs) for each of the HTMs used in the study. b) A zoomed plot of the CVs for the HTMs, depicting the onset of oxidation for each of the five HTMs. All CVs were acquired by scanning at a rate of 100 mV/s. The values of the HOMO and LUMO levels were calculated by comparing the onset of oxidation and reduction (respectively) to the normal hydrogen electrode (NHE), assuming that the HOMO of Fc/Fc$^+$ is equal to 4.80 eV.[12] CVs for HTM01, HTM03 and HTM04 were acquired by Arthur Hendsbee, Jetsuda Areephong and Seth McAfee, respectively.

UV-Vis absorption spectra for the five HTMs are shown in **Figure 4.5**, with a summary of electronic parameters given in **Table 4.3**. Optical bandgap energies (E_g) acquired from both solution and thin-film spectra are defined by the onset of absorption (λ_{onset}), which was measured to be the wavelength at which the line tangent to the lowest-energy peak and the baseline intersect. In all of the HTMs, the onset of absorption wavelength for the thin-film spectra is longer (i.e., red-shifted) relative to that of the solution spectra ($\lambda_{onset,solution}$). This change is attributed to solid-state ordering within the thin films, which is known to enhance electron delocalization through the π-conjugated backbone of organic small-molecule semiconductors.[87] Spiro-OMeTAD and HTM01 have similar absorption profiles with maximum film absorption (373 and 377 nm, respectively) in the near-UV region. HTM02 has an intermediate optical bandgap, with maximum absorption at 445 nm for the thin film. HTM03 and HTM04 have the smallest E_g with onset of absorption at 715 and 759 nm, respectively (for thin films). The narrow bandgap and corresponding low-energy absorption of HTM03 is attributed to the additional DPP unit in the side-arm.

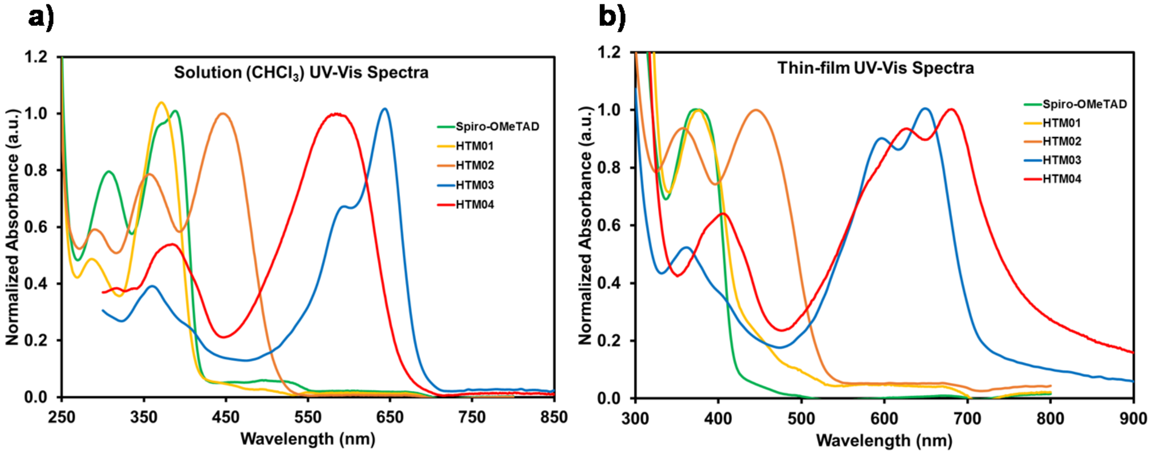

Figure 4.5. UV-Vis absorption spectra of HTMs acquired for a) solution samples with $CHCl_3$ as the solvent and b) thin-films on glass substrates.

Table 4.3. Summary of optical and electronic parameters of HTMs.

HTM	E_{ox} vs. Fc (V)	E_{HOMO} (eV)	$E_{g,solution}$ (eV)	$E_{g,film}$ (eV)	$\lambda_{onset,solution}$ (nm)	$\lambda_{onset,film}$ (nm)
Spiro-OMeTAD	0.55	−5.09	2.98	2.96	416	419
HTM01	0.14	−4.94	3.02	2.95	411	420
HTM02	0.26	−5.09	2.43	2.38	510	520
HTM03	0.24	−5.04	1.81	1.73	685	715
HTM04	0.23	−5.03	1.86	1.63	665	759

4.3.2. Perovskite Solar Cell Fabrication and Testing

All devices fabricated without an HTL displayed evidence of shorts and produced no photocurrent, suggesting that the perovskite layer itself has pinholes – a source of shunt pathways. On the other hand, all devices with HTLs displayed diode-like *J*-*V* curves with no evidence of shorts (see **Figure 4.6**). A summary of the device performance metrics for the best and average cells is provided in **Table 4.4**. Furthermore, it may be filling-in deep pinholes in the rough perovskite active layer and may be blocking shunt pathways.

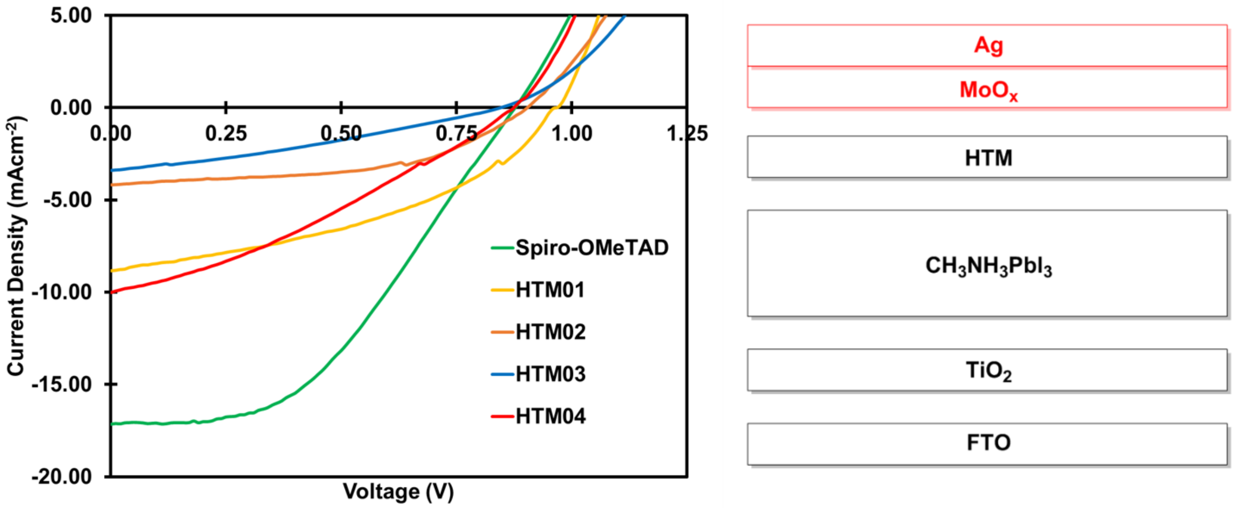

Figure 4.6. *J*-*V* curves of the best-performing cells with different HTLs. Also shown is an illustration of the configuration of the planar PSCs.

Table 4.4. A summary of performance metrics for the best cells (i.e., those with the highest *PCE*) with different HTLs. The plots were obtained by scanning from +2.0 V to 0.0 V at a rate of 10 ms per data point under an illumination of 1.5 G. The average metrics for five sample devices (each with a different HTL) are also provided with standard deviations in the brackets. The shunt and series resistances listed are for the best-performing devices only.

HTL		**V_{oc} (V)**	**J_{sc} (mA cm^{-2})**	***PCE* (%)**	**FF**	**Shunt Resistance (Ω/cm^2)**	**Series Resistance (Ω/cm^2)**
Spiro-OMeTAD	Best	0.88	17.16	6.58	0.43	1.65×10^6	0.04
	Average	0.85(0.04)	16.36(1.28)	5.57(0.67)	0.40(0.03)	-	-
HTM01	Best	0.97	8.84	3.51	0.41	2.49×10^2	0.04
	Average	0.94(0.03)	7.96(0.62)	2.83(0.43)	0.38(0.02)	-	-
HTM02	Best	0.92	4.18	1.99	0.52	5.68×10^2	19.98
	Average	0.88(0.08)	3.91(1.04)	1.61(0.43)	0.48(0.13)	-	-
HTM03	Best	0.85	3.40	0.89	0.31	3.44×10^5	8.47
	Average	0.87(0.04)	3.34(0.36)	0.88(0.06)	0.30(0.01)	-	-
HTM04	Best	0.89	10.02	2.76	0.31	1.74×10^5	0.02
	Average	0.80(0.08)	7.47(3.04)	1.79(0.94)	0.28(0.03)	-	-

HTM01 performed the best among the TPA hole-transporting materials and displayed the highest J_{sc} and *PCE*. Since the V_{oc} of all devices is similar, J_{sc} is the major contributing parameter to the observed differences in *PCE* and overall performance. Interestingly, the two HTMs with thiophene units (i.e., HTM01 and HTM04) displayed the highest J_{sc} compared to the two HTMs with the furan-phthalimide units. This may suggest that the thiophene unit plays a role in the hole-extraction from the perovskite or hole-transport to the metal contact. Compared to spiro-OMeTAD, all four new HTMs resulted in devices with lower photocurrents, corresponding to lower overall performance.

4.3.3. Hole-Transporting Layer Surface Morphology

Figure 4.7 shows AFM images of the hole-transporting layer surfaces acquired after device fabrication and testing. An image of the bare perovskite layer is shown for comparison. The bare perovskite film consists of micron-sized crystalline grains with large height deviations that resemble "mountains" and "valleys". Ideally, the HTM would conform to the rough surface of the perovskite and provide uniform coverage across the entire active layer. Such morphology would result in devices of consistent HTL thickness, and therefore, consistent PV performance. It is more likely, however, that the HTM will tend to planarize the films, partially filling in the low "valleys" while resulting in thinner coverage on the "mountains". Herein, AFM was used to assess the morphology of each HTL in terms of grain size and overall surface roughness.

It is observed that Spiro-OMeTAD forms the smoothest, most planar film over the underlying perovskite layer with the lowest value of root-mean square roughness (R_{RMS}) (see **Table 4.5**). The spiro-OMeTAD solution was also significantly more concentrated than the others. This may explain how spiro-OMeTAD effectively fills-in gaps between the large perovskite domains and forms a planar surface over the perovskite crystals. From the roughness parameters listed in **Table 4.5**, the roughness of the HTL appears to decrease from HTM01 to HTM02 to HTM03. Although error bars on the roughness parameters are not provided, the uncertainty in the values is quite high; the area that was sampled (one or two 5×5 μm scans per sample) is very small relative to the entire HTL surface.

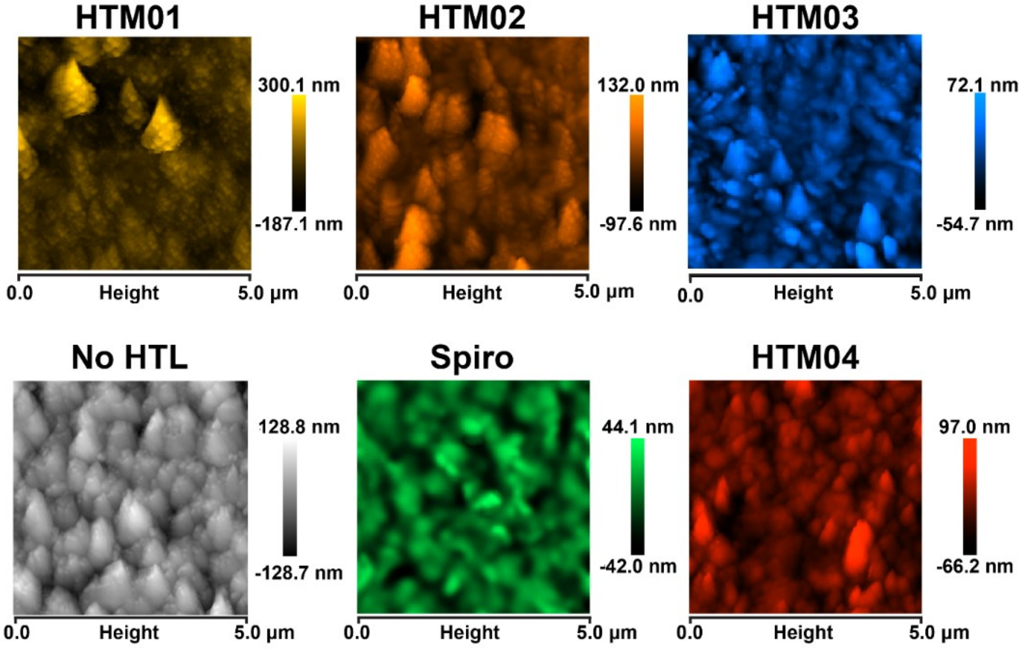

Figure 4.7. 2D AFM images of HTL surfaces of the five hole-transporting materials under study. An image of a neat perovskite film (i.e., no HTL) is shown for comparison.

Table 4.5. Roughness parameters of HTL films on perovskite films obtained from 2D AFM images. The parameters were calculated over an area of 25 µm^2.

	No HTL (Neat perovskite)	**Spiro-OMeTAD**	**HTM01**	**HTM02**	**HTM03**	**HTM04**
Surface Area (µm^2)	26	24	28	24	25	24
R_{RMS} [a] (nm)	35	12	58	28	17	20
R_{a} [b] (nm)	28	10	40	21	13	14
$R_{\max}$ [c] (nm)	246	86	445	228	132	170

[a] R_{RMS}, the root mean square (RMS) average of height deviations relative to the mean image data plane. [b] R_{a}, the average of the absolute values of the surface height deviations relative to the mean plane. [c] $R_{\max}$, the vertical distance between the highest and lowest data points in the image.

4.4. Conclusions

A design strategy for organic hole-transporting materials has been demonstrated with applications in PSCs using a TPA-core and highly modular side-arms. By keeping the HOMO level constant among the HTMs, the effects of shape, size, and conjugation length on thin-film morphology and device performance could be compared. Following this approach, the molecular structures of the HTMs could be easily modified, such as the exchange of electron-rich (e.g., thiophene and furan) side-arm functionalities. As a result, electronic properties such as the HOMO level can be tuned to an appropriate value for hole extraction from the perovskite. Furthermore, a trend was observed in the performance of the TPA-based hole-transporting materials and the type of functionalities used in the side-arms: devices with the HTM including a thiophene unit (HTM01) in the side-arm produced higher photocurrent than those with HTMs containing the furan-phthalimide unit (HTM02 and HTM03). The bandgap energy of the HTM does not appear to have a significant influence on PV performance since HTM02 and HTM03 display similar performance, yet HTM03 has a significantly smaller bandgap. Comparison of the TPA-based donors to HTM04 confirmed that another thiophene-containing molecule (albeit, linear in shape) generated greater photocurrent than those with furan-phthalimide. Furthermore, HTM04 has a significantly narrower bandgap than HTM01 yet displays a similar J_{sc} in PSC devices.

It was shown that the surface roughness of the hole-transporting layer formed by HTM01, HTM02, HTM03 and HTM04 was not significantly different and therefore was not a major factor in the observed differences in PV performance. However, it was observed that spiro-OMeTAD forms a smoother layer than the other four HTMs, which may be attributed to the high solution concentration. The high solubility of spiro-OMeTAD gives it the ability to better planarize the rough perovskite film and contributes to the high *PCE*.

Development of simple TPA-based hole-transporting materials via facile synthetic methods is commercially relevant. Having identified a unique structure-performance relationship, further investigation of the effect of heterocycles in the sidearm units of such HTMs may proceed. Future optimization in the molecular design of TPA-based HTMs could focus on adjustments to the side-arm units including:

i. The use of sulfur-based heterocyclic functionalities;

ii. Exchanging R-groups (e.g., methoxy) to enhance solubility, affording the preparation of solutions with higher concentrations, which would lead to thicker HTL film-formation and better coverage of the perovskite surface.

4.5. Future Work

Two other important factors to consider in the development of alternative HTMs are air and thermal stability. In order to be viable as a commercial material, the HTM must be able to operate in humid and at elevated temperatures. For this reason, it is proposed that the following comparative experiments be conducted for the series of HTMs:

i. Thermogravimetric analysis (TGA) to monitor physical changes to the materials under heat exposure;

ii. Photovoltaic performance (e.g., *J-V*) measurements under controlled atmospheric conditions (e.g., elevated humidity levels).

From this study, it was discovered that the molecular structure of the side-arms of the TPA-based hole-transporting can influence performance in perovskite solar cells. Modifications to HTM01 and HTM02 can be made to further investigate the effect of thiophene, furan, phthalimide and combinations of the three. **Figure 4.8** depicts the molecular structures of two new HTMs. HTM01 is modified by replacing the thiophene unit with furan, whereas the furan unit in HTM02 is replaced by thiophene while keeping the phthalimide group present. It is proposed that by fabricating devices with four different hole-transporting materials under the same, controlled processing conditions, insight into the relationship of hole-transport in perovskite solar cells and the functional groups in the HTM can be gathered. This methodology is advantageous with modular designs such as

HTM01 and HTM02 since new derivatives can be readily synthesized and screened for device performance.

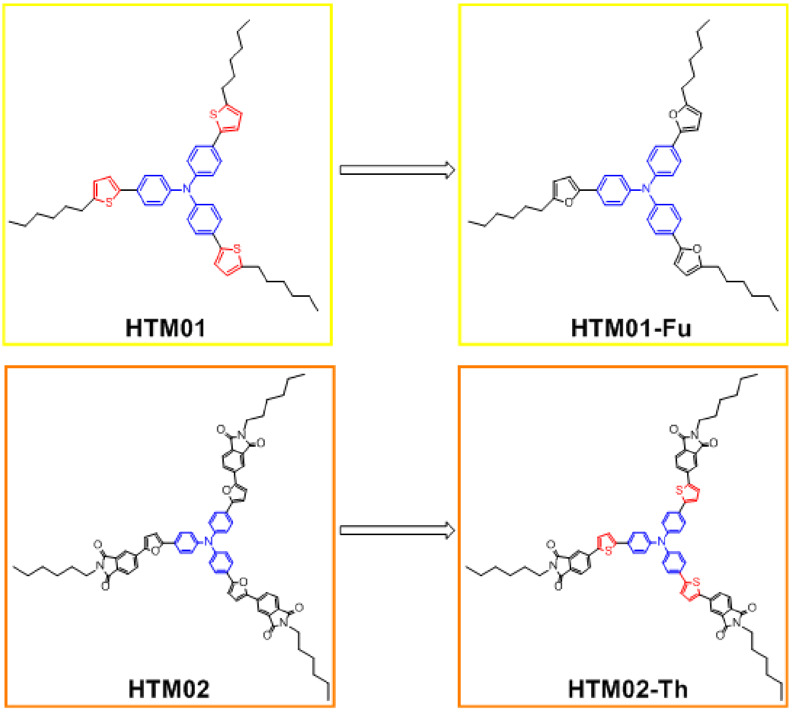

Figure 4.8. Proposed modifications to HTM01 and HTM02 for future studies in TPA-based HTMs.

In a separate study discussed in **Appendix G**, non-conjugated polymers were investigated as inert additives in hole-transporting layers of perovskite solar cells. It was shown that addition of non-conjugated polymers can increase the performance of devices (**Figure G1** for *J-V* curves) by improving the planarity of the hole-transporting layer formed by HTM04 (see **Figure G2** for AFM images). This strategy is a proposed as a viable technique to enhance device performance in perovskite solar cells and can be applied to new TPA-based hole-transporting materials as well.

CHAPTER 5 – STAR-SHAPED DONOR MATERIALS FOR SMALL-MOLECULE ORGANIC SOLAR CELLS

5.1. Background

5.1.1. Transition from Hole-transporting Materials to Donors

It was shown in **Chapter 4** that the molecular composition and film-forming properties of the TPA-based hole-transporting materials can influence device performance in PSCs. Ultimately, the select TPA-based compounds were not ideal candidates for HTMs – all three displayed significantly lower performance than spiro-OMeTAD in perovskite solar cells. However, these materials might be better suited for other photovoltaic applications.

The three newly designed small molecules used as HTMs in PSCs all have appropriate energy levels and absorption profiles to be considered for use as donor components in organic solar cells. In some instances, such compounds can serve in both PSC and OSC devices. For example, in a recent paper by Cheng *et al.* a single organic compound was used for the dual-purpose as a hole-transporting material in a perovskite solar cell and as a donor in a bulk heterojunction organic solar cell.[88] Similarly, HTM04 (aka *p*-DTS(FBTTh$_2$)$_2$) is a high-performance donor material in OSCs,[82,89] but it was shown in **Chapter 4** to also function as an HTM in PSCs.

5.1.2. Selection of a Complementary Acceptor

It is of interest to develop fullerene-free organic solar cells. In small-molecule organic photovoltaic systems, fullerene derivatives, such as phenyl-C$_{61}$-butyric acid methyl ester (PC$_{61}$BM or PCBM), are the gold-standard electron-acceptors. However, fullerenes are expensive, difficult to synthesize and display weak absorption of visible light;[90,91] factors that are disadvantageous in OSCs. The goal herein is to investigate the new TPA small molecules as donors with custom-built non-fullerene acceptors.

Fullerenes, such as PCBM, have a spherical three-dimensional (3D) shape and a 3D π-conjugated pathway (see **Figure 5.1**). As result, charge transport in fullerenes is isotropic;[92] charge carriers are transported in all directions through the fullerene. The success of fullerenes as acceptors in organic solar cells is largely attributed to its shape, which allows for high electron mobility in three dimensions.[93] In fact, the high-dimensionality and 3D shape is a sought-after trait for the design of non-fullerene acceptors (see **Figure H1** in **Appendix H** for examples of 3D non-fullerene acceptors).

In contrast, planar organic molecules are two-dimensional (2D) in shape, yet have a π-conjugated pathway that runs in one plane (i.e., a 1D π-conjugated pathway along the length of the molecule),[92] A well-known example of an organic molecule with a 2D shape is HTM04, aka “*p*-DTS(FBTTh$_2$)$_2$” (**Figure 5.1**).[82]

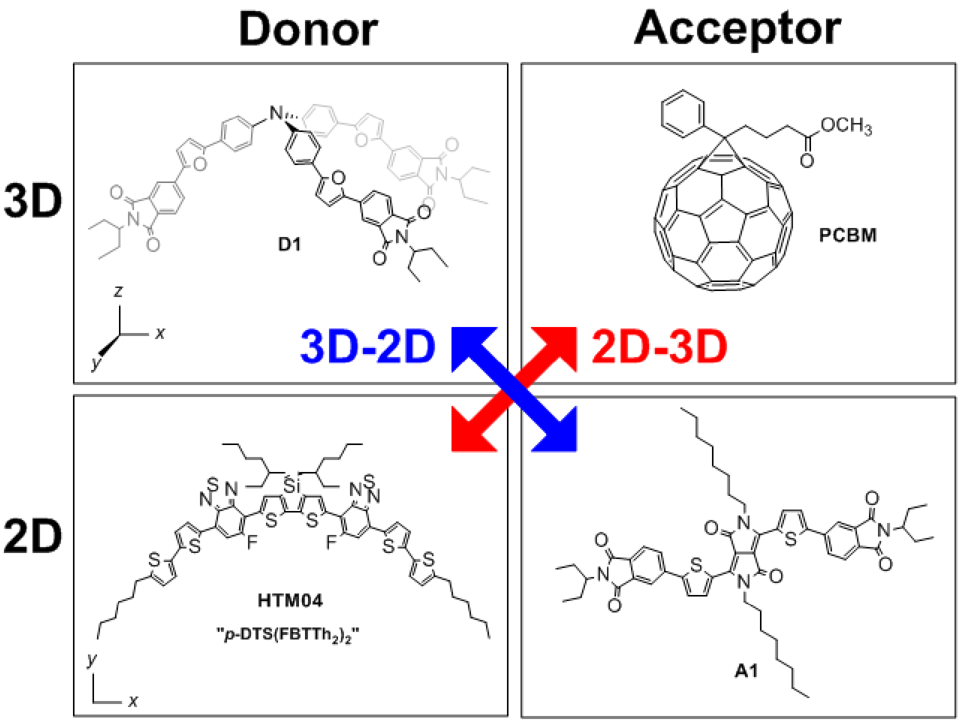

Figure 5.1. An illustration of the concept of opposing molecular geometry in donor-acceptor BHJ OPVs.

Some of the best-performing small-molecule OSCs consist of a 3D fullerene acceptor with a planar 2D donor.[94] For clarity, these types of systems will be referred to as "2D-3D" systems herein (indicated by a red arrow in **Figure 5.1**). The dissimilarity in shape between the two complementary materials is thought to drive self-assembly and produce a solid-state morphology in bulk heterojunction active layer that is conducive to efficient charge transfer, separation and extraction. These pathways are essential for charge transportation and collection at the electrodes. Similar to PCBM, TPA-based compounds also demonstrate high dimensionality and assume a 3D shape. Evidence for the sp^3-hybridization of the N-atom at the TPA core in other related organic semiconductors has been demonstrated by others using density functional theory (DFT) calculations[64] and is suggested to be the result of steric interactions between the side-arm units.[92] As a result, the molecule assumes a 3D propeller-shape with π-conjugated pathways extending in three dimensions. To date, all TPA donor materials reported in the literature for use in OSCs are accompanied with a fullerene acceptor (e.g., C_{60}, $PC_{61}BM$, $PC_{71}BM$, etc.), While there have been some examples in the literature of 3D TPA donors in OSCs achieving modest *PCE*s between 3%[95–97] and 4%,[98] the issue of the use of fullerene acceptors remains unaddressed.

5.1.3. Custom-Made D-A Pairs

Developing fullerene-free OSCs requires a D-A pair with the following criteria:

i) Distinct geometry/topology to ensure phase separation, allowing for the formation of homogeneous percolation pathways within the active layer and charge transport to the electrodes,

ii) Complementary light absorption to maximize photon-harvesting,

iii) HOMO/LUMO energy levels that are offset to ensure efficient electron transfer (LUMO of donor to LUMO of acceptor and HOMO of donor to HOMO of acceptor),

iv) Thermal and air stability,

v) Low cost with a low embodied energy,

vi) Photo-stability.

The goal herein is to utilize the TPA-based hole-transporting materials developed in the previous chapter as donor molecules in fullerene-free organic solar cells. It is now reported how the molecular structure of such compounds will affect the electronic, structural and morphological properties in thin-film D-A systems. In this case, 3D trigonal pyramidal conjugated molecules, such as those with a TPA core, are ideally paired with a planar 2D acceptor to form a “3D-2D” system and satisfy the first criterion (indicated by the blue arrow in **Figure 5.1**). Although the geometries of these compounds are agreeable, the absorption, electronic properties and thin-film morphology must be characterized to ensure that the other criteria are met.

5.2. Materials and Methods

5.2.1. Materials

Molecules D1, D2 and A1 were synthesized in the Welch lab by Arthur Hendsbee. The structures of the compounds are depicted in **Figure 5.2**. The 3D, TPA-based donor compounds are named “D1” and “D2” for simplicity. The reader is reminded that “D2” is named “HTM02” in **Chapter 4**. D1 and D2 differ only in the terminal alkyl chains; D1 has bulky 1-ethylpropyl (aka “swallowtail”) groups while D2 has linear hexyl chains.

A linear, 2D acceptor with a DPP core was selected as the acceptor. This compound, which is named “A1” for the purpose of this chapter, has been previously reported to have favourable optoelectronic properties for electron transport.[99] A1 contains two bridging thiophene units that connect the DPP core to the electron-deficient phthalimide end-caps. The terminal and core alkyl groups are swallowtail and octyl chains, respectively. The design of this compound allows for the substitution of a variety of R-groups that can influence molecular interactions and self-assembly in the solid-state (vide infra).

In order to purify the organic compounds used in this work, standard organic purification techniques were applied by Arthur Hendsbee, including organic extractions, column chromatography, filtrations and recrystallizations. ^{1}H and ^{13}C nuclear magnetic resonance (NMR) spectroscopy and mass spectrometry were used to confirm the identity of the molecules as well as to detect organic impurities. In addition, elemental analysis was used to confirm the absence of impurities such as inorganic compounds (e.g., SiO_2, which is a potential contaminant during chromatography) that are not visible using other methods. The samples of each material used herein were qualitatively deemed to be pure when the analytical methods listed above detected no extraneous signals. It is recognized that this method of purity assessment is dependent on the detection limit of each instrument. Although each of the analyses provides a qualitative assessment of sample purity, quantitative measurements of purity were not conducted.

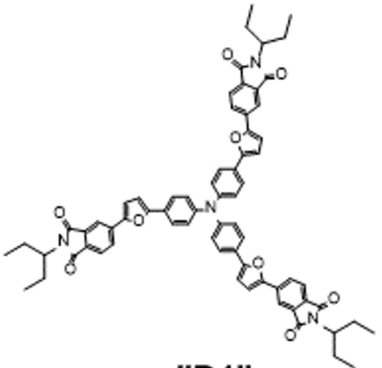

"D1"

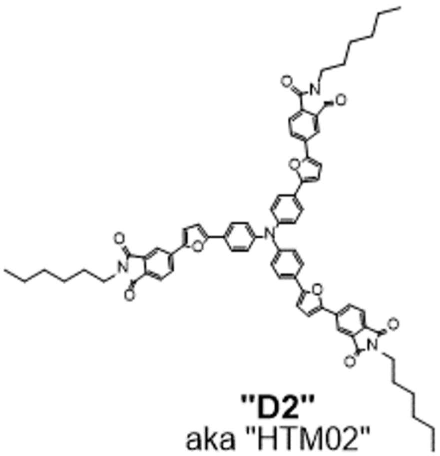

"D2"
aka "HTM02"

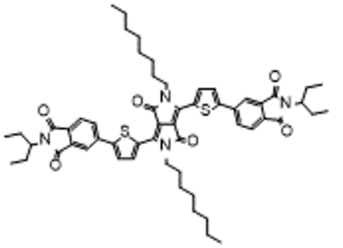

"A1"

	Chemical Formula	**Molecular Weight (g/mol)**
D1	$C_{69}H_{60}N_4O_9$	1089.26
D2	$C_{72}H_{66}N_4O_9$	1131.34
A1	$C_{56}H_{70}N_4O_6S_2$	959.32

Figure 5.2. Molecular structures of D1, D2 and A1.

5.2.2. Thin-film Formation via Spin Coating

All thin-films were formed via spin-coating from solution. Unless otherwise stated, single-component thin-films were spun from solutions using $CHCl_3$ as the solvent with a concentration of 10 mg/mL. D1:A1 and D2:A1 blend-film solutions used $CHCl_3$ as the solvent with a total solid concentration of either 30 or 20 mg/mL (e.g., 10 mg of D1 and 10 mg of A1 per 1 mL for a 20 mg/mL blend solution). Neat solutions (i.e., no solvent additives) were prepared by combining the weighed (using an analytical balance) solid compound(s) and the measured volume (using a micropipette) of $CHCl_3$ in a 4.0 mL Teflon-capped vial with a stir bar. Solutions were gently heated for 10 min under stirring and then allowed to stir overnight at room-temperature to dissolve the materials.

The films were spin-cast using a spin speed of 1000 rpm for a duration of 90 s. A description of the spin-coating procedure for organic thin-films can be found in **Section 4.2.2**.

5.2.3. Organic Solar Cell Fabrication Procedure

OSC devices were fabricated on 25 mm × 25 mm pre-patterned ITO-coated glass substrates. Substrates were cleaned by gently scrubbing the surface with a solution of DI H_2O and Sparkleen® lab detergent using a soft toothbrush. The substrates were then sonicated vertically in a solution of DI H_2O and Sparkleen® for 15 min after which they were rinsed thoroughly with DI H_2O, dried under a stream of filtered air, and then sonicated vertically in acetone for 15 min. The process was then repeated, but using ethanol as the solvent. The substrates were then treated under a UV/ozone lamp for 20 min.

Immediately following UV/ozone exposure, a layer of PEDOT:PSS was deposited as the HTL from a chilled aqueous colloidal suspension purchased from Heraeus (Product: Clevios^{TM} AI 4083). The substrate was mounted onto the chuck of the spin-coater and approximately 0.3 mL of the dispersion was dispensed onto the surface through a 0.45 μm PVDF filter before spinning at 2000 rpm for 45 s. The film was removed at the edges of the substrate using a lint-free Texwipe® dampened with DI H_2O to expose the ITO contacts. The PEDOT:PSS film was then annealed on a hotplate with a surface temperature of 140 °C for 10 min. Annealing the PEDOT:PSS film at such temperature has been shown by others to increase its conductivity, resulting in better-performing devices.[100]

After cooling the substrates to room-temperature, the active layer was deposited by spin-coating the surface using blend solutions. The total solids concentration of the solutions was 20 mg/mL with a 1:1 weight ratio of donor to acceptor, using $CHCl_3$ as the solvent. For each active layer, 0.2 mL of solution was filtered directly onto the substrate through a 0.45 μm PTFE syringe filter followed by spinning at 1000 rpm for 90 s. The ITO contacts were then exposed by scraping away the blend film using a razor blade. Once all active layers were spun, the substrates were promptly cycled into the glovebox and mounted into a substrate holder with a metal shadow mask.

The top metal contact was deposited using an in-house designed thermal evaporator equipped with two evaporation sources. Calcium was loaded into an alumina crucible as the first source and aluminum pieces were secured to a tungsten filament as the second source. Once the substrates were transferred into the evaporation chamber, the system was pumped down to $<1\times10^{-6}$ torr. The metal cathode was formed by sequential thermal evaporation of 7.5 nm of Ca and 100 nm of Al. The chamber was allowed to cool for 30 min under vacuum before the substrates were transferred directly into the glovebox where they were promptly tested.

5.2.4. Organic Solar Cell Testing

Device testing was performed using a Keithley 236 Source-Measure Unit in an Ar-filled glovebox under 100 (±1) mW/cm^2 illumination (AM 1.5G). *J*-*V* measurements were collected for each of the 18 devices on each substrate by scanning first from 1.2 V to -0.2V, 1.2 V to -6.2 V and finally from 1.2 V to -0.2 V, at a rate of 0.05 V/step with a delay of 5 ms between steps.

5.3. Results and Discussion, Part I

5.3.1. Materials Characterization, Part I

The first step in the study was to select a suitable solvent for the preparation of thin-film precursor solutions. Ideally, solutions with high concentrations are preferred for spin-coating to ensure uniform coverage of the substrate and adequate film thickness (i.e., 100 nm). For this reason, it is favourable to use solvents in which the active materials are highly soluble. The approximate solubility of each of the three materials in three different solvents with varying polarity (in order of decreasing polarity: ethyl acetate, 2-methyl tetrahydrofuran, and chloroform ($CHCl_3$)) were determined by an undergraduate honours student, Liz Kitching. The solubilities were quantified from a calibration curve constructed using solution UV-Vis data. All three of the materials displayed the highest solubility in $CHCl_3$. For this reason, all subsequent solutions in this study were prepared using $CHCl_3$ as the solvent.

UV-Vis absorption spectra for the three materials are plotted in **Figure 5.3 a)**. The absorption profiles of D1 and D2 are almost identical. This can be explained by the structural similarity of the two materials; both contain the same light-absorbing π-conjugated backbone. The absorption of A1 extends to longer wavelengths than both of the donor materials and is reflective of its narrow bandgap. This can be explained by the presence of the DPP chromophore; electrons are localized in low-lying molecular orbitals at the DPP core,[101] and low-energy photons are sufficient to induce electronic transitions. By combining either D1 or D2 with A1, the materials absorb across a broad range of the visible-light spectrum, fulfilling the second criteria for a D-A pair: complementary light absorption.

The CV plots for the three materials are shown in **Figure 5.3**. As expected, D1 and D2 exhibit very similar CVs, owing to their similar molecular structures. The oxidation potentials of both donor compounds are well-defined by the sharp oxidation peaks, allowing accurate elucidation of the HOMO levels. The bandgap energies ($E_{g,CV}$) for each of the materials are listed in **Figure 5.3 d)** and were obtained by taking the difference between the calculated HOMO and LUMO energy levels. These values are in good agreement with the values of the bandgap ($E_{g,onset}$) that were measured from the UV-Vis onsets of absorption (λ_{onset}). A description of how $E_{g,onset}$ is calculated from λ_{onset} is provided in **Section 2.5**. A1 has a high oxidation potential, corresponding to a deep HOMO level. The energy offset between the LUMO levels of D1 and A1 and D2 and A1 are 0.53 eV and 0.48 eV, respectively. In order for charge separation to occur, the offset must be larger than the exciton binding energy. Comparison of the energy offsets to the binding energies of other organic small molecules,[30] suggests that the offsets may be sufficient for charge separation. Therefore, the third criterion for a D-A pair is fulfilled: appropriate energy level alignment.

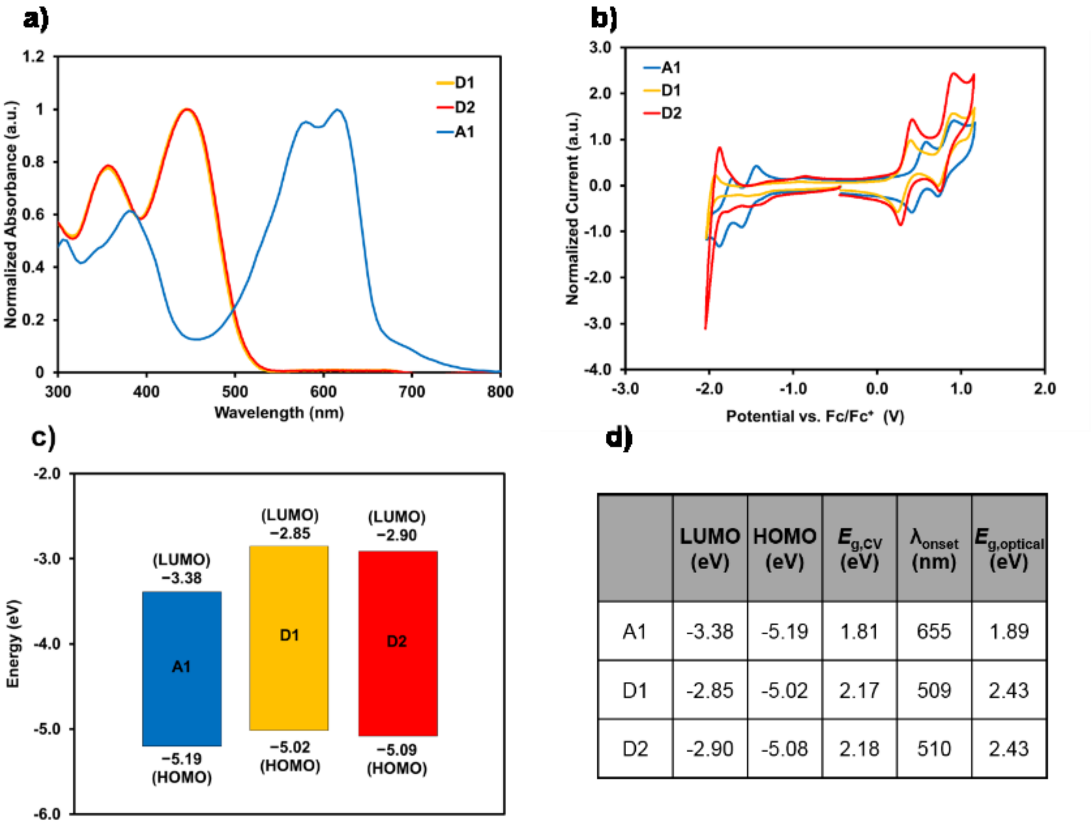

	LUMO (eV)	HOMO (eV)	$E_{g,CV}$ (eV)	λ_{onset} (nm)	$E_{g,optical}$ (eV)
A1	-3.38	-5.19	1.81	655	1.89
D1	-2.85	-5.02	2.17	509	2.43
D2	-2.90	-5.08	2.18	510	2.43

Figure 5.3. a) UV-Vis absorption spectra for solution samples of D1, D2 and A1 using $CHCl_3$ as the solvent. b) CV plots for D1, D2 and A1. c) An energy-level diagram for D1, D2 and A1, showing the HOMO and LUMO energy levels. d) A table summarizing the optoelectronic properties of the three materials, where $E_{g,CV}$ and $E_{g,optical}$ are the bandgap energies determined by CV and UV-Vis, respectively, and λ_{onset} is the wavelength at the onset of absorption, that is, the longest wavelength absorbed by the material.

5.3.2. Thin-film Characterization, Part I

The D1-A1 and D2-A1 systems meet the criteria for a suitable D-A pair and can be investigated in thin film systems. It is important to understand the properties of each material in independent systems before blend films are made. Neat films of D1, D2 and A1 were spin-cast on cleaned glass substrates for the purpose of solid-state thin-film characterization. Each film was thermally annealed at incrementally higher temperatures for a duration of 10 minutes in a procedure referred to as "sequential thermal annealing." Thermal annealing is a common processing technique applied to thin-films in OPV applications to induce morphological changes and dramatic increases in *PCE*.[102–104] Furthermore, it is important to understand how an organic material responds to heat in a thin film solar cell; under normal operation in full-sun exposure, the temperature of a solar cell will inevitably rise.

Figure 5.4 depicts UV-Vis absorption spectra for neat films of each of the three materials before and after sequential thermal annealing. The absorption spectra of D1 and D2 exhibit only slight changes upon thermal annealing; a slight blue-shift in the low-energy band of D1 and an overall decrease in the intensity of the absorption of both D1and D2 is observed with increasing annealing temperature. In contrast, A1 exhibits significant changes in the band structure after annealing, suggesting that electronic changes occur within the material. Most notably, three bands merge in the red-region of the spectrum (between 550 and 700 nm).

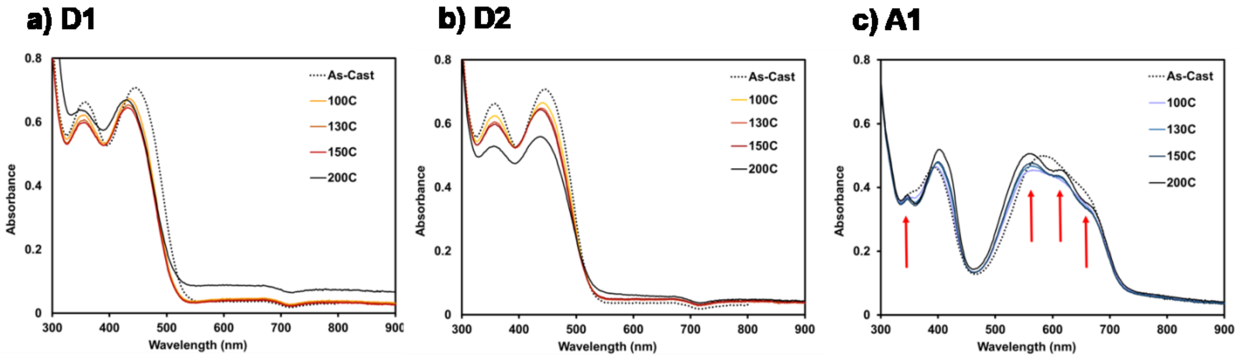

Figure 5.4. UV-Vis absorption spectra acquired by Liz Kitching for neat films of a) D1, b) D2 and c) A1 during the sequential thermal annealing experiment. The absorption spectrum was first acquired for each as-cast film. Each film was then annealed by placing the substrate onto a hotplate heated at 100 °C for 10 min after which a second absorption spectrum was acquired. This process was repeated, sequentially annealing at incrementally higher temperatures.

Thin-film blends of D1 and A1 and D2 and A1 were spin-cast on glass substrates by Liz Kitching. Similar to the one-component films, sequential thermal annealing was applied to the blend films and UV-Vis absorption spectra acquired after each annealing step. The absorption spectra of the blend films are depicted in **Figure 5.5**.

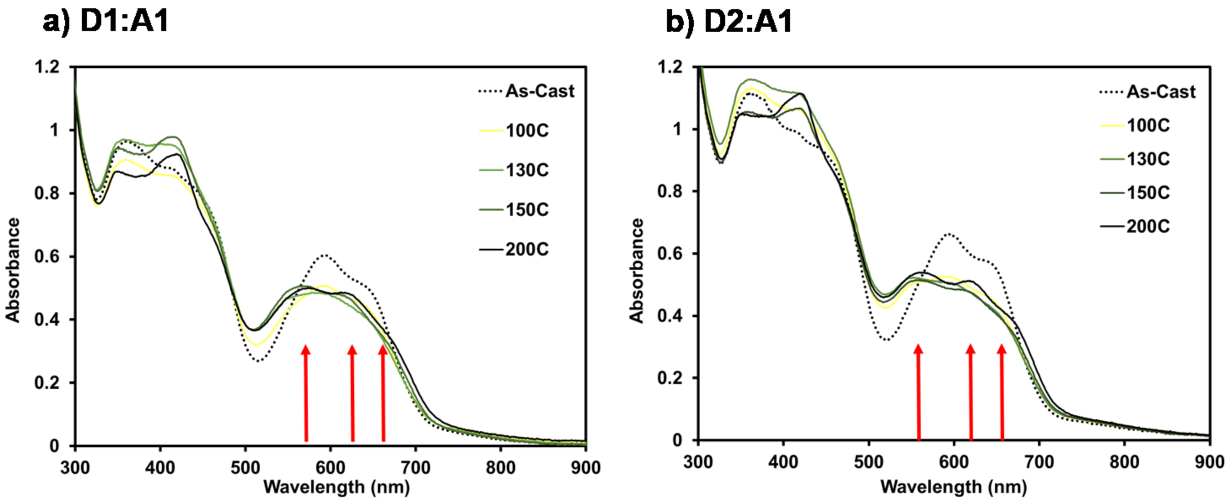

Figure 5.5. UV-Vis absorption spectra acquired for blend films of a) D1-A1 and b) D2-A1 during the sequential thermal annealing experiment. Solutions for both blends were prepared using the donor and acceptor compounds in 1-to-1 weight ratios.

The spectra of both unannealed (i.e., as-cast) blend films reveal two distinct bands in the region between 550 and 700 nm that are absent in the A1 as-cast neat film (see **Figure 5.3 c)**). The resolution of these bands suggests that the presence of the donor influences the solid-state ordering of A1 in the thin-film blend. Similar to the phenomenon observed in the neat film of A1, thermal annealing results in a change in the band structure of A1 within both blend films; three bands emerge upon annealing. From the UV-Vis spectra in **Figure 5.4**, it is clear that the absorption of the donor and acceptor is unbalanced in the blend films; the magnitude of absorption of D1 and D2 is considerably greater than that of A1. For this reason, blends with higher quantities of A1 relative to the donor were investigated. UV-Vis spectra (**Figure I1**) and XRD powder patterns (**Figure I2**) for films with varying ratios of donor and acceptor are provided in **Appendix I**.

The interactions between the donors and A1 within the blend films were further probed using photoluminescence (PL) spectroscopy (**Figure 5.6**). In this experiment, the thin film samples were irradiated with monochromatic light of a wavelength, λ_{ex}. A photodetector collected the emitted light across a range of wavelengths (λ_{em}), providing evidence for fluorescence. PL spectra of D1 and D2 neat films were first acquired using an excitation wavelength of 443 nm and collecting emitted radiation from 500 to 900 nm. The A1 neat film displayed minimal fluorescence when excited at the wavelength of maximum absorbance (i.e., 587 nm). For this reason, the PL spectrum of A1 is not shown.

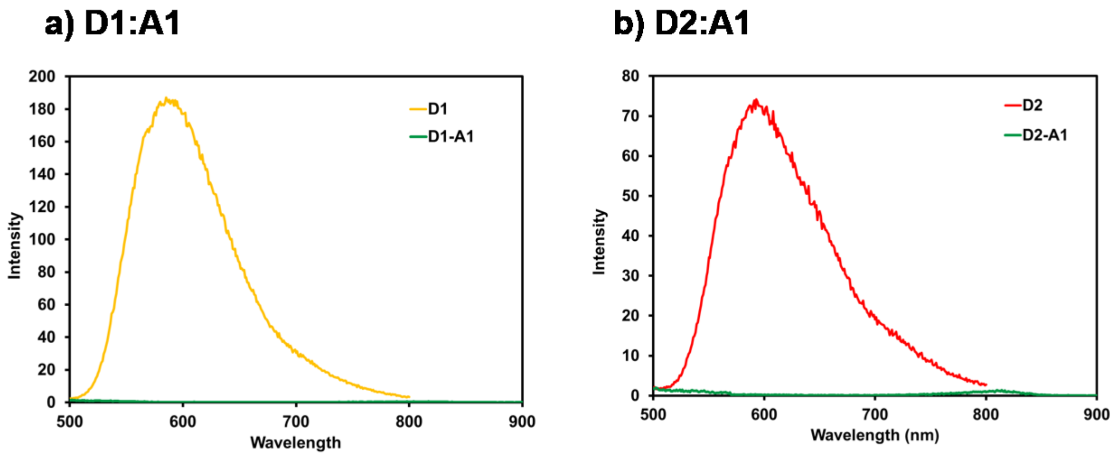

Figure 5.6. PL spectra comparing the fluorescence of one-component donor films with two-component donor-acceptor (1:1 weight ratio) blend films.

As illustrated in **Figure 5.6 a)** and **b)**, both D1 and D2 exhibit significant fluorescence in single-component samples. That is, the electrons are effectively excited from the LUMO to the HOMO and subsequently relax to the ground state, emitting a photon in the process. However, the blend films with equal quantities of donor and acceptor display negligible fluorescence. This indicates that the exciton dissociates at the D-A interface, separating into free charge carriers. The electrons are effectively transferred from D1 or D2 to A1, and are provided with alternate relaxation pathways. As a result, electrons do not relax from the LUMO to the HOMO of the donor and the intensity of the fluorescence is reduced or "quenched". PL quenching provides additional evidence for D-A interactions within the blends, which is a favourable trait for materials in organic solar cells.

Thus far, all experiments described were conducted on both D1-A1 and D2-A1 systems in parallel. For the purpose of streamlining the optimization of thin-films for application in organic solar cells, one system is subsequently studied in greater depth. Since D1 and A1 have identical alkyl end-caps (i.e., swallowtail), which suggests molecular compatibility, the D1-A1 system was selected for further optimization.

It is important to consider the crystallinity of the materials within the active layer; formation of well-ordered crystalline domain can enhance charge transport.[105] The changes in the absorption profiles of the blend films induced by thermal annealing (see **Figure 5.5**) are indicative of electronic changes that may be related to the crystallinity or solid-state ordering of the materials. To further probe the structure of the films, XRD experiments were conducted. XRD patterns of thin films of D1 and A1 are shown in **Figure 5.7 a)** and **b)**, respectively, and are compared to a two-component blend film (1:1 weight ratio of D1 and A1, **Figure 5.7 c)**) before and after annealing at an intermediate temperature (150 °C).

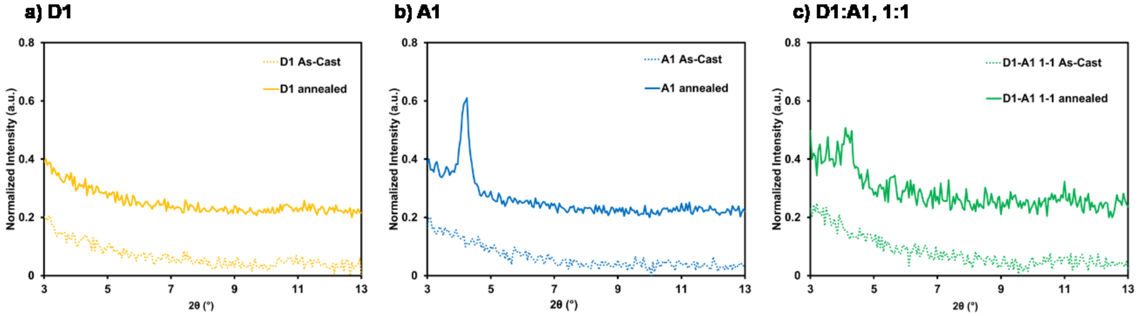

Figure 5.7. XRD patterns of one-component thin-films of a) D1 and b) A1 and c) a two-component D1-A1 blend film acquired before and after thermal annealing for 120 min at 150 °C. The scans were acquired with a range between 3° and 20°, however, no diffraction peaks were observed above $2\theta = 10°$. Thus, only narrow range is used to clearly the show the peaks.

Based on the absence of diffraction peaks for any of the as-cast films, it is assumed that the materials are amorphous within the films or consist of sub-nanometre grains. Upon annealing, the pattern of D1 does not change; no diffraction peaks are observed in the as-cast nor the annealed film, indicating that the material remains amorphous. However, a single diffraction peak is observed for the A1 film at $2\theta = 4.3°$ after annealing – an indication of solid-state ordering. After annealing the blend film, a peak emerges at the same position as in the A1 film, indicative of crystallization of A1 domains.

In a separate experiment, the effect of annealing temperature on crystallinity of the blends is illustrated by comparing XRD patterns of films annealed at 150 °C and at 180 °C (see **Figure 5.8**). Annealing at a higher temperature results in a diffraction peak at the same angle as the film annealed at 150 °C and of the annealed A1 film. This suggests that A1 assumes the same crystalline phase regardless of the annealing temperature. However, the film annealed at high temperature displays a peak of higher-intensity; an indication of the growth of larger crystallites.

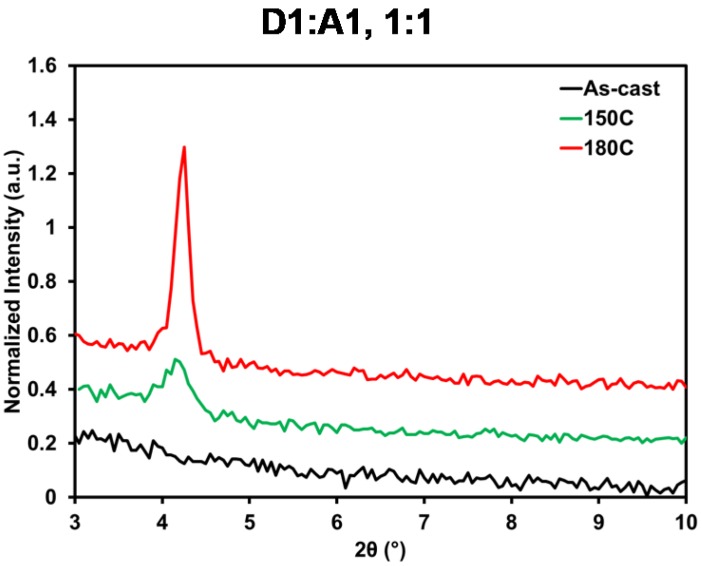

Figure 5.8. XRD patterns of separate films of D1-A1 blends (1:1 weight ratio) comparing the effect of annealing temperature on crystallinity. The films were annealed for 30 minutes at either 150 or 180 °C.

5.3.3. Organic Solar Cell Testing, Part I

Based on the differences in the absorption spectra (**Figure 5.5**) and XRD patterns (**Figure 5.7** and **5.8**) of the blend films, it is clear that electronic and structural changes occur upon thermal annealing. To determine the effect of thermal annealing on PV performance, OSCs were fabricated on three separate substrates using D1:A1 active layers employing a conventional device architecture (see **Figure 5.9 b)**). A detailed fabrication procedure can be found in **Section 5.2.5**. Before deposition of the metal cathode, each substrate was annealed on a hotplate in the glovebox at a different temperature (or tested without annealing).

All devices displayed linear *J*-*V* curves, with very high series resistance and very low J_{sc}. Regardless of annealing condition, very little photocurrent was generated suggesting that the system was not operational in OSC devices.

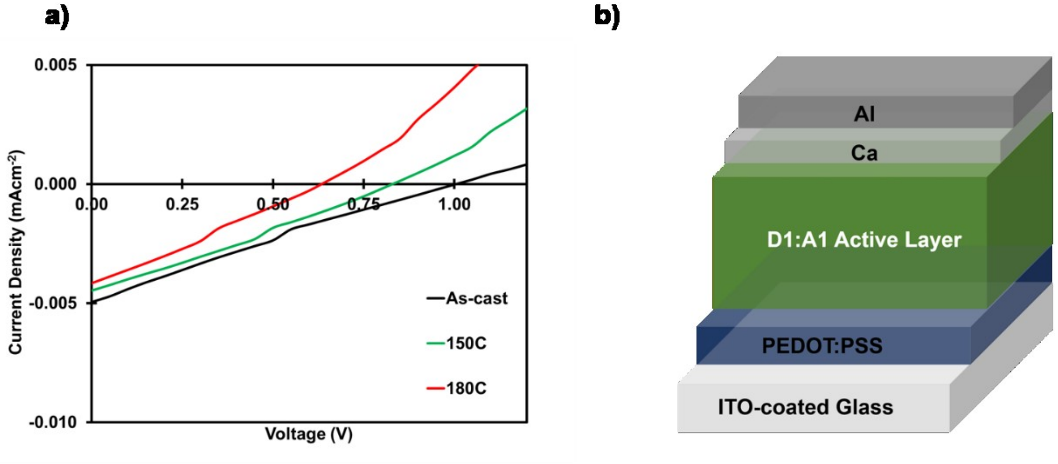

c)

	V_{oc} (V)	J_{sc} (mAcm^{-2})	PCE (%)	FF
As-Cast	1.00	0.0050	0.0012	0.24
150 °C	0.83	0.0045	0.0010	0.28
180 °C	0.63	0.0042	0.0007	0.27

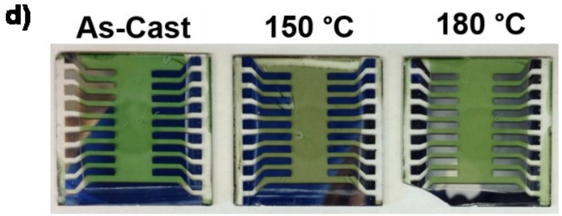

Figure 5.9. a) *J*-*V* curves of representative devices with D1-A1 active-layer blends in a 1:1 ratio. b) An illustration of the layered "conventional"-style architecture. c) A table of performance metrics. d) Photographs of the completed devices.

To gain insight into the cause of the poor device performance, AFM images of the active layers were acquired after device testing (**Figure 5.10**). The images reveal the topography of the active layer surfaces and allow for quantification of the domain sizes. The as-cast film consists of very small domains with minimal phase-separation. Annealing at 150 °C induces growth of larger features that are likely crystalline domains of A1 which correspond to the diffraction peak observed in the XRD pattern. The film annealed at 180 °C consists of large columnar crystallites up to a micron in breadth. These images correlate well with the XRD patterns and confirm the growth of larger crystallites upon high-temperature annealing. The large features observed in the images of the annealed films are likely crystalline domains of A1.

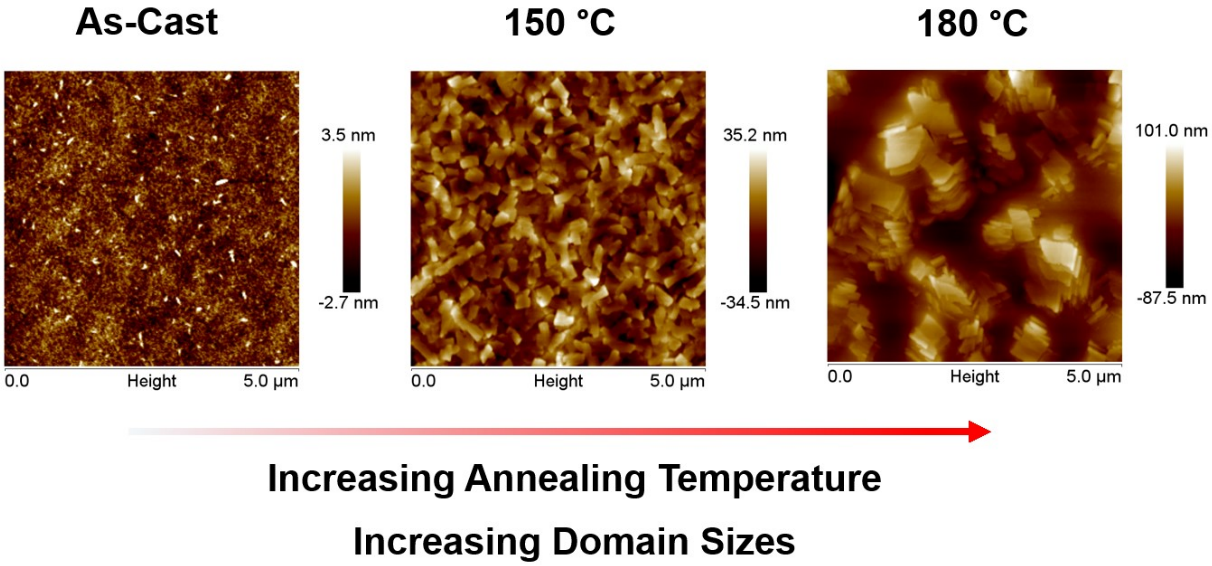

Figure 5.10. 2D AFM images of the D1:A1 active-layer surfaces of the OSC devices.

5.3.4. Conclusions, Part I

The binary blend of D1 and A1 was determined to be a poor system for use in organic solar cells. Despite evidence for PL quenching (**Figure 5.6**), and therefore molecular compatibility as a D-A pair, preliminary devices performed poorly.

AFM reveals very different morphologies between as-cast and annealed films, none of which are likely to display good performance as the active layer in OSCs. Based on the AFM and XRD data, it can be concluded that: i) the amorphous nature of the as-cast films consists of few charge-transport or percolation pathways and ii) the over-crystallization of A1 upon annealing forms domains that are too large for efficient charge generation.

For this system, control of the D-A film morphology was used as a strategy to improve the PV performance. Two strategies that can be used to influence the film morphology are: i) solution-processing techniques and ii) molecular engineering. Two examples of solution-processing techniques are the addition of solvent additives and solvent-vapour annealing (SVA). In a preliminary study described in **Appendix J**, it was observed that addition of solvent additives (**Figure J1**) and solvent-vapour annealing (**Figures J2** and **J3**) modifies the absorption properties of the materials. However, the focus of the project herein is to apply a molecular design strategy to tune the self-assembly of the acceptor and enhance the morphology of the thin films.

5.4. Results and Discussion, Part II

5.4.1. New Acceptors: A Molecular Design Strategy

Moving forward, the unfavourable over-crystallization of the acceptor was addressed through molecular design. The molecular structure of the 2D acceptor was modified to influence its self-assembly within the thin film. D1 continued to be used as the donor in the system for its 3D shape and amorphous nature.

One of the simplest approaches to changing the self-assembly and crystallinity of A1 is by modifying the alkyl chains, taking advantage of the facile synthetic procedure and infinite tunability of this molecular framework. By substituting different alkyl chains for the octyl and swallowtail groups at the central and terminal positions of A1, respectively, the solid-state self-assembly can be controlled to change the morphology of the resulting thin films. Following this approach, another graduate student researcher in the Welch lab, Arthur Hendsbee, synthesized a series of derivatives of A1 (**Figure 5.11**), each with different functional units and/or alkyl chains (**Table 5.1**). Each derivative was designed to be less crystalline than A1 to avoid the large-domain phase separation observed in the D1-A1 system (recall **Figure 5.10**). Since the major driving force for crystallization in π-conjugated materials is π-π interactions between adjacent molecules, side chains were selected to disrupt the π-π interactions and reduce the tendency to crystallize.

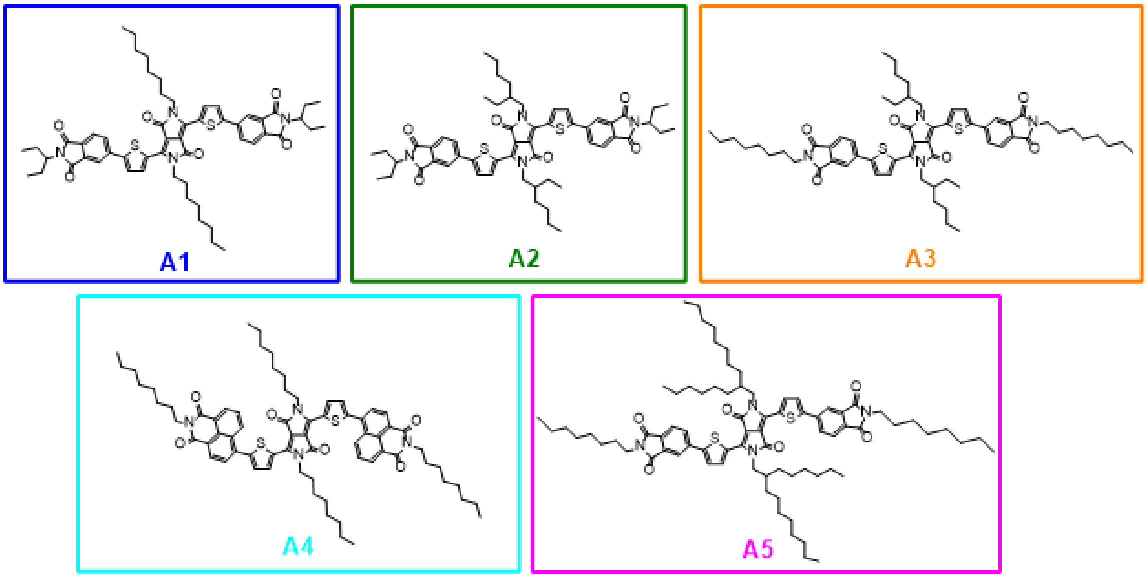

Figure 5.11. Molecular structures of A1 and the four new acceptor derivatives.

Table 5.1. Molecular components used in the acceptor derivatives.

	Central R-groups	**Terminal R-group**	**End-Cap Unit**
A1	Octyl	1-Ethylpropyl	Phthalimide
A2	2-Ethylhexyl	1-Ethylpropyl	Phthalimide
A3	2-Ethylhexyl	Octyl	Phthalimide
A4	Octyl	Octyl	Napthalimide
A5	2-Hexyldecyl	Octyl	Phthalimide

Similar to A1, A2 has terminal swallowtail R-groups, but has a branched 2-ethylhexyl chain stemming from the DPP core as opposed to the linear octyl chains on A1. A3 differs from A2 with the substitution of the swallowtail groups for octyl chains. The bulky branched chains at the core are expected to increase the spatial separation of the DPP units of adjacent molecules thereby weakening the π-π interactions and reducing the tendency to crystallize. In comparison, the linear octyl chains of A1 display strong van der Waals forces, which drive the molecules into a stacking crystalline arrangement. Similar to A3, A5 has terminal octyl chains, but larger branching central groups (2-hexyldecyl).

A4 is unique with larger naphthalimide groups as the terminal electron-withdrawing units in place of phthalimide. Compared to phthalimide, naphthalimide groups induce a greater torsional strain within the π-conjugated backbone, resulting in a less-planar molecule and weaker π-π interactions.

5.4.2. Materials Characterization, Part II

To determine if each of the new acceptors is electronically-compatible with D1, CV experiments were conducted and the HOMO and LUMO energy levels were calculated based on the oxidation and reduction potentials, respectively. A description of how the energy levels were calculated is provided in **Section 4.3.1**. The energy level diagram in **Figure 5.12 a)** shows the relative positions of the frontier molecular orbitals compared to those of D1. Normalized CV plots are provided in **Figure 5.12 b)**. The similar energy levels of the all five acceptors can be explained by the similar conjugated backbone structure.

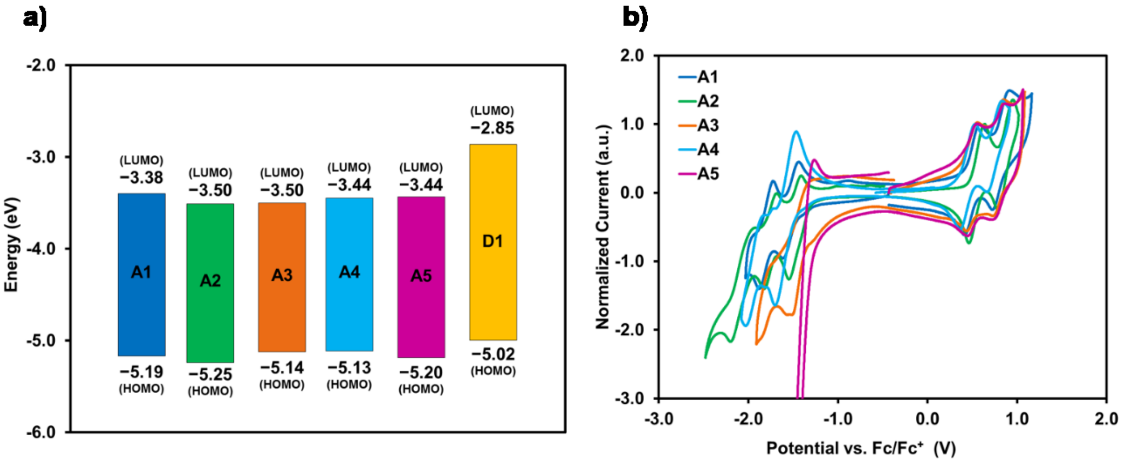

Figure 5.12. a) Energy levels of the frontier molecular orbitals of D1 and the five acceptors determined by CV. The coloured bars represent the bandgaps of each material. b) CV plots for the acceptor derivatives, normalized such that the current of the first oxidation peak is set to unity. The onsets of oxidation and onset of reduction for each material were used to determine the HOMO and LUMO energy levels, respectively. Each CV was acquired by scanning at a rate of 100 mV/s.

5.4.3. Thin-film Characterization, Part II

Thermal annealing was applied to thin-film blends of D1-A*x* systems as a processing technique. The high-temperature condition (i.e., 180 °C) was selected to gain insight into the robustness of the system against crystallization. UV-Vis spectra were acquired on two separate films of each blend: i) one unannealed film and ii) a different film annealed at 180 °C for 10 min after spin-casting. All films were spin-cast onto glass substrates from $CHCl_3$ solutions at concentrations of 20 mg/mL with a donor:acceptor weight ratio of 1:1 (D1:A*x*).

The UV-Vis absorption spectra are compared in the left-hand column of **Figure 5.13**. For all unannealed/as-cast blend films, the absorption of D1 (350-500 nm) is considerably more intense than the absorption attributed to the acceptor (550-700 nm). Significant changes in the absorption profiles of the blends with A2 and A3 are observed after annealing (**Figure 5.13 b) and c)**, respectively). For the D1-A2 blend, three notable changes occur with annealing. First, the two high-energy bands attributed to D1 are blue shifted, similar to what is observed in the D1-A1 blend. Second, a third band is observed in the A2 region, increasing the overall breadth of the absorption. Third, there is an overall relative increase in intensity of the low-energy absorption.

For the D1-A3 film, there is a large red-shift in the low-energy (A3) absorption upon annealing. The two bands also become more distinct with a greater energy-separation. Like A2, a third low-intensity absorption band emerges at the high-energy (blue) end of absorption (580 nm). Also worthy of note is a blue-shift in the low-energy band of D1 from 445 to 425 nm.

In contrast, the blend with A4 shows no change in absorption when annealed. The absorption of A4 is characterized by a single broad band and absorbs weakly compared to the other five acceptors in blends with D1.

For the D1-A5 system, only slight differences are observed in the absorption of the annealed film versus the as-cast film. A new shoulder in the A5 absorption is observed at low-energy, which increases the onset of absorption from 695 to 715 nm. No change is observed in the high-energy region of the spectrum, indicating that the absorption of D1 is not influenced by annealing conditions in this system.

The XRD powder patterns for all of the blend films are also shown in **Figure 5.13 (g-k)** in the right-hand column. Similar to the D1-A1 system, all other blend films display no diffraction peaks before annealing. When annealed, the blends with A1, A2 and A3 display a single diffraction peak at angles of 4.25, 5.75 and 6.15°, respectively. Although a value for *d* can be determined based on the XRD patterns using Bragg's Law, no crystal structure data for these compounds were obtained (attempts were made to grow single crystals, but yielded no crystals with large enough dimensions for single-crystal XRD experiments). For this reason, it cannot be concluded whether the peak in each of the three powder patterns corresponds to π-π or alkyl-alkyl spacing.

Even after annealing at high temperature, no peaks are observed in the D1-A4 blend film. These patterns are in agreement with UV-Vis spectra, suggesting that neither electronic nor structural properties of either material in the blend change after annealing. A single broadened peak can be distinguished from the noise in the post-annealed D1-A5 film. The breadth and low-intensity of the peak suggests that crystalline domains form upon annealing, but are of very small dimensions.

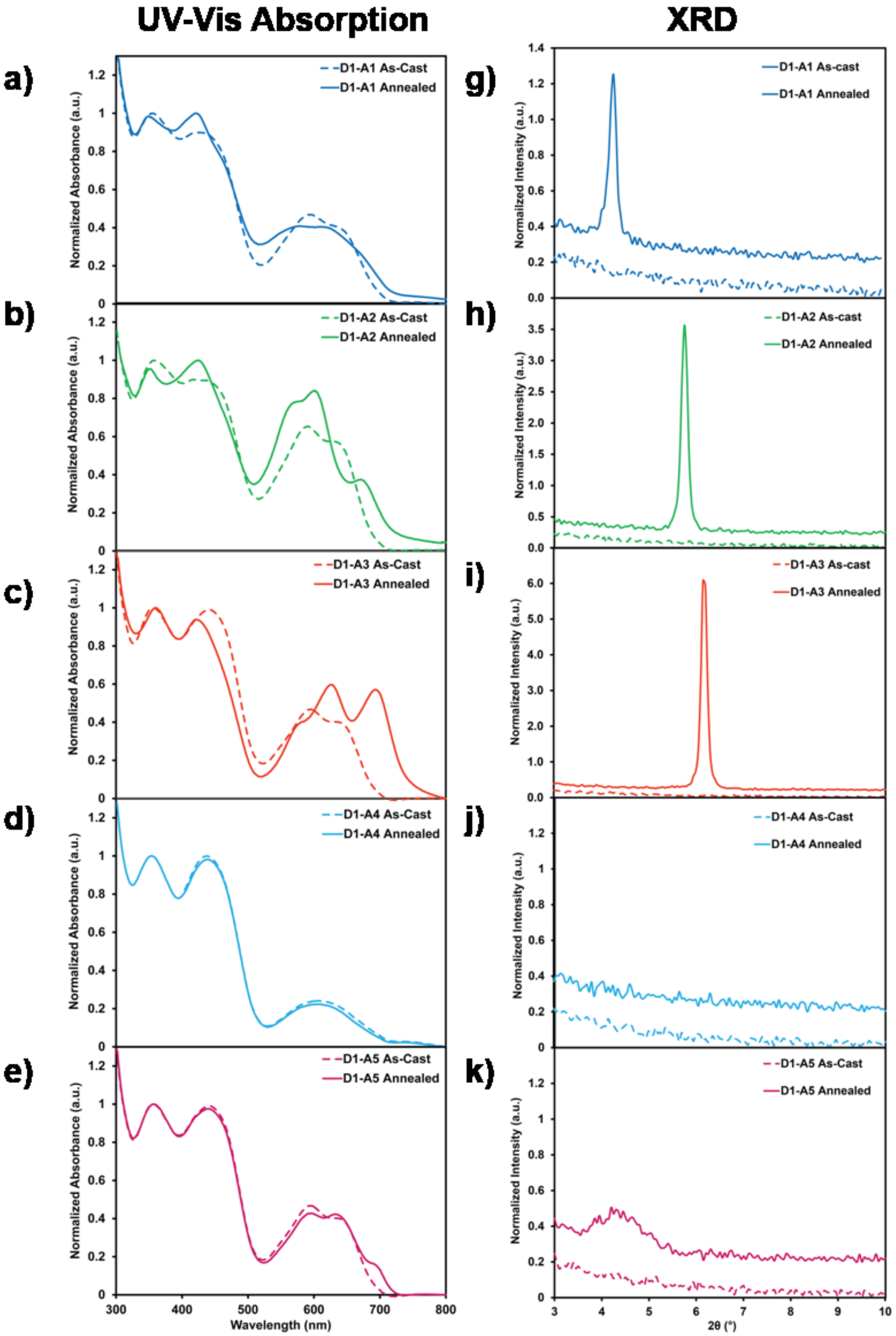

Figure 5.13. Thin-film characterization of D1:A*x* blended films (1:1 by-weight) as-cast (dashed lines) and after thermal annealing at 180 °C for 10 min (solid lines). UV-Vis absorption spectra (a-e) and XRD patterns (g-k) are shown in the left- and right-hand columns, respectively. The scans were acquired with a range between 3° and 20°, however, no diffraction peaks were observed above $2\theta = 10°$. Thus, only a narrow range is depicted.

The AFM images reveal the morphology of the thin-film blends and are shown in **Figure 5.14**. When unannealed, all blend films display a featureless morphology with no indication of phase separation; this is in agreement with the lack of diffraction peaks in the XRD patterns. Similar to the D1-A1 blend (shown again in **Figure 5.14** for comparison), the D1-A2 and D1-A3 blends develop large crystalline domains upon annealing. The D1-A2 annealed blend consists of large mountainous domains measuring microns in lateral dimension, with height deviations up to 200 nm. The D1-A3 blend has smaller, more-compact pebble-like features.

The annealed film of the D1-A4 blend becomes more textured after annealing; however, the features are very small. Based on the lack of diffraction peaks in the XRD pattern (**Figure 5.13 j)**) these features are likely to be amorphous or too small to result in diffraction peaks. Similar to the blend with A4, the A5 blend film roughens upon annealing with large waves spanning microns across the substrate. The roughening is likely formation of the crystalline domains that give rise to the broadened diffraction peak observed in the XRD pattern in **Figure 5.13 k)**.

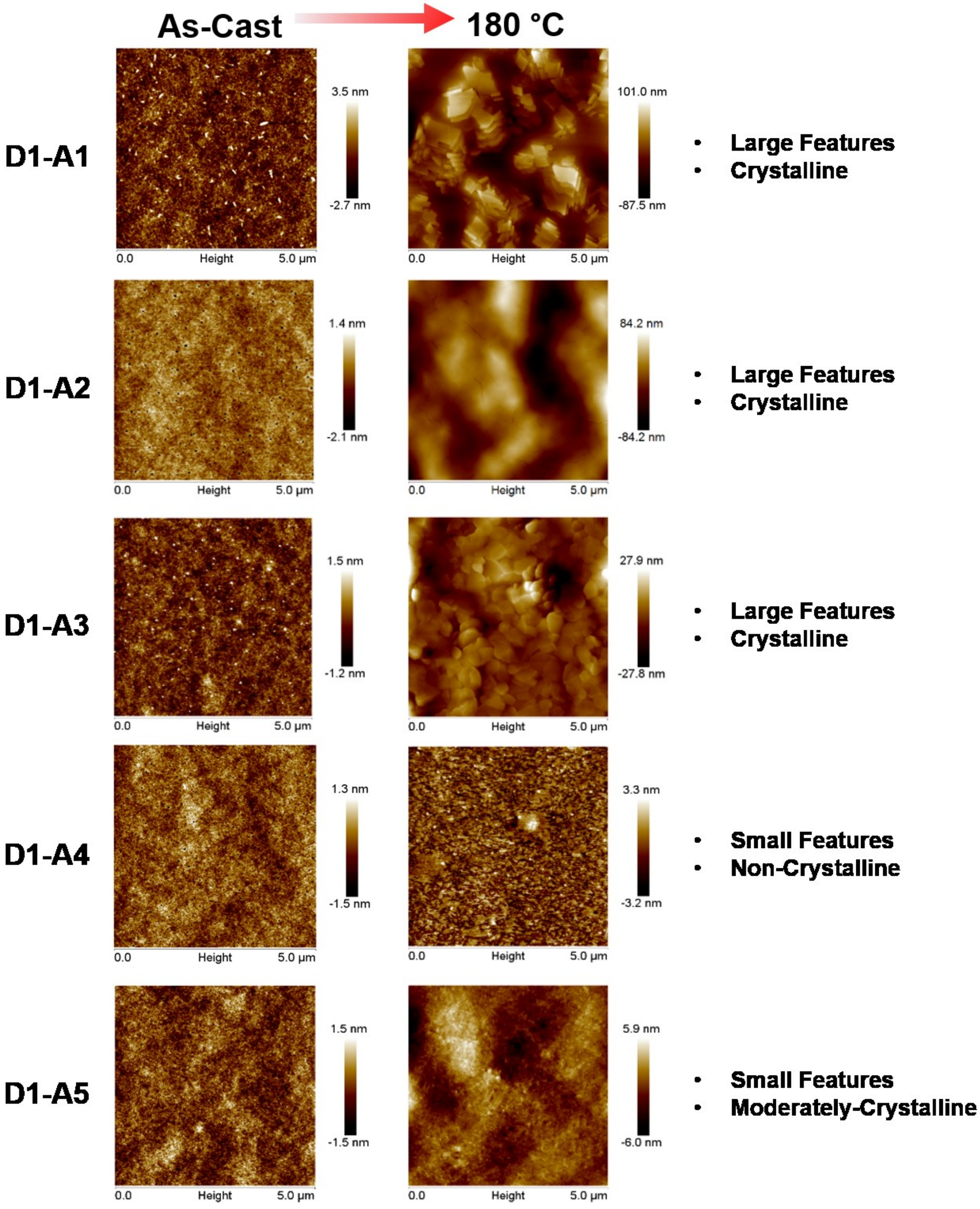

Figure 5.14. 2D AFM topographical images of the surfaces of 1:1 thin-film blends of D1 with acceptors A1, A2, A3, A4 and A5, as-cast and after annealing at 180 °C for 10 min.

5.4.4. Organic Solar Cell Testing, Part II

To compare the PV performance of each new donor-acceptor system as the active layer in OSCs, a batch of devices was fabricated on five different substrates with a conventional device architecture. The fabrication procedure is outlined in **Section 5.2.5**. The metal cathode was deposited onto the unannealed (i.e., as-cast) active layers. All devices were tested as-cast and then annealed on a hotplate at 180 °C for 10 min in the glovebox before re-testing the annealed devices. The *J-V* curves of all devices were linear with very high series resistance and minimal current; no effect was observed from annealing. However, only one batch of devices was made for these D-A combinations. Since the control devices with (*p*-DTS($FBTTh_2)_2$ and PCBM as the donor and acceptor, respectively) had poorer *PCE*s than in previous batches, it is possible that other materials in the cells (e.g., PEDOT:PSS) could have been defective.

5.4.5. Conclusions, Part II

In Part II of this project, it was demonstrated that molecular design (e.g., R-groups and naphthalimide units) influences the electronic and film-forming properties of a series of DPP-based small-molecule derivatives paired with a 3D TPA-based donor.

Based on the absorption spectra, XRD and AFM images, conclusions can be drawn about the effect of R-groups on the self-assembly the materials within solid-state thin-film blends. Among the five acceptor derivatives studied, A1, A2 and A3 clearly respond to heat most significantly as indicated by i) changes in the absorption properties (UV-Vis), and ii) development of large crystalline domains (XRD and AFM) upon annealing. These conditions are not favourable for organic photovoltaic applications – the morphology needs to be robust and resistant to heat in functional solar cells since the cells will increase in temperature during regular cell operation under full-sun exposure.

In contrast, the solid-state ordering of A4 appears to be quite resistant to heat. It can be speculated that the substitution of the napthalimide unit for phthalimide reduces the ordering of the molecules and is responsible for the lack of crystallinity in the film. However, the lack of order in the thin-film may not be ideal; if no ordered domains exist, charge-transport pathways will not be formed and no current will be generated by the cell. In this case, charge-mobility measurements would be needed for confirmation.

A5 exhibits the "best-of-both-worlds" scenario: the film is amorphous as-cast, but develops crystalline networks once annealed at high-temperature; a processing condition that can easily be implemented into the fabrication of cells on an industrial scale. These properties suggest that the blend contains charge-transporting percolation networks and that the morphology and electronics will remain in-tact under normal cell operation.

5.5. Outlook and Future Work

Ultimately, fabrication employing each of the blends using a conventional-style architecture yielded non-functional organic solar cell devices. The reason for the poor performance and low current is unknown based on the current data. Nevertheless, several approaches exist for troubleshooting non-functioning systems:

i) *Device engineering* – investigating alternative device architectures. For example, other members of the Hill lab have discovered that "inverted" solar cell designs can perform better than conventional cells when using the same active layer blends.

ii) *Applying additional experimental techniques to further characterize the blends and provide a better understanding of the materials.* For example, charge-transport properties of the materials (e.g., hole-mobility) of D1 and D2 by fabricating thin-film transistors (TFTs) are important to understanding the cause of the low photocurrents generated by the preliminary devices. It is also of interest to investigate the thermal stability of the materials using TGA, especially when high-temperature annealing is used as a processing technique. These data are also relevant to the application of D2/HTM02 as the hole-transporting layer in PSCs (**Chapter 4**).

iii) *Synthesizing more acceptor derivatives with different R-groups*. The organic semiconductors presented in this study are infinitely tunable – using the results gathered in this study and the trends observed in the effect of side-chain engineering on the electronic and structural properties, efforts can now be focused on derivatives with the best properties. For example, it has been shown that branched chains at the DPP core effectively reduce crystallinity and domain sizes in solid-state thin films.

iv) *Continuing to optimize processing conditions of the existing materials to tune the blend properties*. This strategy includes the application of techniques such as solvent additives, solvent vapour annealing and inert polymer additives. Preliminary investigations of solvent additives and solvent vapour annealing were performed and are discussed in **Appendix J**.

v) *Substitution of other functionalities*. For example, A1 has three types of functional units: i) DPP, ii) thiophene and iii) phthalimide. Each of these units can be replaced by analogous units (e.g., furan) that can alter both the electronic properties (e.g., absorption, bandgap, etc.) and self-assembly (e.g., *d*-spacing, crystallinity, domain sizes, etc.).

While each of these five possible directions holds promise, strategies iv) and v) were selected while continuing to work with similar materials. It is clear that the DPP-based compounds demonstrate interesting electronic and structural responses to processing conditions. For this reason, a related compound (i.e., AX in **Figure 5.15**) was selected as an electron donor paired with a promising non-fullerene acceptor. Strategies outlined in iv) were applied to this new system. Solution-processing techniques were shown to change the electronic, structural and morphological properties of thin-films and could be used to enhance device performance when applied to the fabrication of organic solar cells.

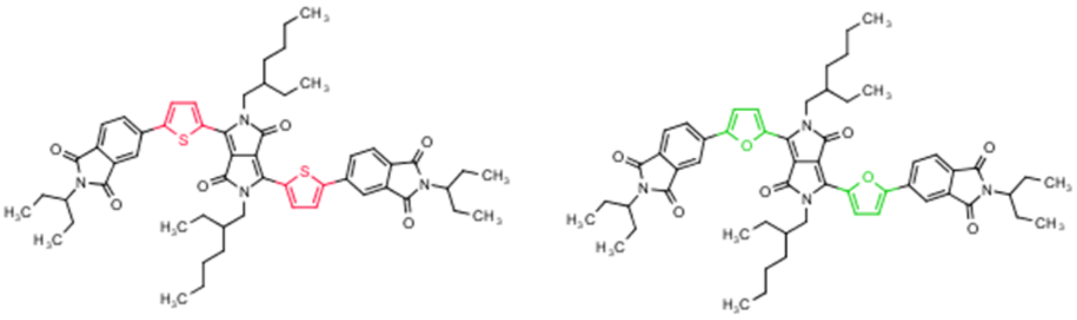

A2 **AX**

Figure 5.15. A comparison of the structures of A2 and AX with thiophene and furan units highlighted in red and green, respectively.

CHAPTER 6 – CONCLUSIONS

The first step in the program was to design a fabrication procedure for high-efficiency perovskite solar cells (**Chapter 3**). Reproducible formation of dense, uniform perovskite films via the dip-coating method is inherently challenging. Methods that increased control over the perovskite conversion step (e.g., deposition via sequential spin-coating) ultimately improved both film quality and reproducibility, leading to better control devices. The first goal in the project (see **Section 1.6**) was achieved; the best-performing devices fabricated using the established procedure achieved a power conversion efficiency of 13.43% (see **Appendix F**), which is comparable to reports made in the literature.[59] Development of a detailed protocol for perovskite solar cell fabrication was important for not only these projects, but for future endeavours in the Welch and Hill laboratories including the development of novel organic hole-transporting materials.

Once a reproducible fabrication procedure for efficient perovskite solar cells was established, new economical hole-transporting materials were investigated to address the issue of the high-cost of spiro-OMeTAD (**Chapter 4**). Triphenylamine-based hole-transporting compounds (HTM01, HTM02 and HTM03) were selected along with a well-known small molecule donor (HTM04) used in high-performance organic solar cells. The simplest hole-transporting material (HTM01) was shown to give the best performance in perovskite solar cells among the triphenylamine compounds. The bandgap of the hole-transporting materials was shown to have little effect on device performance. For example, HTM03 and HTM04 both have narrow bandgaps yet display significantly different performance. Compared to the triphenylamine-based HTMs, spiro-OMeTAD formed the smoothest film over the perovskite active layer, suggesting that it provided better coverage and may explain its better performance as hole-transporting material in perovskite solar cells. In order to achieve the goal of developing a low-cost and efficient HTM for perovskite solar cells using the triphenylamine core, efforts should be focused on increasing solubility in order cast thicker and more uniform hole-transporting layers.

Despite the relatively poor performance of the custom-built triphenylamine-based compounds as HTMs in perovskite solar cells, they demonstrate potential as donors in organic solar cells (**Chapter 5**). The TPA hole-transporting compounds were paired with custom-built acceptors to create fullerene-free donor-acceptor pairs. By characterizing the absorption properties (using UV-Vis spectroscopy) and energy levels (using cyclic voltammetry), organic materials could be assessed for compatibility as donors and acceptors in organic solar cells. The final goal of the project was achieved; two non-fullerene materials were selected (i.e., D1 and A1) that met the three of the five criteria for a promising donor-acceptor pair. Thermal annealing was shown to have an effect on both the electronic and structural properties of D1-A1 blend films. However, the morphologies of the D1-A1 thin films were not appropriate for organic solar cell active layers; the large domain sizes contributed to the poor PV performance. To address the challenge of achieving thin films with a good morphology, new 2D acceptors were tested for compatibility with D1. Molecular design and alkyl chain modifications were shown to significantly change the self-assembly of the A1 derivatives in solid-state thin-film systems. Although these thin film blends were shown to give poor PV performance, the design strategy demonstrates the tunability of organic semiconductors and ease of modifying the properties of organic thin-films.

In summary, the processing conditions used for thin-film formation affects electronic, structural and morphological properties which ultimately influence device performance in solution-processed perovskite and organic solar cells. Understanding how spin-coating techniques influence the thin-film properties of both perovskites and organic semiconductors is necessary for i) optimization of solar cells and ii) development of new functional materials. Through further investigation of processing conditions and development of new derivatives of organic semiconductors, low-cost and efficient solution-processed perovskite and organic solar cells can be realized.

REFERENCES

1 US Energy Information Administration, *Annual Energy Outlook 2015*, Washington, DC, 2015.

2 N. S. Lewis and D. G. Nocera, *Proc. Natl. Acad. Sci.*, 2006, **103**, 15729–15735.

3 US Department of Energy, 2013.

4 J. Yan and B. R. Saunders, *RSC Adv.*, 2014, **4**, 43286–43314.

5 F. C. Krebs, T. Tromholt and M. Jørgensen, *Nanoscale*, 2010, **2**, 873–86.

6 A. Kojima, K. Teshima, Y. Shirai and T. Miyasaka, *J. Am. Chem. Soc.*, 2009, **131**, 6050–6051.

7 H. Zhou, Q. Chen, G. Li, S. Luo, T. Song, H.-S. Duan, Z. Hong, J. You, Y. Liu and Y. Yang, *Science*, 2014, **345**, 542–546.

8 M. A. Green, K. Emery, Y. Hishikawa, W. Warta and E. D. Dunlop, *Prog. Photovoltaics Res. Appl.*, 2015, **23**, 1–9.

9 C. W. Tang, *Appl. Phys. Lett.*, 1986, **48**, 183.

10 G. C. Papavassiliou, G. A. Mousdis and I. B. Koutselas, *Adv. Mater. Opt. Electron.*, 1999, **9**, 265–271.

11 T. Ishihara, *J. Lumin.*, 1994, **60**, 269–274.

12 Y. Kawamura, H. Mashiyama and K. Hasebe, *J. Phys. Soc. Japan*, 2002, **71**, 1694–1697.

13 T. Ishihara, J. Takahashi and T. Goto, *Phys. Rev. B*, 1990, **42**, 11099–11107.

14 J. Calabrese, N. L. Jones, R. L. Harlow, N. Herron, D. L. Thorn and Y. Wang, *J. Am. Chem. Soc.*, 1991, **113**, 2328–2330.

15 D. G. Billing and A. Lemmerer, *CrystEngComm*, 2007, **9**, 236–244.

16 K. Tanaka, T. Takahashi, T. Ban, T. Kondo, K. Uchida and N. Miura, *Solid State Commun.*, 2003, **127**, 619–623.

17 H.-S. Kim, C.-R. Lee, J.-H. Im, K.-B. Lee, T. Moehl, A. Marchioro, S.-J. Moon, R. Humphry-Baker, J.-H. Yum, J. E. Moser, M. Gratzel and N.-G. Park, *Sci. Rep.*, 2012, **2**, 1–7.

18 C. C. Stoumpos, C. D. Malliakas and M. G. Kanatzidis, *Inorg. Chem.*, 2013, **52**, 9019–9038.

19 M. Samiee, S. Konduri, B. Ganapathy, R. Kottokkaran, H. A. Abbas, A. Kitahara, P. Joshi, L. Zhang, M. Noack and V. Dalal, *Appl. Phys. Lett.*, 2014, **105**.

20 C. S. Ponseca, T. J. Savenije, M. Abdellah, K. Zheng, A. Yartsev, T. Pascher, T. Harlang, P. Chabera, T. Pullerits, A. Stepanov, J. P. Wolf and V. Sundström, *J. Am. Chem. Soc.*, 2014, **136**, 5189–5192.

21 S. Avasthi, W. E. McClain, G. Man, A. Kahn, J. Schwartz and J. C. Sturm, *Appl. Phys. Lett.*, 2013, **102**, 203901.

22 A. Marchioro, J. Teuscher, D. Friedrich, M. Kunst, R. van de Krol, T. Moehl, M. Gratzel and J.-E. Moser, *Nat. Phot.*, 2014, **8**, 250–255.

23 J.-Y. Jeng, Y.-F. Chiang, M.-H. Lee, S.-R. Peng, T.-F. Guo, P. Chen and T.-C. Wen, *Adv. Mater.*, 2013, **25**, 3727–3732.

24 O. Malinkiewicz, A. Yella, Y. H. Lee, G. M. Espallargas, M. Graetzel, M. K. Nazeeruddin and H. J. Bolink, *Nat. Phot.*, 2014, **8**, 128–132.

25 Q. Xue, Z. Hu, J. Liu, J. Lin, C. Sun, Z. Chen, C. Duan, J. Wang, C. Liao, W. M. Lau, F. Huang, H.-L. Yip and Y. Cao, *J. Mater. Chem. A*, 2014, **2**, 19598–19603.

26 J. You, Z. Hong, Y. Yang, Q. Chen, M. Cai, T.-B. Song, C.-C. Chen, S. Lu, Y. Liu and H. Zhou, *ACS Nano*, 2014, **8**, 1674–1680.

27 Y. Sun, G. C. Welch, W. L. Leong, C. J. Takacs, G. C. Bazan and A. J. Heeger, *Nat. Mater.*, 2012, **11**, 44–48.

28 L. J. A. Koster, S. E. Shaheen and J. C. Hummelen, *Adv. Energy Mater.*, 2012, **2**, 1246–1253.

29 B. A. Gregg and M. C. Hanna, *J. Appl. Phys.*, 2003, **93**, 3605.

30 I. G. Hill, A. Kahn, Z. G. Soos and R. A. Pascal, Jr, *Chem. Phys. Lett.*, 2000, **327**, 181–188.

31 A. K. K. Kyaw, D. H. Wang, V. Gupta, J. Zhang, S. Chand, G. C. Bazan and A. J. Heeger, *Adv. Mater.*, 2013, **25**, 2397–2402.

32 G. Yu, J. Gao, J. C. Hummelen, F. Wudl and A. J. Heeger, *Science*, 1995, **270**, 1789–1791.

33 A. Hagfeldt, G. Boschloo, L. Sun, L. Kloo and H. Pettersson, *Chem. Rev.*, 2010, **110**, 6595–6663.

34 a. J. Oostra, E. Smits, D. de Leeuw, P. Blom and J. Michels, *Phys. Chem. Chem. Phys.*, 2015, **17**, 21501–21506.

35 F. C. Krebs, *Sol. Energy Mater. Sol. Cells*, 2009, **93**, 394–412.

36 C. W. Extrand, *Polym. Eng. Sci.*, 1994, **34**, 390.

37 S. J. L. Billinge and I. Levin, *Science*, 2007, **316**, 561–5.

38 N. Maskil and M. Deutsch, *Phys. Rev. A*, 1988, **37**, 2947–2952.

39 A. Shafiee, M. M. Salleh and M. Yahaya, *Sains Malaysiana*, 2011, **40**, 173–176.

40 M. M. Lee, J. Teuscher, T. Miyasaka, T. N. Murakami and H. J. Snaith, *Science*, 2012, **338**, 643–647.

41 J. M. Ball, M. M. Lee, A. Hey and H. J. Snaith, *Energy Environ. Sci.*, 2013, **6**, 1739–1743.

42 P. Docampo, J. M. Ball, M. Darwich, G. E. Eperon and H. J. Snaith, *Nat. Commun.*, 2013, **4**, 1–6.

43 G. E. Eperon, V. M. Burlakov, P. Docampo, A. Goriely and H. J. Snaith, *Adv. Funct. Mater.*, 2014, **24**, 151–157.

44 S. D. Stranks, G. E. Eperon, G. Grancini, C. Menelaou, M. J. P. Alcocer, T. Leijtens, L. M. Herz, A. Petrozza and H. J. Snaith, *Science*, 2013, **342**, 341–344.

45 G. C. Xing, N. Mathews, S. Y. Sun, S. S. Lim, Y. M. Lam, M. Gratzel, S. Mhaisalkar and T. C. Sum, *Science*, 2013, **342**, 344–347.

46 D. Liu and T. L. Kelly, *Nat. Phot.*, 2014, **8**, 133–138.

47 M. Liu, M. B. Johnston and H. J. Snaith, *Nat.*, 2013, **501**, 395–398.

48 K. Hwang, Y. Jung, Y. Heo, F. H. Scholes, S. E. Watkins, J. Subbiah, D. J. Jones, D. Kim and D. Vak, *Adv. Mater.*, 2015, **27**, 1241–1247.

49 M. Xiao, F. Huang, W. Huang, Y. Dkhissi, Y. Zhu, J. Etheridge, A. Gray-Weale, U. Bach, Y.-B. Cheng and L. Spiccia, *Angew. Chemie*, 2014, **126**, 10056–10061.

50 K. Liang, D. B. Mitzi and M. T. Prikas, *Chem. Mater.*, 1998, **10**, 403–411.

51 J. Burschka, N. Pellet, S.-J. Moon, R. Humphry-Baker, P. Gao, M. K. Nazeeruddin and M. Gratzel, *Nat.*, 2013, **499**, 316–319.

52 N. J. Jeon, J. H. Noh, Y. C. Kim, W. S. Yang, S. Ryu and S. Il Seok, *Nat. Mater.*, 2014, **13**, 897–903.

53 Z. Xiao, C. Bi, Y. Shao, Q. Dong, Q. Wang, Y. Yuan, C. Wang, Y. Gao and J. Huang, *Energy Environ. Sci.*, 2014, **7**, 2619–2623.

54 B.-E. Cohen, S. Gamliel and L. Etgar, *Apl Mater.*, 2014, **2**, 081502.

55 P. A. Beckmann, *Cryst. Res. Technol.*, 2010, **45**, n/a–n/a.

56 J. Yang, B. D. Siempelkamp, D. Liu and T. L. Kelly, *ACS Nano*, 2015, **9**, 1955–63.

57 A. Dualeh, N. Tétreault, T. Moehl, P. Gao, M. K. Nazeeruddin and M. Grätzel, *Adv. Funct. Mater.*, 2014, **24**, 3250–3258.

58 J.-H. Im, I.-H. Jang, N. Pellet, M. Grätzel and N.-G. Park, *Nat. Nano.*, 2014, **9**, 927–932.

59 C. Bi, Y. Shao, Y. Yuan, Z. Xiao, C. Wang, Y. Gao and J. Huang, *J. Mater. Chem. A*, 2014, **2**, 18508–18514.

60 O. Knop, R. E. Wasylishen, M. A. White, T. S. Cameron and M. J. M. Vanoort, *Can. J. Chem.* , 1990, **68**, 412–422.

61 A. Dualeh, P. Gao, S. Il Seok, M. K. Nazeeruddin and M. Grätzel, *Chem. Mater.*, 2014, **26**, 6160–6164.

62 T. Baikie, Y. Fang, J. M. Kadro, M. Schreyer, F. Wei, S. G. Mhaisalkar, M. Graetzel and T. J. White, *J. Mater. Chem. A*, 2013, **1**, 5628–5641.

63 N. J. Jeon, H. G. Lee, Y. C. Kim, J. Seo, J. H. Noh, J. Lee and S. Il Seok, *J. Am. Chem. Soc.*, 2014, **136**, 7837–7840.

64 C. He, Q. He, Y. Yi, G. Wu, F. Bai, Z. Shuai and Y. Li, *J. Mater. Chem.*, 2008, **18**, 4085.

65 S. Allard, M. Forster, B. Souharce, H. Thiem and U. Scherf, *Angew. Chemie - Int. Ed.*, 2008, **47**, 4070–4098.

66 P. Strohriegl and J. V. Grazulevicius, *Adv. Mater.*, 2002, **14**, 1439–1452.

67 Z. Li, T. Ye, S. Tang, C. Wang, D. Ma and Z. Li, *J. Mater. Chem. C*, 2015, **3**, 2016–2023.

68 J. J. Wang, S. R. Wang, X. G. Li, L. F. Zhu, Q. B. Meng, Y. Xiao and D. M. Li, *Chem. Commun.*, 2014, **50**, 5829–5832.

69 J. H. Heo, S. H. Im, J. H. Noh, T. N. Mandal, C. S. Lim, J. A. Chang, Y. H. Lee, H. J. Kim, A. Sarkar, M. K. Nazeeruddin, M. Gratzel and S. I. Seok, *Nat. Photonics*, 2013, **7**, 487–492.

70 H. Choi, S. Park, S. Paek, P. Ekanayake, M. K. Nazeeruddin and J. Ko, *J. Mater. Chem. A*, 2014, **2**, 19136–19140.

71 S. Do Sung, M. S. Kang, I. T. Choi, H. M. Kim, H. Kim, M. Hong, H. K. Kim and W. I. Lee, *Chem. Commun.*, 2014, **50**, 14161–14163.

72 T. Malinauskas, M. Daskeviciene, G. Bubniene, I. Petrikyte, S. Raisys, K. Kazlauskas, V. Gaidelis, V. Jankauskas, R. Maldzius, S. Jursenas and V. Getautis, *Chem. Eur. J.*, 2013, **19**, 15044–15056.

73 N. Satoh, T. Nakashima and K. Yamamoto, *J. Am. Chem. Soc.*, 2005, **127**, 13030–13038.

74 D. J. Burke and D. J. Lipomi, *Energy Environ. Sci.*, 2013, **6**, 2053–2066.

75 M. N. Belgacem and A. Gandini, *Monomers, polymers and composites from renewable resources*, Elsevier, 2011.

76 O. Gidron, A. Dadvand, Y. Sheynin, M. Bendikov and D. F. Perepichka, *Chem. Commun.*, 2011, **47**, 1976–1978.

77 A. D. Hendsbee, J.-P. Sun, T. M. McCormick, I. G. Hill and G. C. Welch, *Org. Electron.*, 2015, **18**, 118–125.

78 K. Oniwa, T. Kanagasekaran, T. Jin, M. Akhtaruzzaman, Y. Yamamoto, H. Tamura, I. Hamada, H. Shimotani, N. Asao, S. Ikeda and K. Tanigaki, *J. Mater. Chem. C*, 2013, **1**, 4163–4170.

79 J. Liu, B. Walker, A. Tamayo, Y. Zhang and T.-Q. Nguyen, *Adv. Funct. Mater.*, 2013, **23**, 47–56.

80 A. B. Tamayo, M. Tantiwiwat, B. Walker and T.-Q. Nguyen, *J. Phys. Chem. C*, 2008, **112**, 15543–15552.

81 J. A. Love, C. M. Proctor, J. Liu, C. J. Takacs, A. Sharenko, T. S. van der Poll, A. J. Heeger, G. C. Bazan and T.-Q. Nguyen, *Adv. Funct. Mater.*, 2013, **23**, 5019–5026.

82 T. S. van der Poll, J. A. Love, T.-Q. Nguyen and G. C. Bazan, *Adv. Mater.*, 2012, **24**, 3646–3649.

83 Y. Zhao, A. M. Nardes and K. Zhu, *Appl. Phys. Lett.*, 2014, **104**, 21306.

84 J. Meyer, S. Hamwi, M. Kröger, W. Kowalsky, T. Riedl and A. Kahn, *Adv. Mater.*, 2012, **24**, 5408–27.

85 A. Abrusci, S. D. Stranks, P. Docampo, H.-L. Yip, A. K. Y. Jen and H. J. Snaith, *Nano Lett.*, 2013, **13**, 3124–3128.

86 M. G. Helander, M. T. Greiner, Z. B. Wang, W. M. Tang and Z. H. Lu, *J. Vac. Sci. & Technol. A*, 2011, **29**, 011019.

87 G. C. Welch, L. A. Perez, C. V. Hoven, Y. Zhang, X.-D. Dang, A. Sharenko, M. F. Toney, E. J. Kramer, T.-Q. Nguyen and G. C. Bazan, *J. Mater. Chem.*, 2011, **21**, 12700.

88 M. Cheng, C. Chen, X. Yang, J. Huang, F. Zhang, B. Xu and L. Sun, *Chem. Mater.*, 2015, **27**, 1808–1814.

89 L. A. Perez, J. T. Rogers, M. A. Brady, Y. Sun, G. C. Welch, K. Schmidt, M. F. Toney, H. Jinnai, A. J. Heeger, M. L. Chabinyc, G. C. Bazan and E. J. Kramer, *Chem. Mater.*, 2014, **26**, 6531–6541.

90 R. B. Ross, C. M. Cardona, D. M. Guldi, S. G. Sankaranarayanan, M. O. Reese, N. Kopidakis, J. Peet, B. Walker, G. C. Bazan, E. Van Keuren, B. C. Holloway and M. Drees, *Nat. Mater.*, 2009, **8**, 208–212.

91 Y. He, H.-Y. Chen, J. Hou and Y. Li, *J. Am. Chem. Soc.*, 2010, **132**, 1377–1382.

92 J. Roncali, P. Leriche and A. Cravino, *Adv. Mater.*, 2007, **19**, 2045–2060.

93 D. M. Guldi, *Chem. Commun.*, 2000, 321–327.

94 L. A. Perez, K. W. Chou, J. A. Love, T. S. van der Poll, D.-M. Smilgies, T.-Q. Nguyen, E. J. Kramer, A. Amassian and G. C. Bazan, *Adv. Mater.*, 2013, **25**, 6380–6384.

95 J.-Y. Pan, L.-J. Zuo, X.-L. Hu, W.-F. Fu, M.-R. Chen, L. Fu, X. Gu, H.-Q. Shi, M.-M. Shi, H.-Y. Li and H.-Z. Chen, *ACS Appl. Mater. Interfaces*, 2013, **5**, 972–980.

96 J. Zhang, D. Deng, C. He, Y. He, M. Zhang, Z.-G. Zhang, Z. Zhang and Y. Li, *Chem. Mater.*, 2011, **23**, 817–822.

97 J. Zhang, Y. Yang, C. He, D. Deng, Z. Li and Y. Li, *J. Phys. D. Appl. Phys.*, 2011, **44**, 475101.

98 H. Shang, H. Fan, Y. Liu, W. Hu, Y. Li and X. Zhan, *Adv. Mater.*, 2011, **23**, 1554–1557.

99 A. D. Hendsbee, J.-P. Sun, L. R. Rutledge, I. G. Hill and G. C. Welch, *J. Mater. Chem. A*, 2014, **2**, 4198–4207.

100 Y. Kim, A. Ballantyne, J. Nelson and D. Bradley, *Org. Electron.*, 2009, **10**, 205–209.

101 S. Qu and H. Tian, *Chem. Commun. (Camb).*, 2012, **48**, 3039–51.

102 Z. Du, W. Chen, Y. Chen, S. Qiao, X. Bao, S. Wen, M. Sun, L. Han and R. Yang, *J. Mater. Chem. A*, 2014, **2**, 15904–15911.

103 B. Kan, Q. Zhang, M. Li, X. Wan, W. Ni, G. Long, Y. Wang, X. Yang, H. Feng and Y. Chen, *J. Am. Chem. Soc.*, 2014, **136**, 15529–15532.

104 Z. Yi, W. Ni, Q. Zhang, M. Li, B. Kan, X. Wan and Y. Chen, *J. Mater. Chem. C*, 2014, **2**, 7247–7255.

105 J. W. Ryan and Y. Matsuo, *Sci. Rep.*, 2015, **5**.

106 J.-H. Im, C.-R. Lee, J.-W. Lee, S.-W. Park and N.-G. Park, *Nanoscale*, 2011, **3**, 4088–4093.

107 H. Li, K. Fu, A. Hagfeldt, M. Grätzel, S. G. Mhaisalkar and A. C. Grimsdale, *Angew. Chemie - Int. Ed.*, 2014, **53**, 4085–4088.

108 S. Sun, T. Salim, N. Mathews, M. Duchamp, C. Boothroyd, G. Xing, T. C. Sum and Y. M. Lam, *Energy Environ. Sci.*, 2014, **7**, 399–407.

109 H. Li, K. Fu, P. P. Boix, L. H. Wong, A. Hagfeldt, M. Grätzel, S. G. Mhaisalkar and A. C. Grimsdale, *ChemSusChem*, 2014, **7**, 3420–3425.

110 L. Zheng, Y. S. Chung, Y. Ma, L. Zhang, L. Xiao, Z. Chen, S. Wang, B. Qu and Q. Gong, *Chem. Commun.*, 2014, **1**, 1–4.

111 D. Bi, L. Yang, G. Boschloo, A. Hagfeldt and E. M. J. Johansson, *J. Phys. Chem. Lett.*, 2013, **4**, 1532–1536.

112 F. Matteocci, S. Razza, F. Di Giacomo, S. Casaluci, G. Mincuzzi, T. M. Brown, A. D'Epifanio, S. Licoccia and A. Di Carlo, *Phys. Chem. Chem. Phys.*, 2014, **16**, 3918–3923.

113 Y. S. Kwon, J. Lim, H.-J. Yun, Y.-H. Kim and T. Park, *Energy Environ. Sci.*, 2014, **7**, 1454–1460.

114 H. J. Snaith and M. Gratzel, *Appl. Phys. Lett.*, 2006, **89**, 262113–262114.

115 A. Abate, T. Leijtens, S. Pathak, J. Teuscher, R. Avolio, M. E. Errico, J. Kirkpatrik, J. M. Ball, P. Docampo, I. McPherson and H. J. Snaith, *Phys. Chem. Chem. Phys.*, 2013, **15**, 2572–2579.

116 W. H. Howie, J. E. Harris, J. R. Jennings and L. M. Peter, *Sol. Energy Mater. Sol. Cells*, 2007, **91**, 424–426.

117 Y. Huang, W. Wen, S. Mukherjee, H. Ade, E. J. Kramer and G. C. Bazan, *Adv. Mater.*, 2014, **26**, 4168–4172.

118 H. Li, T. Earmme, G. Ren, A. Saeki, S. Yoshikawa, N. M. Murari, S. Subramaniyan, M. J. Crane, S. Seki and S. A. Jenekhe, *J. Am. Chem. Soc.*, 2014, **136**, 14589–14597.

119 W. Jiang, L. Ye, X. Li, C. Xiao, F. Tan, W. Zhao, J. Hou and Z. Wang, *Chem. Commun.*, 2014, **50**, 1024–1026.

120 Y. Zang, C.-Z. Li, C.-C. Chueh, S. T. Williams, W. Jiang, Z.-H. Wang, J.-S. Yu and A. K.-Y. Jen, *Adv. Mater.*, 2014, **26**, 5708–14.

121 J. Zhao, Y. Li, H. Lin, Y. Liu, K. Jiang, C. Mu, T. Ma, J. Y. Lin Lai, H. Hu, D. Yu and H. Yan, *Energy Environ. Sci.*, 2015, **8**, 520–525.

122 W. Chen, X. Yang, G. Long, X. Wan, Y. Chen and Q. Zhang, *J. Mater. Chem. C*, 2015, **3**, 4698–4705.

123 S.-Y. Liu, C.-H. Wu, C.-Z. Li, S.-Q. Liu, K.-H. Wei, H.-Z. Chen and A. K.-Y. Jen, *Adv. Sci.*, 2015, **2**, 1500014.

124 Y. Liu, C. Mu, K. Jiang, J. Zhao, Y. Li, L. Zhang, Z. Li, J. Y. L. Lai, H. Hu, T. Ma, R. Hu, D. Yu, X. Huang, B. Z. Tang and H. Yan, *Adv. Mater.*, 2015, **27**, 1014–1014.

125 Y. Lin, P. Cheng, Y. Li and X. Zhan, *Chem. Commun.*, 2012, **48**, 4773–4775.

126 Y. Lin, Y. Wang, J. Wang, J. Hou, Y. Li, D. Zhu and X. Zhan, *Adv. Mater.*, 2014, **26**, 5137–5142.

127 A. Sharenko, D. Gehrig, F. Laquai and T.-Q. Nguyen, *Chem. Mater.*, 2014, **26**, 4109–4118.

128 A. Sharenko, C. M. Proctor, T. S. van der Poll, Z. B. Henson, T.-Q. Nguyen and G. C. Bazan, *Adv. Mater.*, 2013, **25**, 4403–6.

129 R. Singh, E. Aluicio-Sarduy, Z. Kan, T. Ye, R. C. I. MacKenzie and P. E. Keivanidis, *J. Mater. Chem. A*, 2014, **2**, 14348–14353.

130 M. Li, J. Liu, X. Cao, K. Zhou, Q. Zhao, X. Yu, R. Xing and Y. Han, *Phys. Chem. Chem. Phys.*, 2014, **16**, 26917–26928.

APPENDIX A – SOLUTION PREPARATIONS

TiO_2 Precursor Solution Preparation

To form the compact TiO_2 layer, a precursor solution containing titanium (IV) isopropoxide ($Ti(iPrO)_4$), purchased from Sigma-Aldrich, Product No. 377996-25ML, 99.999% purity) was prepared using a modified procedure outlined by Abrusci *et al.*[85] Two solutions were prepared in separate 8 mL vials. The first vial contained 2530 μL of ethanol and 35 μL of a stock solution of 2.0 M HCl (prepared in air). The second solution contained 2530 μL of ethanol and 370 μL of $Ti(iPrO)_4$ (prepared in the glovebox). The first solution was added dropwise to the second solution while the second was stirred in air to form the final sol-gel solution.

PbI_2 Solution Preparation

A 1.0 M PbI_2 solution was prepared by weighing 461 mg of PbI_2 (purchased from Alfa-Aesar, Product No. 12724, 99.9985% purity) in a 4- or 8-mL Teflon-capped vial and adding 1000 μL of dry DMF and a stir bar. The solid was dissolved by heating and stirring on a hotplate and maintained at the desired temperature throughout the deposition procedure. The temperature of the solution was recorded by attaching a thermocouple probe to the outer wall of the vial. The 0.5 M and 0.75 M PbI_2 solutions were prepared in a similar fashion, but dissolved by stirring at RT.

Spiro-OMeTAD (Doped) Solution Preparation

The HTM solution was prepared using the recipe described by Liu *et al.*[46]: 80 mg of spiro-OMeTAD (purchased from Sigma-Aldrich, Product No. 792071-1G, 99% purity), 28.5 μL of 4-tert-butylpyridine (tBP, purchased from Sigma-Aldrich, Product No. 142379-25G, 96% purity) and 17.5 μL of a 520 mg/mL solution of lithium-bis(trifluoromethane)sulfonimide (Li-TFSI, purchased from Sigma-Aldrich, Product No.

544094-5G, 99.95% purity) in acetonitrile was combined and dissolved 1 mL of chlorobenzene. The solid spiro-OMeTAD was weighed onto a weigh paper and then transferred to a 4.0 mL Teflon®-capped vial. tBP, chlorobenzene and the Li-TFSI solution were transferred separately into the vial using micropipettes. The mixture was dissolved using a stir-bar and stirring at RT.

APPENDIX B – SYNTHESIS OF CH_3NH_3I

The synthesis of CH_3NH_3I was performed using the procedure documented by Im *et al*. as a guideline.[106] A 250 mL round-bottom flask was loaded with 27 mL of 55 wt-% $HI_{(aq)}$ (BC Scientific, Product No. 0152-01), 30 mL of a 40% aqueous solution of methylamine (Fisher Scientific, Product No. 00983) and a stir bar. The reaction mixture was stirred in an ice bath in air for 3 h. The solvent was removed using a rotary evaporator, leaving behind a brown solid. The solid product was slurried in diethyl ether for 30 minutes and filtered using a Buchner funnel. This process was repeated twice more to wash the product. The washed final product was recrystallized from a minimum amount of ethanol, cooled, and filtered to recover white crystals. The crystals were washed with diethyl ether and dried in a vacuum oven overnight. The solid crystalline product was stored in an Ar-filled glovebox prior to use.

APPENDIX C – OTHER FACTORS INFLUENCING LEAD IODIDE FILM MORPHOLOGY

Solution Temperature (T_{solution})

It was determined that the minimum value of T_{solution} for complete dissolution of a 1.0 M solution of PbI_2 in DMF was 50 °C. Increasing T_{solution} above the threshold temperature (i.e., 50 °C) results in perovskite films with smaller crystallites (**Figure C1**). However, there are no significant differences between the films cast from solutions held at 70, 90, 110, and 130 °C in terms of crystallite size and distribution.

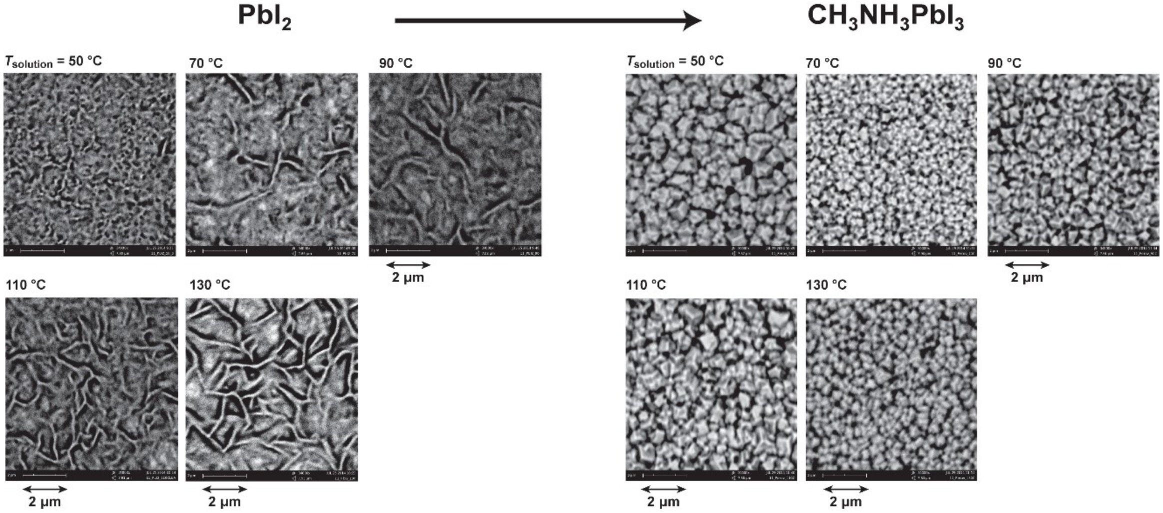

Figure C1. The effect of solution temperature. SEM images of PbI_2 films spin-cast on TiO_2 compact films at different temperatures and the corresponding $CH_3NH_3PbI_3$ films after conversion via dipping. The solution was spin-coated using a spin speed of 3000 rpm for 30 s onto TiO_2-coated substrates heated at 100 °C.

The Effect of Atmosphere

By depositing onto a hot substrate *or* performing the deposition under an inert (i.e., Ar) atmosphere, film coverage can be drastically improved. In both cases, the films exhibit smaller grain sizes and better coverage than the unheated film in ambient. It is also observed that the film spun under ambient conditions with a heated substrate had a lower frequency of pinholes than the one spun in the glovebox (see **Figure C2**). This demonstrates that inert conditions are not required for uniform film formation – simply heating the substrate prior to deposition is an effective method for hindering crystal growth and increasing film coverage.

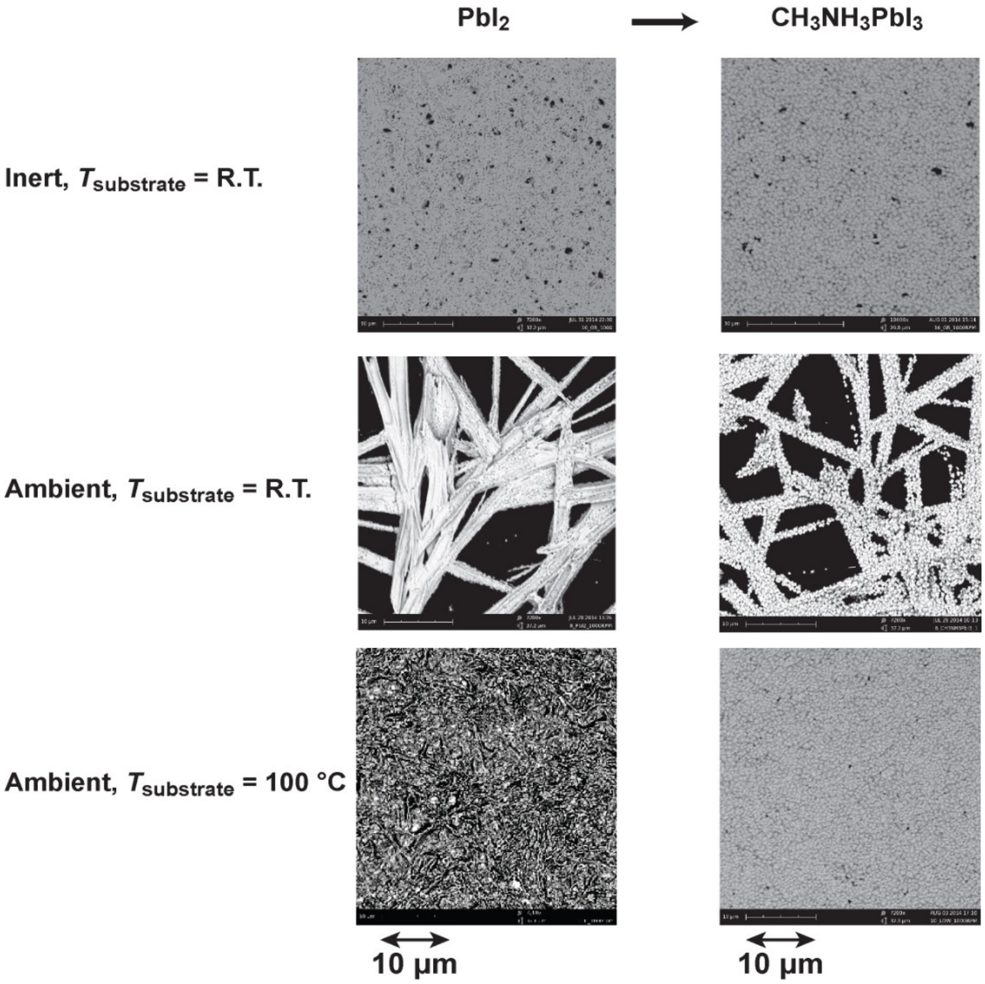

Figure C2. The effect of atmosphere on PbI_2 film formation. Depicted are SEM images of PbI_2 and corresponding $CH_3NH_3PbI_3$ films spin-cast from a 1.0 M PbI_2 solution in DMF held at 70 °C. The solution was spin-coated in either air (ambient) or N_2 (inert) using a spin speed of 1000 rpm for 30 s onto substrates held at either R.T. or 100 °C.

APPENDIX D – PEROVSKITE X-RAY DIFFRACTION PEAK INTENSITIES

Table D1. Peak areas corresponding to XRD plots in **Figure 3.15**, determined by applying the Pearson VII function and using Jade software.

[MAI]	Peak Area for PbI_2 (001)	PbI_2 (001) Error	Peak Area for $MAPbI_3$ (110)	$MAPbI_3$ (110) Error	$I_{PbI2}/(I_{PbI2} + I_{MAPbI3})$	$I_{PbI2}/(I_{PbI2} + I_{MAPbI3})$ Error
20	5662.7	37.8	2319.9	26.7	0.70938	0.010559
30	3760.1	32.3	2636.1	26.4	0.587865	0.009255
40	1933.3	25.6	3833.2	31.1	0.335264	0.006842
50	71.4	12.5	4592.7	N/A	0.015308	0.00379

For simplicity, let:

$I_{PbI2}/(I_{PbI2} + I_{MAPbI3}) = A$

Error for $I_{PbI2}/(I_{PbI2} + I_{MAPbI3}) = \delta A$

$I_{PbI2} = B$

Error for $I_{PbI2} = \delta B$

$I_{MAPbI3} = C$

Error for $C = \delta C$

Calculation of error:

$\delta A = |A|\ (2*(\ \delta B/B)^2 + (\delta C/C)^2)^{1/2}$

APPENDIX E – THIOPHENE IN ORGANIC SMALL MOLECULES

Thiophene heterocyclic derivatives are important electron-donating (D) functionalities in organic HTMs. There are a number of reports of high-performance small-molecule HTMs designed for applications in PSCs based on thiophene derivatives – the molecular structure of three examples are given in **Figure E1**. In the first example, a simple HTM known as "H101" was synthesized and shown to achieve a respectable *PCE* of 10.6 % without the use of dopants. In this molecule, 3,4-ethylenedioxythiophene (EDOT) core[107] was used in an shown to produce higher currents than unsubstituted benzene or thiophene. EDOT is a common functional group in HTMs, with a popular example being the mixture of poly(3,4-ethylenedioxythiophene) polystyrene sulfonate (PEDOT:PSS). Although mostly used for OPVs, PEDOT:PSS is now gaining attention as the HTL in inverted PSCs.[23,24,108] In a subsequent paper, the same group reported a derivative of H101 with a tetra-substituted thiophene core (aka "H111") that achieved a *PCE* of 14.9 %;[109] to date, it is the highest reported PCE for PSCs without Spiro-OMeTAD. A third example is a thiophene oligomer with benzodithiophene (BDT) core, named "DR3TBDTT".[110] From DFT studies the HOMO is located at BDT unit, and the LUMO occupies the electron-drawing ethylrhodanine groups at both ends, suggesting that that hole-transport may be occurring primarily at the core in this acceptor–donor–acceptor backbone electronic structure. Three thiophene bridging units extend conjugation from the core to the ends. Unlike the previous two examples, devices with DR3TBDTT performed *worse* when doped with Li-TFSI and tBP, suggesting that structural differences are a factor in the response to such dopants.

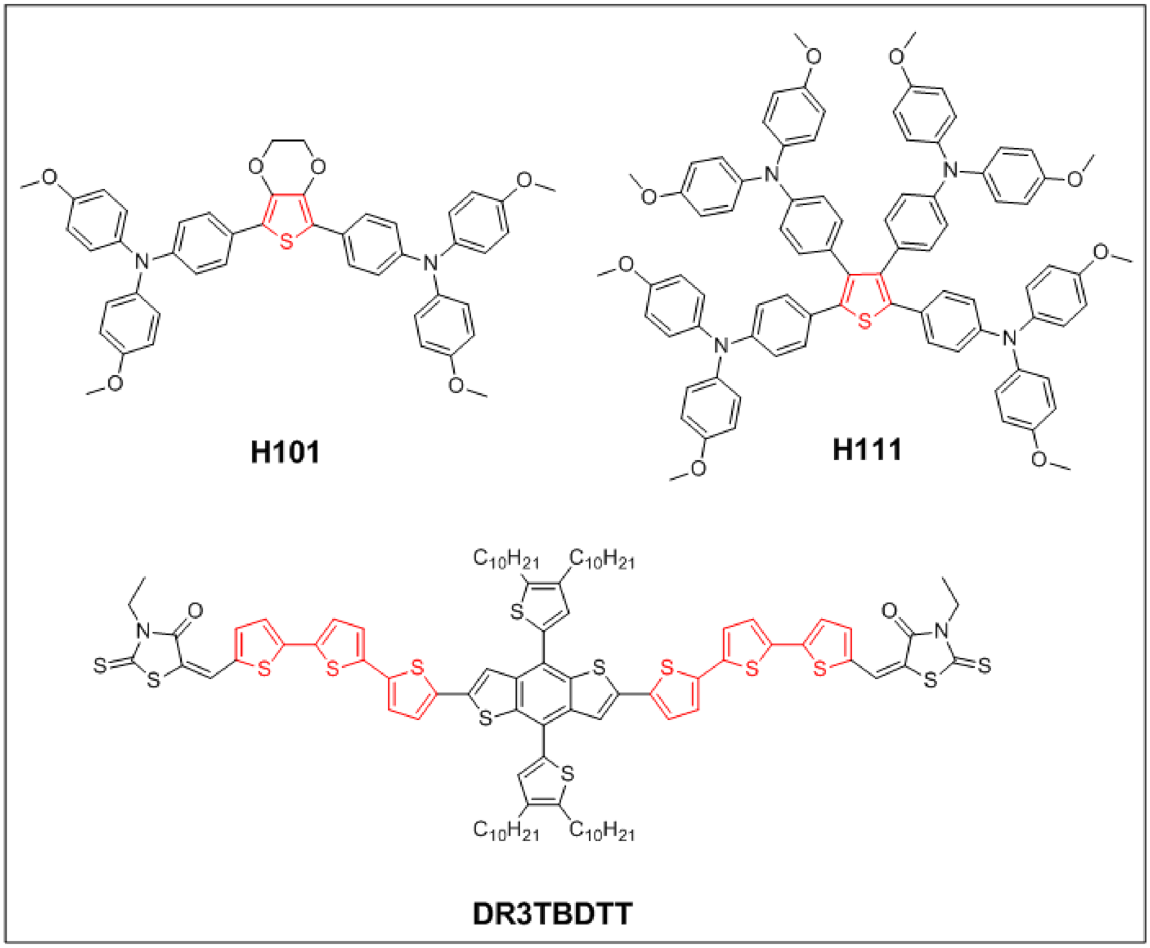

Figure E1. Structures of small-molecule HTMs for PSCs with thiophene functionalities highlighted in red.

Polymer HTMs with thiophene units also have precedence for applications in *PCE*s. Three examples are shown in **Figure E2**. P3HT, a narrow band-gap semiconductor with a successful history as a donor in OSCs has been shown to yield efficiencies as the HTL in PSCs, with *PCE*s of up to 6.7%.[69,111,112] Although P3HT has excellent hole mobility, the major disadvantage of using it as an HTM in PSCs is its elevated HOMO level – corresponding devices have lower V_{oc}s. Design strategies to improve thiophene-based polymeric HTMs have included the addition of acceptor units, such as benzothiadiazole (e.g., poly-[2,1,3-benzothiadiazole-4,7-diyl[4,4-bis(2-ethylhexyl)-4H-cyclopenta[2,1-b:3,4-b′]dithiophene-2,6-diyl]] or PCDTBT).[69] Although this particular polymer showed an increased the V_{oc} of PSC devices, the J_{sc} was significantly lower than analogous devices with P3HT as the HTM. Alternatively, insertion of a DPP unit (e.g., poly[2,5-bis(2-decyldodecyl)-pyrrolo[3,4-c]pyrrole-1,4(2H,5H)-dione-(E)-1,2-di(2,20-bithio phen-5-yl)-ethene] or PDPPDBTE in **Figure E2**)[113] to a thiophene-conjugated backbone effectively reduced the HOMO, producing a polymeric HTM demonstrating a much higher V_{oc} while maintaining a similar J_{sc} as devices with P3HT.

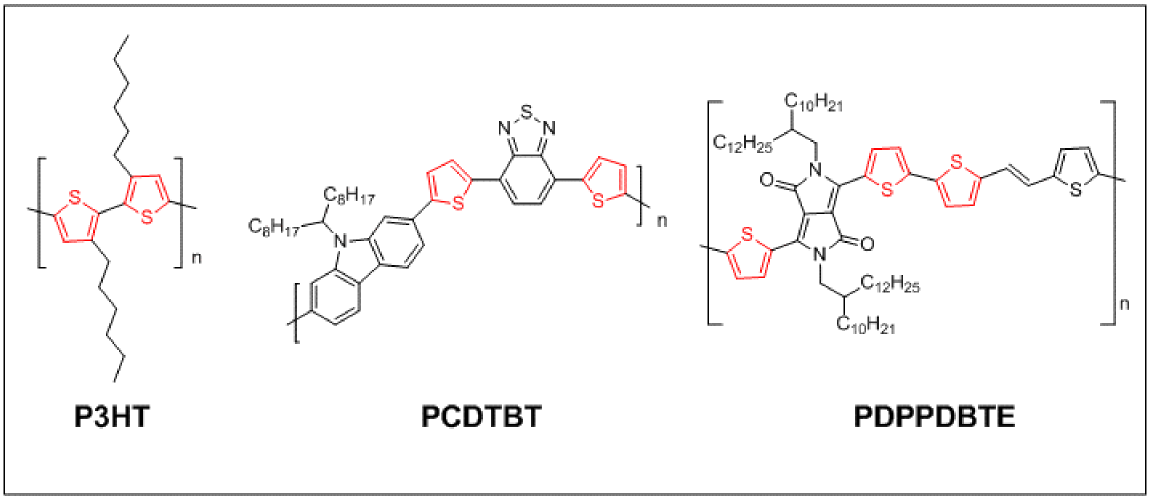

Figure E2. Polymer HTMs for PSCs with thiophene functionalities highlighted in red.

APPENDIX F – THE EFFECT OF DOPANTS ON HOLE-TRANSPORT

Although it is well-known that the addition of p-type dopants to spiro-OMeTAD greatly enhance device performance (see **Appendix F** for experimental data), [114–116] these additives are hygroscopic and detrimental to the long-term stability of the cell.[110] **Figure F1** depicts the *J-V* curves of devices fabricated with Spiro-OMeTAD doped with Li-TFSI and tBP and without dopants. The devices with the doped HTM had a higher *FF* and higher V_{oc} as a result of lower series resistance.

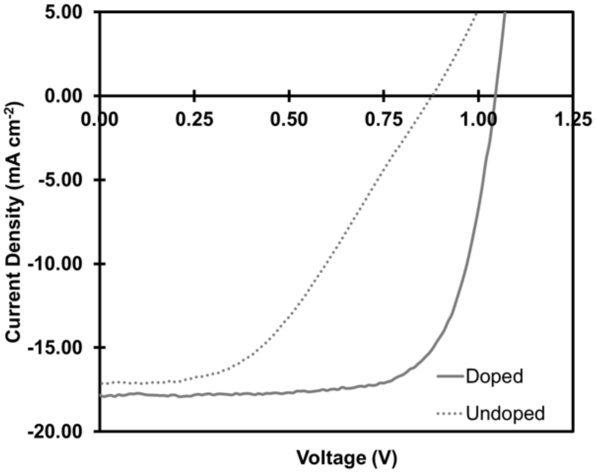

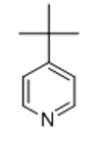

4-*tert*-Butylpyridine
(tBP)

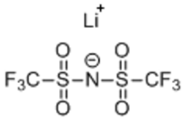

Lithium Bis(trifluoromethane)sulfonimide
(Li-TFSI)

HTM	V_{oc} (V)	J_{sc} (mAcm^{-2})	PCE (%)	FF
Doped Spiro	1.06	17.81	13.43	0.71
Undoped Spiro	0.88	17.16	6.58	0.43

Figure F1. A comparison of *J-V* curves of the best-performing devices with Spiro-OMeTAD doped with Li-TFSI and tBP against devices undoped Spiro-OMeTAD as the HTL. The plots were obtained by scanning from +2.0 V to 0.0 V at a rate of 10 ms per data point under 1.5 G (one Sun) illumination.

APPENDIX G – THE EFFECT OF NON-CONJUGATED POLYMER ADDITIVES ON FILM FORMATION OF HOLE-TRANSPORT LAYERS

Non-conjugated polymers were combined with HTM04 to observe the effect of inert additives in the HTL of PSCs. The binary blends were made by spin-coating HTL precursor solutions containing polystyrene (PS) or trimethyl-terminated polydimethylsiloxane (PDMS) and HTM04 dissolved in CB. The concentration of HTM04 was kept at 25 mg/mL and the amount of polymer was equivalent to 2% of the HTM by weight (i.e., 0.5 mg/mL). PS was selected because it has been shown to improve the performance of small-molecule bulk-heterojunction OSCs with HTM04 as the donor.[117] PDMS was selected for its previous success as an inert additive in HTLs with another thiophene-containing small-molecule HTM.[110] It was found that the addition of PDMS helped planarize the surface of the HTL, resulting in an increase in J_{sc} and FF.

Indeed, devices with binary blends of HTM04 and PDMS showed higher J_{sc} than their neat-film counterparts, contributing to a better *PCE* (3.33 % versus 2.76 % for the HTM04 neat film). Devices with HTM04 with 2% PS showed little difference in performance compared to the neat-film devices (see **Figure G1**).

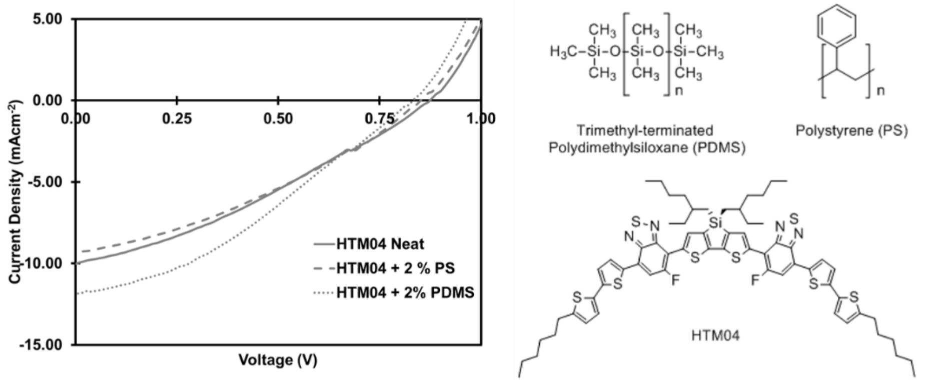

Figure G1. A comparison *J-V* curves for the best-performing devices with HTM04 with and without non-conjugated polymer additives. The plots were obtained by scanning from +2.0 V to 0.0 V at a rate of 10 ms per data point under 1.5 G illumination.

Table G1. Summary of *J-V* characteristics of devices with HTM04 as the HTM with and without non-conjugated polymer additives. All measurements were taken by scanning from +2.0 V to 0.0 V with a scan delay of 10 ms under 1.5 G illumination.

HTL	V_{oc} (V)	J_{sc} (mA cm^{-2})	*PCE* (%)	FF	Shunt Resistance (Ω/cm^2)	Series Resistance (Ω/cm^2)
HTM04 neat	0.89	10.02	2.76	0.31	1.74×10^{5}	7.46×10^{-2}
HTM04 + 2% PS	0.87	9.35	2.71	0.33	2.13×10^{5}	7.34×10^{-2}
HTM04 + 2% PDMS	0.85	11.87	3.33	0.33	2.20×10^{5}	7.58×10^{-2}

AFM images of the HTL surfaces reveal that films with HTM04 and PDMS on a perovskite active layer are less rough than HTM04 neat films on perovskite (see **Figure G2**). The images suggest that the addition of PDMS planarizes the HTL by filling in the deep "valleys" in the perovskite film. On the other hand, the roughness of the films with and without PS are very similar. Interestingly, addition of either polymer improved the shunt resistance of the devices, which gives further evidence that the blends are providing better coverage of the perovskite layer, and thus passivating shunt pathways.

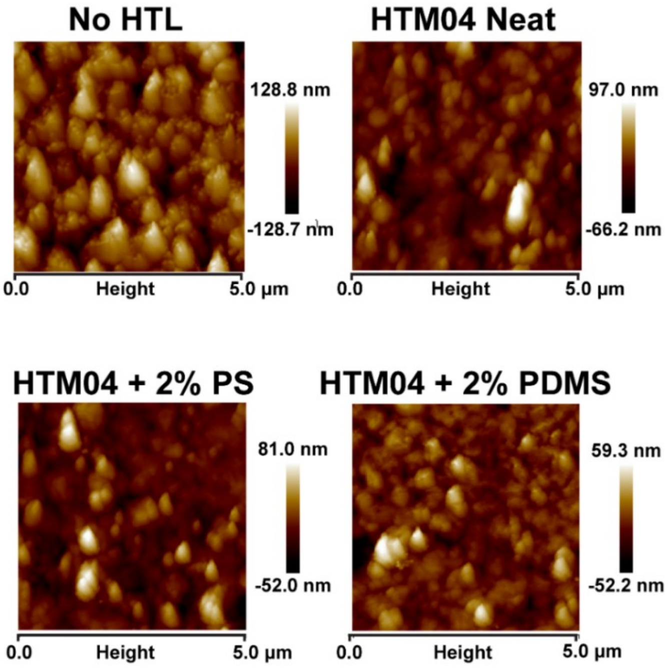

Figure G2. 2D AFM images of HTL surfaces of HTM04 with and without polymer additives on a perovskite film. An image of a neat perovskite film is shown for comparison.

Table G2. Roughness parameters for HTL films on perovskite obtained from 2D AFM images.

	No HTL	**HTM04 neat**	**HTM04 + 2% PS**	**HTM04 + 2% PDMS**
Surface Area (μm²)	26	23	24	25
R_{RMS} (nm)	35	20	17	14
R_{a} (nm)	28	14	12	11
$R_{\max}$ (nm)	246	170	139	139

[a] R_{RMS}, the root mean square (RMS) average of height deviations relative to the mean image data plane. [b] R_{a}, the average of the absolute values of the surface height deviations relative to the mean plane. [c] $R_{\max}$, the vertical distance between the highest and lowest data points in the image.

In conclusion, it has been shown that addition of PDMS increases planarity of the HTM04 surface and contributes to higher photocurrent than neat-films of HTM04. This strategy for device improvement seems to be especially important when fabricating devices with PHJ perovskite active layers in which large perovskite crystal domains are common and difficult to cover.

APPENDIX H – 3D NON-FULLERENE ACCEPTORS

A well-studied strategy in the design of high-performing non-fullerene acceptors is mimicry of the advantageous 3D shape of PCBM. Three categories of 3D non-fullerene acceptors are: i) twisted dimers, ii) tetramers and iii) TPA-based star-shapes. Jenekhe and co-workers[118] have demonstrated a successful design methodology for the synthesis of non-planar non-fullerene acceptors (see **Figure H1** for structure); 3D twisted dimeric structures were shown to exhibit more homogeneous thin-films than their 2D monomeric units, ultimately delivering higher performance in OPV devices with a 2D polymer donor. Other 3D dimeric structures include bridged perylene-diimide (PDI) derivatives.[119–121]

Non-planar tetrameric non-fullerene acceptors contain four conjugated units spatially distributed around a common core. One strategy is to use a tetrahedral sp^3-hybridized C[122] or Si[123] core with four arms. Recently, Yan *et al*. fashioned a tetramer with four PDI units bridged at a tetraphenylethylene core, yielding an impressive *PCE* of 5.5% (**Figure H1**).[124]

The third category is trimeric acceptors that have a TPA core. The first report of a 3D TPA-based acceptor displayed modest performance with a *PCE* of 1.2% with P3HT as the polymer donor.[125] Two years later, the same group improved upon their original design by using electron-deficient PDI units and synthesizing a new TPA-based acceptor with higher electron mobility and better PV performance.[126]

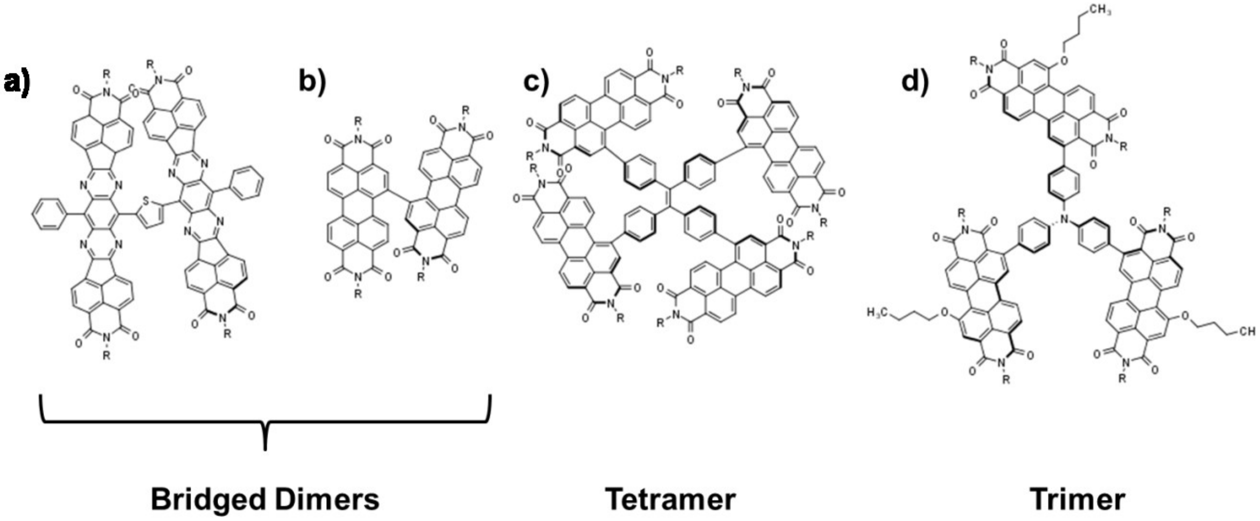

Figure H1. Examples of non-fullerene acceptors, including bridged dimers (a)[118] and b)[119]), c) a tetramer[124], and d) a TPA trimer with PDI side-arm units.[126]

APPENDIX I – VARYING DONOR-ACCEPTOR RATIOS

Figure I1 depicts UV-Vis spectra of D1-A1 and D2-D1 blends spin-cast from solutions with varying D:A weight ratios. It was confirmed that by reducing the D:A weight ratio, the relative absorption intensity of A1 increases, balancing the absorption of the film across the spectrum. However, if the concentration of the precursor solution is fixed at 30 mg/mL, while reducing the D:A ratio, the total absorbance of the film is reduced. Since there is a trade-off between absorption balance and total absorbance, only fabrication of devices with the different ratios can determine the optimal ratio for OPVs.

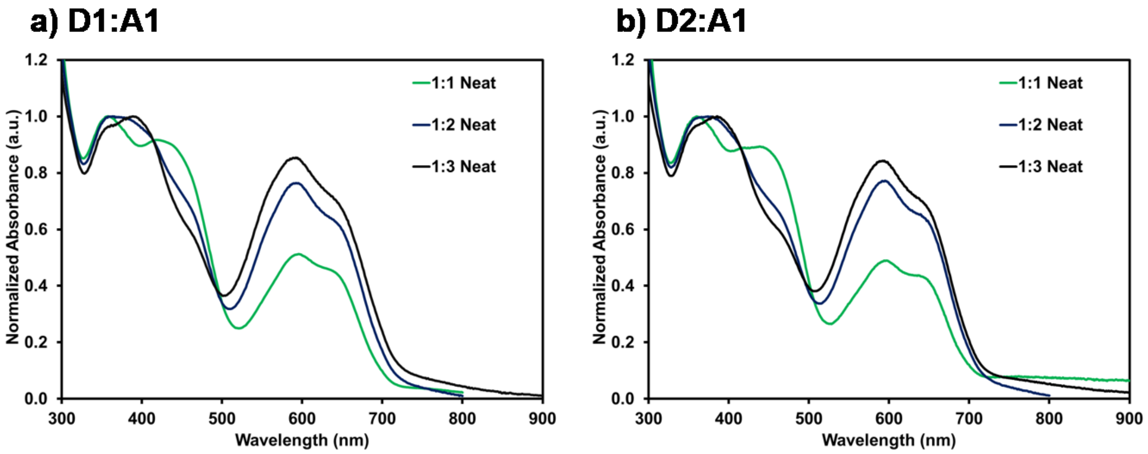

Figure I1. UV-Vis absorption spectra acquired for as-cast blend films of a) D1-A1 and b) D2-A1 with varying D:A weight ratios. Spectra were acquired by Arthur Hendsbee.

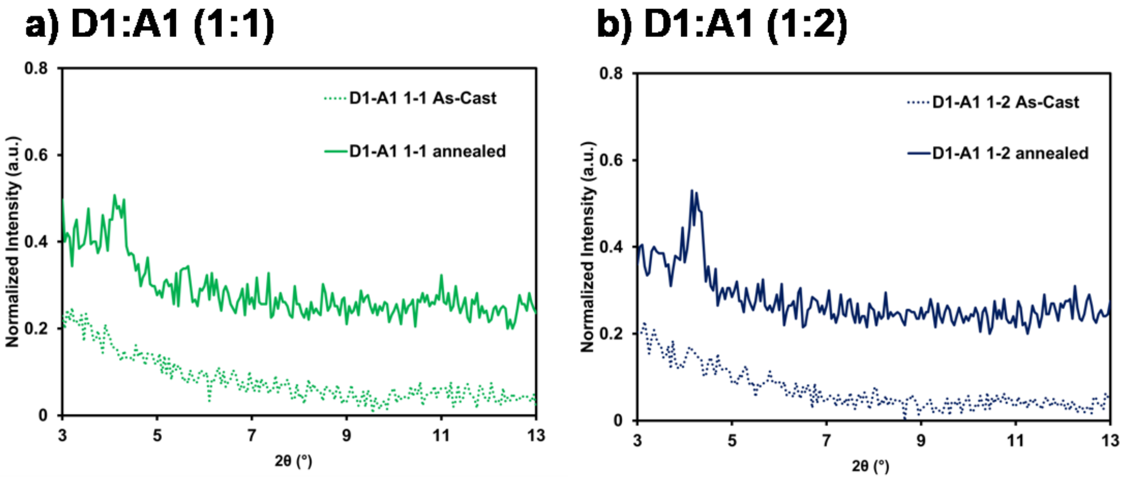

Figure I2. XRD patterns of thin-film blends with D1-A1 ratios of a) 1:1 and b) 1:2 acquired before and after thermal annealing for 120 min at 150 °C. The A1 diffraction peak is higher in relative intensity in the pattern for the 1:2 film than in the 1:1 due to the higher quantity of crystalline material.

APPENDIX J – SOLVENT ADDITIVES AND SOLVENT VAPOUR ANNEALING

In **Chapter 4**, thermal annealing was used as a processing technique to modify the structure and morphology of thin film blends of D1-A1. Two other techniques that can be applied to formation of thin films and the fabrication of OSCs are the use of solvent additives and solvent vapour annealing.

Solvent Additives

Solvent additives are typically high-boiling liquids that are co-dissolved with the photoactive materials in the spin-coating solution. The most common solvent additive is 1,8-diiodooctane (DIO), which has been shown to yield remarkable improvements in a variety of OPV systems.[127–129] Nevertheless, other solvent additives have also been shown to induce different and favourable changes in thin film OSCs.[130]

In a preliminary study, three different high-boiling compounds were selected as solvent additives for the D1-A1 systems. In separate samples, either DIO, 4-trifluoromethyl benzoic acid (4-TFBA) or 1-naphthaldehyde (1-NA) were used as solvent additives in the solutions containing D1 and A1 in a 1:1 weight ratio with a total solid concentration of 20 mg/mL. A stock solution of each solvent additive was first prepared in $CHCl_3$ at a concentration of 4% (v/v%). D1-A1 solutions were prepared by combining the weighed solid compounds with a measured mixture of the solvent-additive stock solution and pure $CHCl_3$ as per the volumes listed in **Table J1**. All volumes of solvent and solvent additive were measured with either a 200-µL or 1000-µL micropipette.

Table J1. Compositions of solvents with solvent-additive.

Volume % Additive	**Total Solution Volume (µL)**	**Volume of Additive (µL)**	**Volume of Stock Solution (µL)**	**Volume of Pure $CHCl_3$ (µL)**
0.4	1000	4	100	900
1.0	1000	10	250	750

From the UV-Vis spectra depicted in **Figure J1**, it is observed that small quantities of each of the solvent additives have negligible effects on the absorption properties of D1 and A1. However, increasing the concentration of the DIO (**Figure J1 a)**) and 1-NA (**Figure J1 c)**) to 1.0% results in changes to the absorption profile of A1 and emergence of three distinct bands and a reduction in the intensity of the high-energy absorption band of D1. On the other hand, addition of 1.0% of 1-TFBA results in a broadening of the A1 absorption, but no significant changes in the absorption of D1. Although it is clear that electronic changes occur within the films from the presence of the solvent additives, structural changes could not be detected using XRD (**Figure J1 d), e), f))**. In this case, AFM is an ideal tool to probe the films for morphological changes. However, these experiments have yet to be performed.

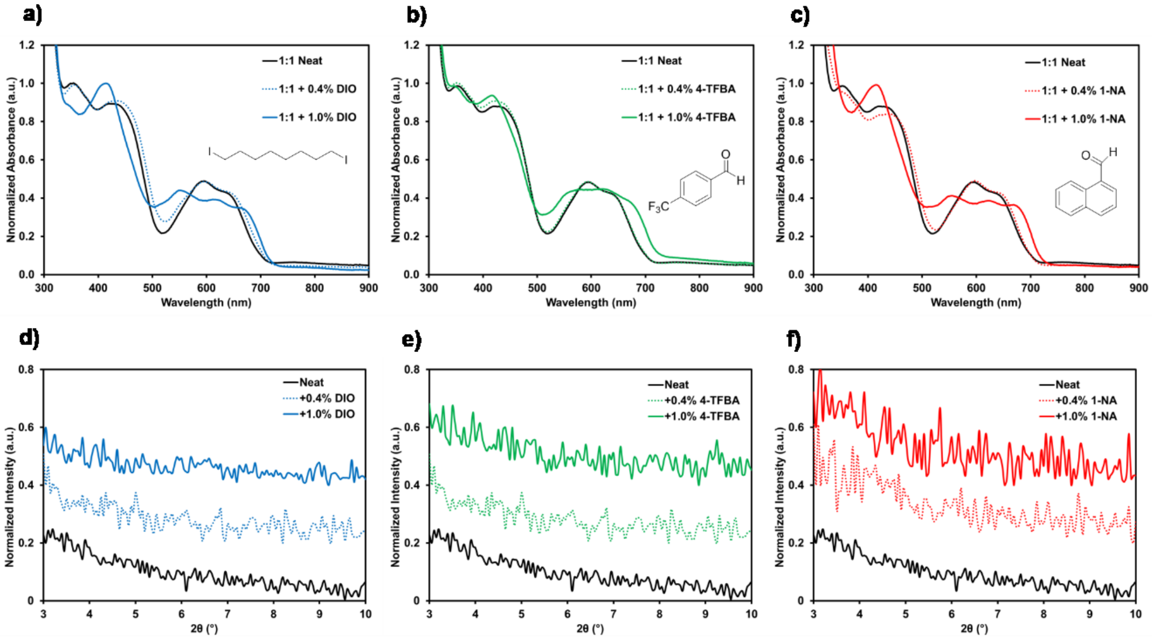

Figure J1. UV-Vis spectra of D1-A1 blend thin films (1:1 weight ratio) with various amounts of solvent additives: a) DIO, b) 4-TFBA and c) 1-NA. Also shown are XRD patterns of the blend films with d) DIO, e) 4-TFBA and f) 1-NA.

Solvent Vapour Annealing

Solvent vapour annealing (SVA) involves the exposure of a thin film to a gaseous solvent for a given amount of time (see **Figure J2**).

Figure J2. A photograph of a D1-A1 thin film undergoing SVA in an annealing chamber.

An SVA chamber was prepared by dispensing 2000 μL of $CHCl_3$ into a clean and dry shot glass with a lid covering the mouth. The solvent vapour was allowed to saturate the interior of the chamber for 10 minutes. To anneal a film, the film-coated substrate was suspended above the solvent before re-attaching the lid. The vapour was allowed to penetrate the film for a set amount of time before the substrate was removal. The film was allowed to dry for 2 minutes before a UV-Vis spectrum was acquired. The film was then returned to the chamber and annealed for additional time. This process of sequential annealing with intermittent acquisition of UV-Vis spectra was repeated until the total amount of time spent in the chamber was equal to 20 minutes. An XRD pattern of the film after SVA for a total time of 20 minutes was also acquired.

From the UV-Vis spectra in **Figure J3**, one can observe changes in the absorption profile after only a short duration of SVA (i.e., 60 s). The change in the band structure of A1 as a result of SVA is very similar to that observed after the use of DIO and 1-NA as solvent additives. No evidence of crystallinity in the films after SVA were detected using XRD. Again, AFM is an invaluable tool for probing the morphology of this system and will be applied in future experiments.

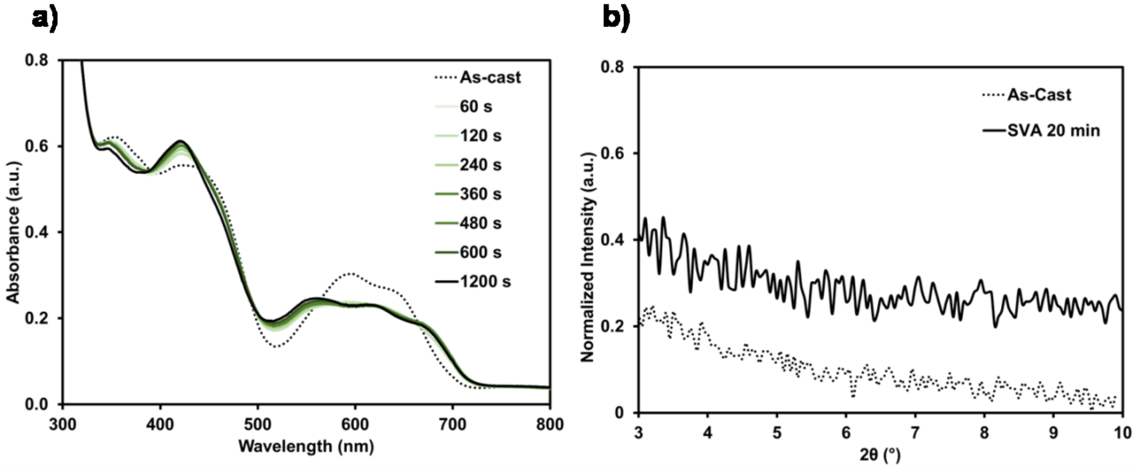

Figure J3. a) UV-Vis spectra of a D1-A1 blend thin film (1:1 weight ratio) before and after sequential SVA. b) XRD patterns of a D1-A1 blend thin film before and after SVA for 20 min.